Title

Techniques in Live Neutron Spectroscopy

Author

Brand, Christopher Alexander

Publication Date

2024

Peer reviewed|Thesis/dissertation

Techniques in Live Neutron Spectroscopy

By

Christopher Alexander Brand

A dissertation submitted in partial satisfaction of the

requirements for the degree of

Doctor of Philosophy

in

Engineering - Nuclear Engineering

in the

Graduate Division

of the

University of California, Berkeley

Committee in charge:

Professor Lee Bernstein, Chair
Professor Paul Renne
Professor Jasmina Vujic
Doctor Darren Bleuel

Spring 2024

Techniques in Live Neutron Spectroscopy

Abstract

Techniques in Live Neutron Spectroscopy

By

Christopher Alexander Brand

Doctor of Philosophy in Engineering - Nuclear Engineering

University of California, Berkeley

Professor Lee Bernstein, Chair

The neutron flux of three neutron beam experiments was measured using a novel neutron spectrometer system, referred to as a Scatter Time-of-Flight (STOF) spectrometer. The neutron beam was generated via the nuclear breakup of 14 and 23 MeV deuteron beams on a thick natural carbon target at the 88-Inch Cyclotron at Lawrence Berkeley National Laboratory (LBNL). The system is shown to be capable of measuring the energy-dependent neutron flux on a per-experiment basis. Furthermore, the resulting neutron flux was unfolded using experimentally determined activation foil reaction rates and a maximum entropy spectral unfolding algorithm. The spectrum unfolding was needed to determine the STOF efficiency as a function of neutron energy. The modular nature of the system allows for it to work in low and high-intensity fluxes, broad energy ranges, and various experimental configurations. The STOF spectrometer, in conjunction with activation foils and spectral unfolding techniques, provides a powerful, high-efficiency capability to noninvasively monitor neutron spectra at experimental facilities like GENESIS where a high beam repetition rate makes traditional time-of-flight techniques not possible due to knowledge of the appropriate start time.

To Friends

Thank you :)

Contents

List of Figures

List of Tables

Acknowledgments

I would like to gratefully acknowledge my dissertation committee for their expert advice and proofreading of this thesis. I am thankful to my academic advisor Professor Lee Bernstein and lab mentor Doctor Darren Bleuel for their support and guidance throughout my graduate studies. I am very thankful to the Bay Area Neutron Group, particularly Bethany Goldblum, Thibault Laplace, Joey Gordon, and Josh Brown for providing feedback on scientific inquiries and general advice. There are a multitude of individuals who have provided funding and tools over the years that allowed me to complete this work. Thank you to Sean Walston, Brian Rusnak, Roark Marsh, Michael Buchoff, Jo Ressler and the National Science and Security Consortium.

This work performed under the auspices of the U.S. Department of Energy by Lawrence Livermore National Laboratory under Contract DE-AC52-07NA27344 and at Lawrence Berkeley National Laboratory under Contract No. DE-AC02-05CH11231.

This material is based upon work supported by the Department of Energy National Nuclear Security Administration through the Nuclear Science and Security Consortium under Award Number DE-NA0003996.

Chapter 1

Introduction

1.1 Motivation

The 88-Inch Cyclotron at Lawrence Berkeley National Laboratory (LBNL) is used for performing a broad range of nuclear measurements and experiments [1]. Of relevance to this work are neutron cross section measurements that support applications such as nuclear data, national security, and nuclear energy. These experiments require a neutron spectrometer to measure the fast neutron spectrum.

The development of an adaptable Time-of-Flight (TOF) spectrometer and methodology was required to facilitate cross section measurements at the Gamma-Energy Neutron-Energy Spectrometer for Inelastic Scattering (GENESIS) facility [2] at Lawrence Berkeley National Laboratory (LBNL). The TOF method, which measures the transit time of particles traveling a known distance, was adapted into a variation called Scatter Time-of-Flight (STOF) for this purpose.

The STOF spectrometer is designed to be used in a variety of experimental settings, including high or low flux environments, with high resolution and efficiency. Importantly, it operates independently of the beam pulse parameters of the accelerator. This flexibility allows the system to be used for ongoing and future projects not just at LBNL, but at other neutron production facilities produced by pulsed charged-particle beams with a short time spacing that causes ambiguity in the determination of the neutron energy via time-of-flight, such as the Neutron Imaging Facility at Lawrence Livermore National Laboratory (LLNL).

A foil activation based spectrum-unfolding methodology was developed to help characterize the STOF system and allow for extrapolation of the spectrum down to energies, below which the spectrometer is capable of measuring.

The STOF spectrometer and unfolding method provides valuable support for detailed and accurate nuclear data measurements of a wide variety of experimental settings and energy ranges.

1.2 Background

1.2.1 GENESIS Array

GENESIS is a detector array constructed to measure the neutron non-elastic cross sections for a variety of materials. The array measures both scattered neutrons (using organic liquid scintillators) and gamma rays (using high-purity germanium Clover detectors) from neutron inelastic scattering for a material of interest, referred to as the GENESIS target. The general form of the equation for determining the microscopic cross section is shown below, where $\sigma(E)$ is the energy-dependent microscopic cross section, $I_R(E)$ is the measured rate of particle interactions with the material, $F(E)$ is the energy-dependent incident flux of a parallel neutron beam, N is the number density of the material, and V is the volume of the material,

$$\sigma(E) = \frac{I_R(E)}{F(E) * N * V}. \tag{1.1}$$

As shown in Eq. (1.1), the energy-dependent neutron flux is required to determine the cross section. The STOF spectrometer and unfolding method were developed to perform this measurement.

1.2.2 88-Inch Cyclotron Constraints

The GENESIS array is located at the 88-Inch Cyclotron at LBNL. Here a neutron beam is produced by focusing a deuteron beam on a target material (e.g. Ta, Be, or C). For light nuclei, this results in a broad neutron spectrum that peaks near half the beam energy minus the deuteron-breakup Q value [3, 4].

The broad neutron spectrum, limited flight path, and beam pulse frequency creates an ambiguity in the determination of neutron energy via time-of-flight measurements due to an effect known as frame overlap. Each cyclotron pulse produces a burst of neutrons with a broad energy range. Fast neutrons from a subsequent burst can catch up with the slow neutrons from the previous burst. This frame overlap creates a unique measurement challenge for any potential neutron spectrometer.

There is an additional uncertainty in the beam energy, this is shown in Fig. 1.1. Consequently, the time resolution of TOF spectrometers that use the accelerator's internal RF signal is significantly degraded.

Cyclotron facilities have achieved significant beam structure improvements by implementing phase slits [5]. These are collimators that block the edges of the particle beam during acceleration, thereby reducing the number of overlapping particles from additional injected beams. The 88-Inch Cyclotron has historically operated with phase slits, though this capability is not present at the time of writing. A downside to the implementation of phase slits is that it also reduces the beam intensity, which is not desirable for the GENESIS facility.

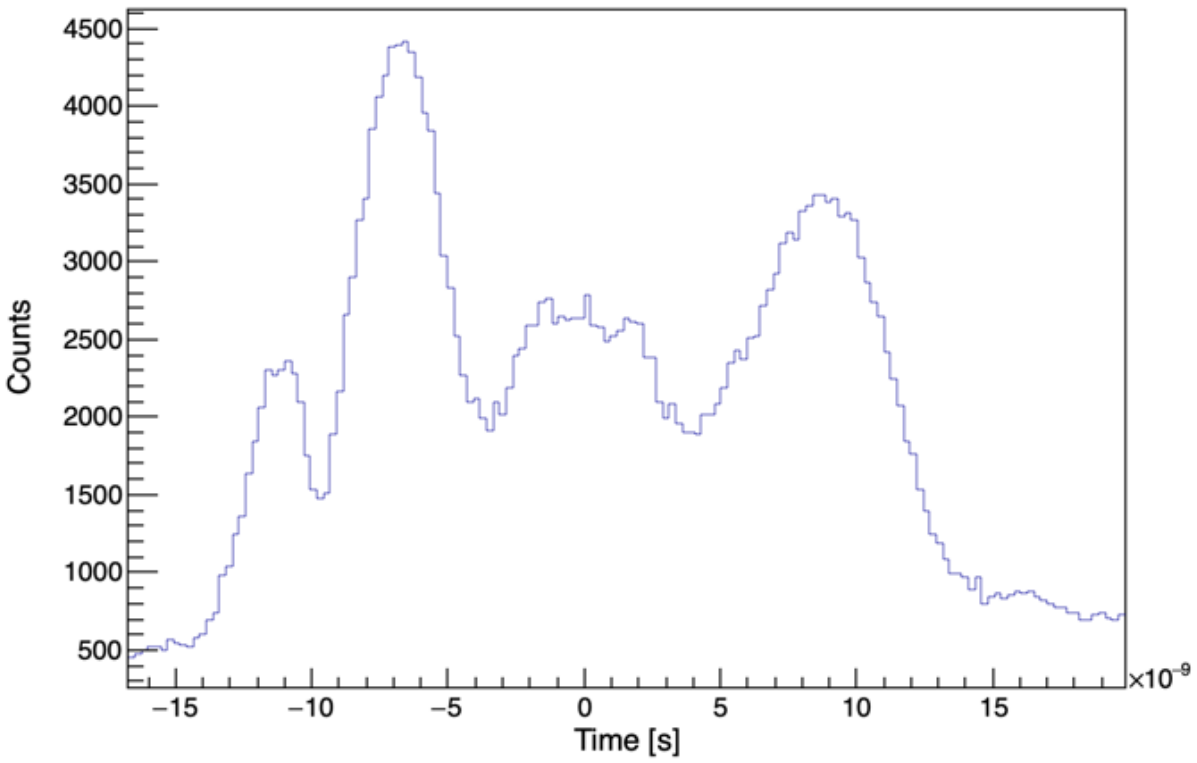

Figure 1.1: Example TOF spectrum between the cyclotron's RF signal and γ rays detected from an in-beam organic scintillator detector, illustrating the irregular nature of the beam pulse structure.

1.2.3 Neutron Beam Characterization Systems

The complexities associated with fast neutron detection have historically been addressed in a number of ways. Each developed system is designed within the constraints of the associated neutron production facility and the limits of technology at the time of implementation. Three primary apparatuses that have been developed are: Scintillator TOF [6, 7], fission chamber TOF [8–15], and proton recoil telescopes [16–19]. A novel adaptation of organic scintillator TOF detection, the Scatter Time-of-Flight spectrometer (STOF), was developed to characterize fast neutron fluxes at the 88-Inch Cyclotron. In addition, a maximum-entropy unfolding technique [20] was applied to neutron activation foil measurements to complement the STOF-determined neutron flux measurements. The following three sections provide a brief overview of all three approaches.

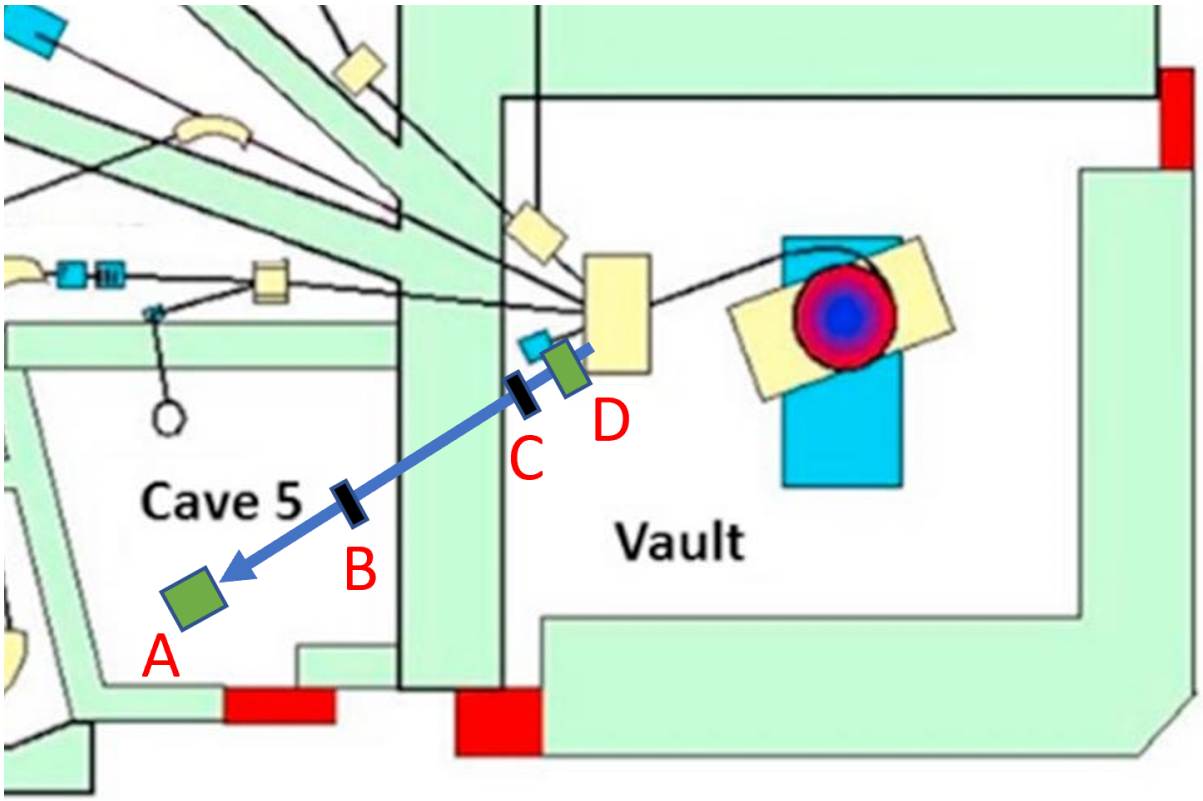

Figure 1.2: Layout of the 88-Inch Cyclotron Facility at LBNL. Cave 5 is the location of all measurements. The green box in the Vault (D) is the location of the deuteron target. The black box in the Vault (C) is the collimator. The blue arrow extending from the Vault into Cave 5 is the neutron beam path, and the green box in Cave 5 (A) is the approximate location of STOF. The black box (B) in cave 5 is the location of the GENESIS target.

1.2.3.1 Scintillator TOF

Scintillators are commonly used as a detection medium for neutrons. These scintillators consist of a hydrocarbon material that emits visual light (scintillation) when electrons excite and de-excite within the molecular energy levels. They can be in solid form (such as plastics and stilbenes) or liquid form (such as EJ-309). The visible light emitted from the scintillation is then collected by a Photo-Multiplier Tube (PMT), which converts it into a current signal proportional to the amount of light collected.

Neutrons are indirectly detected by measuring the light yield from recoiling protons produced when the neutrons scatter off of hydrogen or, to a much lesser degree, off of heavy nuclei in the scintillator. This process allows for the detection of neutrons with a relatively high level of efficiency. Additionally, these neutron detectors are capable of particle identification via Pulse Shape Discrimination (PSD), an analysis technique that distinguishes

between different types of ionizing radiation based on the time dependence of their light yield as a function of time.

These neutron detectors are used to determine the energy-dependent neutron flux spectra via a TOF analysis. By experimentally measuring the location and time of the same neutron at two different locations, the relativistic Eq. (1.2) is applied to calculate the energy of the neutron, where E_n is the neutron energy, d is the distance between the two known positions, T is the transit time between each location, m_n is the neutron mass, and c is the speed of light.

$$E_n = \left(\frac{1}{\sqrt{1 - (\frac{d/T}{c})^2}} - 1 \right) m_n c^2. \tag{1.2}$$

TOF is one of the most reliable and widely used neutron spectroscopy methods for achieving high energy resolution of fast neutron spectra.

Two possible configurations of this methodology are primary time-of-flight and scattered time-of-flight. Primary time-of-flight consists of a neutron detector placed inside the neutron beam and acts as the end event timestamp and location. The start event is the timestamp when the charged particle beam hits a target, creating the neutron pulse. Measurements of this configuration quickly run into issues due to the dependence on the beam pulse parameters. The energy resolution is limited by the width of the beam pulse, the accuracy is restricted due to frame overlap, and the non-Gaussian beam pulse results in a non-Gaussian timing convolution.

The second proposed configuration, scattered time-of-flight, is based on a previous double time-of-flight method [6, 7]. A hydrogen-rich neutron detector (the target cell) is placed in the beam path to measure elastically-scattered neutrons. Multiple neutron detectors are then placed outside the beam (scatter cells) to detect scattered neutrons from the target cell. The TOF-calculated scattered neutron energy is then kinetically converted to the energy of the original in-beam neutron. This configuration, while less efficient than primary TOF, is not reliant on the beam pulse structure and so bypasses the frame overlap and non-Gaussian pulse structure issues.

The scatter time-of-flight configuration is easily scalable by altering the volume of the scintillators or adding additional scatter cells. The system consists of scintillators, PMTs, and a limited amount of structural material to minimize the spectrometer's footprint of potential background scattering sources.

1.2.3.2 Fission Chamber TOF

Fission chambers are a type of gaseous ionization detector used for neutron detection. The apparatus comprises a pair of electrically-conducting plates arranged opposite each other with a layer of fissile material (commonly, uranium or plutonium) deposited on them. The gap between the plates is filled with inert gas, such as nitrogen or argon, and an electric field is established across the plates by applying a bias. Incident neutrons cause fission in the

fissile layer, producing fission fragments that are expelled into the gas, inducing ionization. The electric field separates the resulting electrons and ions towards the plates, which collect the charge.

The fission fragment events are easily discriminated from other charged particles, including most importantly alpha particles from the decay of the fissile material, due to the large amount of energy they deposit. This allows for discrete separation from most background events. Fission chambers have been utilized at other neutron facilities as neutron monitors and neutron TOF spectrometers [8–15]. Fission chambers inherently have low efficiency. Since the high stopping power of the fission fragments limits the thickness of the fissile foil that can be used. In practice, the fragments have approximately a stopping distance of 10 microns within the fissile material [21]. Therefore, any detection system requires the use of fissile layers less than about 10 microns, otherwise, the fission fragments will not make it to the ionizing gas. Scaling up systems that use fission chambers would therefore need to be done by using multiple detectors or increasing the surface area of the fissionable layer.

In a scatter TOF configuration, the fission chamber could only be used as a scatter cell, with an alternative detector being implemented as the target cell. The geometric inefficiency combined with the intrinsically-inefficient fission chamber needs to be compensated by using numerous fission chambers, and consequently, fissionable material, to reliably achieve neutron spectrum measurements. To achieve high efficiency, the amount of fissionable material is substantial. While not a standard fission chamber, one example of a high-efficiency neutron detector used 12 kgs of highly enriched uranium [22]. Such a quantity of fissionable material is not feasible from an economic, security, and hazard standpoint. In addition, the size of such systems and radiation created from the fissionable material are likely to lead to significant backgrounds for the GENESIS array measurements.

Therefore, the use of fission chambers would necessitate a primary TOF configuration. In this configuration, the efficiency can be increased by the development of a large-area detector. At the 88-Inch Cyclotron, the maximal possible efficiency increase is limited by the diameter of the collimated neutron beam. This configuration has the additional problem of having a large incident background due to frame overlap. The combination of the limitations due to low intrinsic efficiency and failure to address the frame overlap concerns necessitates the exclusion of fission chambers as the preferred detector for use as a neutron spectrometer at GENESIS or a similar facility.

1.2.3.3 Proton Recoil Spectrometer

Another common spectrometer design is the Proton Recoil Telescope (PRT) [16–19]. These detectors feature a thin hydrogen-rich foil that produces a proton beam through neutron-proton elastic scattering and two Si particle detectors. The front-facing detectors are thin enough for a partial proton energy deposition (punch-through), followed by a thick back detector to fully stop the proton and collect its remaining energy. This method allows for particle discrimination based on the unique ΔE (front) vs E (front and back) relation,

resulting in a significant reduction of background from neutron scatter on other elements in the converter foil. However, similar to the fission chamber, the lower energy threshold of the observable neutron is relatively high, as the proton must have sufficient energy to penetrate not just the conversion target but also the ΔE silicon detector.

More sophisticated PRT designs use segmented detectors [23] to perform real-time ray tracing of the charged particle, or configurations that combine both PRT and neutron time-of-flight methods [24]. Such spectrometers provide improved energy resolution and low-energy measurements. However, these systems are complex, are of higher cost, limited efficiency, and require a large volume of material (resulting in large potential background for any GENESIS measurements).

These concerns make the PRT a non-ideal system for use as a neutron spectrometer compared to the proposed STOF spectrometer.

1.2.4 Neutron Spectrum Unfolding via Activation

Neutron spectrum unfolding techniques are mathematical algorithms that are used to determine or improve measured neutron spectra [20] via the observation of radioactive reaction products in one or more activation foils irradiated in the neutron beam. Two prominent techniques are: detector response unfolding and activation foil unfolding. These methods require some level of prior information regarding the measured spectrum, as they attempt to solve an under-determined problem. When combined with the results of TOF measurements, they can further refine the neutron spectrum. In this work, neutron activation foil spectrum unfolding is used to adjust the neutron spectrum measured by STOF with measured reaction rates based on well-known reaction cross sections and measured reaction rates. Using measured reaction rates, an unfolding methodology is able to improve the spectrum by both correcting for deficiencies in the STOF spectrum due to limits inherent in the efficiency simulation and extrapolating the spectrum to energies below the lower energy threshold of the STOF spectrometer.

1.3 Datasets

Three separate datasets were acquired and analyzed. A summary of the datasets are tabulated in Table 1.1. Two datasets, referred to as dataset 14(^{56}Fe) and dataset 14(NaCl), were obtained during experiments with a 14 MeV deuteron beam incident on a natural carbon target. The GENESIS target for the 14(^{56}Fe) experiment was an enriched ^{56}Fe rolled disk. The GENESIS target for the 14(NaCl) experiment was a natural NaCl packed powder. The third dataset, referred to as dataset 23(Al_2O_3), was measured during an experiment with a 23 MeV deuteron beam incident on the same natural carbon target. The 23(Al_2O_3) experiment used sapphire as the GENESIS target. The same STOF configuration was used for all three measurements.

Dataset	Deuteron Energy [MeV]	GENESIS Target	Deuteron Target
14(^{56}Fe)	14	^{56}Fe (Enriched)	Carbon (Natural)
14(NaCl)	14	NaCl (Natural)	Carbon (Natural)
23(Al_2O_3)	23	Al_2O_3 (Natural)	Carbon (Natural)

Table 1.1: Summary of analyzed experimental datasets.

Chapter 2

Theory

This section provides a detailed overview of the mathematics and physics of neutron detection via organic scintillators, neutron activation, and the maximum entropy unfolding model.

2.1 Organic Scintillators

Organic scintillators are a radiation detection medium fabricated from hydrocarbons that emit visible light through the excitation and de-excitation of molecular-electron energy levels (scintillation).

2.1.1 Energy Deposition

2.1.1.1 Neutron Energy Deposition

The scintillator detectors used for this work detect neutron events through indirect measurements of elastically scattering neutrons. A neutron incident on a target, as shown in Fig. 2.1, will elastically scatter, depositing an amount of energy that is dependent on the scattering angle. This interaction ionizes the target particle, causing it to recoil through the medium, producing measurable photons through scintillation. Using conservation of energy and momentum the relationship between the scattering angle and particle energy can be derived from the frame of reference of the target particle, where $E_{incoming,n}$ is the energy of the incoming neutron, $E_{outgoing,n}$ is the energy of the scattered neutron, m_t is the mass of the scattering target, m_n is the neutron mass, and θ is the scattering angle of the neutron,

$$\left(\frac{E_{outgoing,n}}{E_{incoming,n}}\right)^{\frac{1}{2}} = \frac{m_n cos(\theta) \pm (m_n^2 cos^2(\theta) + (m_t + m_n)(m_t - m_n))^{\frac{1}{2}}}{m_n + m_t}. \tag{2.1}$$

The amount of energy transferred is dependent on the mass of the target particle. Notably, the energy transferred between a neutron and a target particle of hydrogen (A

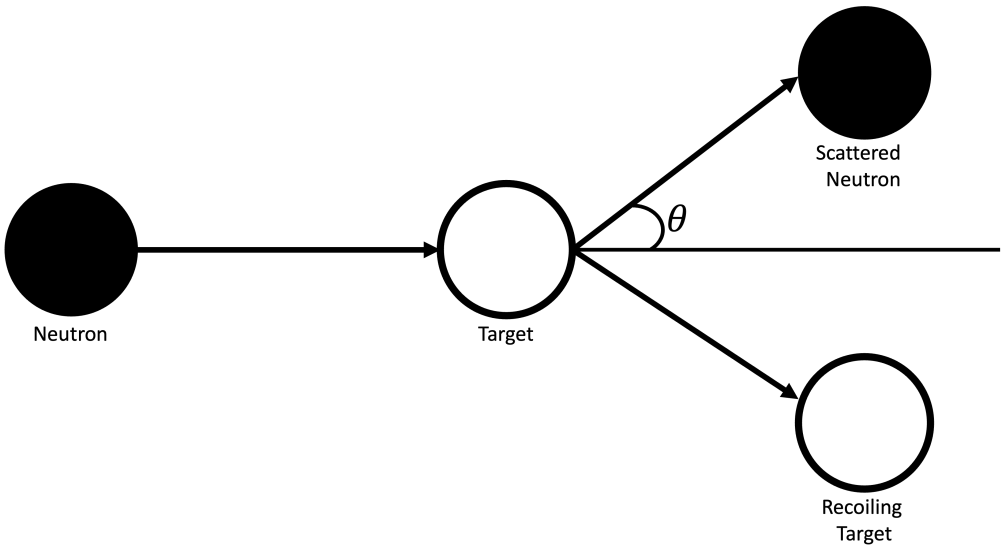

Figure 2.1: Diagram of neutron elastic scattering in the lab frame of reference, where θ is the neutron scatter angle.

= 1) vs carbon (A = 12), is less in carbon elastic scattering. The relationship between the scattering angle and neutron particle energy from hydrogen scattering is important for this work. Taking Eq. (2.1) where $m_n = m_t = 1$ and solving for $E_{incoming,n}$ results in the following relation,

$$E_{incoming,n} = \frac{E_{outgoing,n}}{cos^2(\theta)}. \tag{2.2}$$

Following the same methodology, the energy of the recoiling proton, $E_{Recoiling,p}$ in terms of the scattered neutron is,

$$E_{Recoiling,p} = E_{outgoing,n} sin^2(\theta) \tag{2.3}$$

2.1.1.2 γ-ray Energy Deposition

The primary mechanism through which γ rays deposit energy within a scintillator is Compton scattering. The γ-ray energy is transferred into an electron, ionizing it, which in turn induces scintillation.

2.1.2 Light Yield from Scintillation

The scintillators used in this work consist of hydrocarbon molecules that create a π-electron energy structure. The molecular energy structure is composed of a series of singlet states (spin = 0) alongside a series of triplet states (spin = 1). Incident charged-particles

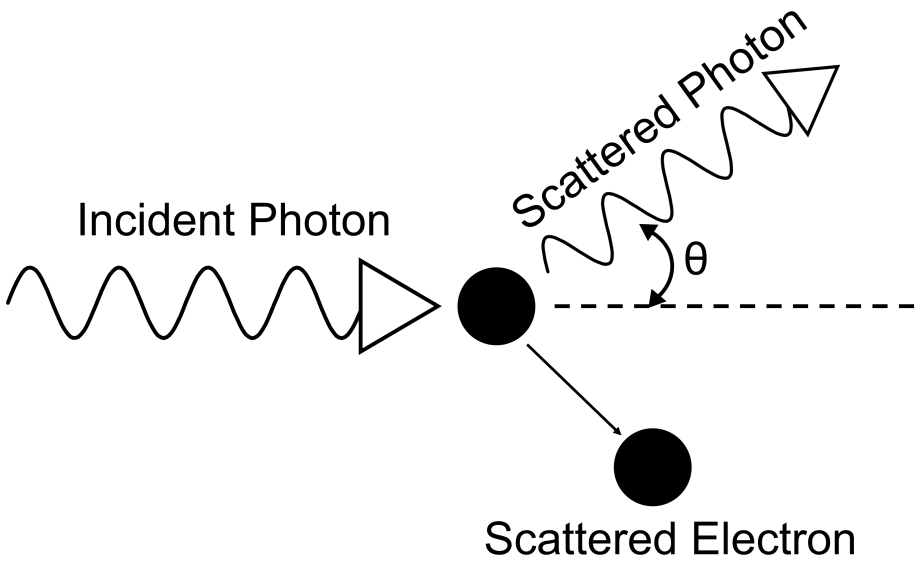

Figure 2.2: Diagram of photon Compton scattering in the lab frame of reference, where θ is the photon scattering angle.

deposit their kinetic energy in the molecular electron bands, exciting the bound electrons from a ground state into higher energy singlet states. From here, there are two predominant scintillation mechanisms, known as prompt fluorescence and delayed fluorescence.

Prompt fluorescence occurs when the excited electron migrates to the lowest energy state within the singlet bands and then decays back to one of the vibrational ground states through the emission of a visible photon, shown in Fig. 2.3. The initial migration occurs via the radiation-less decay of phonons or emission of heat. This relaxation of the electron, followed by its decay, means that the emitted photon is energetically lower than the molecular excited state and is therefore transparent within the scintillating medium. This transparency allows for the collection of this produced light with a light collection instrument such as a photomultiplier tube.

Delayed fluorescence occurs when the excited electron performs an intersystem crossing from the singlet state to the triplet state and then crosses back to the singlet state before continuing the de-excitation process by the decay of a visible photon, exhibited in Fig. 2.4. The transition from the triplet state back to the singlet state is possible due to a bi-molecular interaction between two different molecules that are in excited triplet states. When two triplet-excited molecules interact with each other, it is possible for triplet-triplet annihilation to occur, leaving one molecule in the excited singlet state and another in the de-excited ground state. This process takes a longer period of time than prompt fluorescence, and so light yield contributions to the detector pulse occur later in time than contributions due

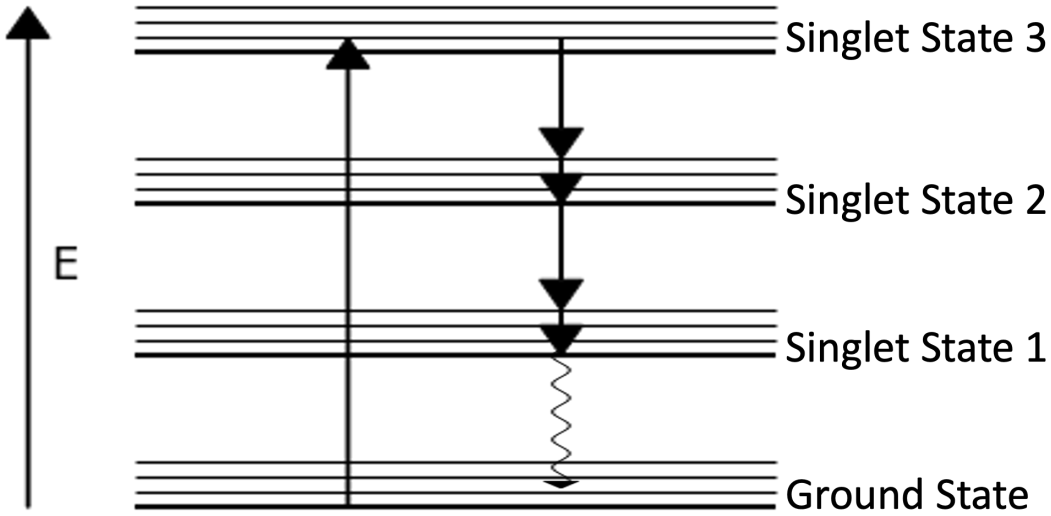

Figure 2.3: Molecular energy diagram of prompt fluorescence.

to prompt fluorescence. The requirement for the excited molecules to be locally adjacent to each other means that particles with higher ionization densities also have an increased likelihood to produce delayed fluorescence. The amount of delayed vs prompt fluorescence for a detection event is, therefore, dependent on the type of charged particle, with electrons produced from γ-ray scattering primarily producing prompt fluorescence and protons from neutron scattering producing a relativity larger amount of delay fluorescence.

2.1.3 Quenching Processes and Light Yield Model

There are various interactions that cause the loss of photons in a scintillating medium. These mechanisms, collectively referred to as quenching, result in a loss of detectable deposited energy for individual events. First, triplet-triplet annihilation, which is described in detail in Section 2.1.2, is responsible for delayed fluorescence. This interaction results in reduced light yield production due to the loss of one of the excited triplet states to radiationless decay. Second, singlet ionization quenching is analogous to triplet-triplet annihilation, but instead of two triplet states, two singlet states of different molecules interact with each other, resulting in the loss of one state to a ground state and another to a higher-level singlet state. Third, it is also possible for molecules in excited energy states to relax or decay to a lower state through the emission of phonons rather than photons, known as

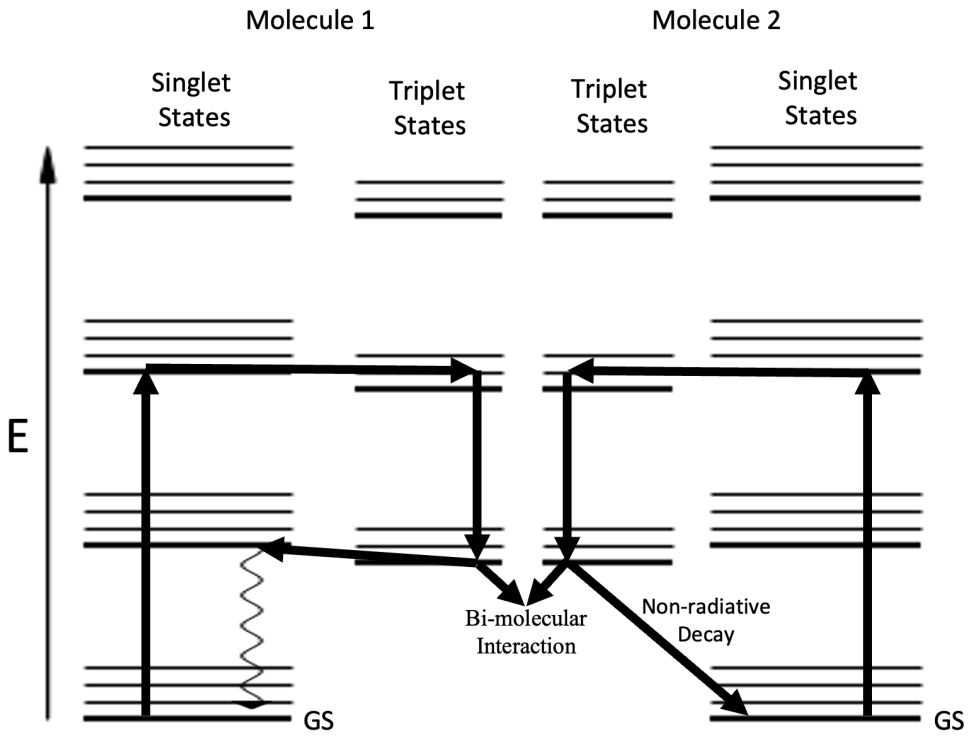

Figure 2.4: Molecular energy diagram of delayed fluorescence. Two adjacent molecules are excited and perform an intersystem crossing into the triplet states. The two triplet states interact and annihilate, promoting one molecule back into the singlet state and the other into the ground state (GS) through non-radiative decay.

radiationless de-excitation. Finally, light yield can be reduced due to contaminants absorbing the energy and not emitting observable photons. Known as contamination quenching, this is commonly due to oxygen contamination within the scintillating material.

As a consequence of the various quenching processes, light yield as a function of energy deposition can be non-linear. Multiple efforts have been conducted to produce semi-empirical models of the light yield, [25–28]. The Yoshida model [28] is used in this work. This model builds upon the work done by Chou [26] and Hong [27]. Chou proposed an empirical extension of the Birks formula [25] resulting in the following,

$$\frac{dL}{dx} = \frac{S(\frac{dE}{dx})}{1 + kB(\frac{dE}{dx}) + C(\frac{dE}{dx})^2}, \tag{2.4}$$

where C is a fitted constant for higher-order correction, $\frac{dL}{dx}$ is the differential light output, S

is the scintillation efficiency, kB is "Birks constant," and $\frac{dE}{dx}$ is the energy loss of a specified charged particle. Hong notes that the energy loss is more accurately represented in two terms: nuclear energy loss and electronic energy loss. Both of these contribute to the quenching processes distinctively and so should be represented as separate terms. The Yoshida paper combines these two extensions of the Birks Model into a new generalized formula,

$$\frac{dL}{dx} = \frac{S_e(\frac{dE}{dx}) + S_n(\frac{dE}{dx})_n}{1 + kB_e(\frac{dE}{dx})_e + C_e(\frac{dE}{dx})_e^2 + kB_n(\frac{dE}{dx})_n}, \tag{2.5}$$

where e are the electronic energy loss terms and n are the nuclear energy loss terms.

2.2 Activation

2.2.1 Reaction Rates

Measuring the production of radionuclides in a target irradiated in a neutron beam provides additional experimental information used to further refine the characterization of the energy differential neutron flux. The reaction rates are derived from γ ray counting measurements of various foils that have been activated by the measured neutron beam. By carefully selecting material types, γ-rays of specific energies can be directly correlated with a specific reaction rate. The radioactivity of a sample is given by

$$A = \lambda N, \tag{2.6}$$

where A is the activity of the foil, λ is the decay constant, related to the half life, $t_{1/2}$ by the relation $\frac{ln(2)}{t_{1/2}}$, and N is the number of nuclei. Additionally, the decay law for the activity as a function of time, t, is,

$$A(t) = A(0)e^{-\lambda t}. \tag{2.7}$$

Given an idealized situation where all the reaction products are made at a single instant at t=0 and the reaction product's half-life is much smaller than the counting time, t_{count}, the total activity is related to the total number of measured γ-ray events through the following,

$$A = \frac{C}{t_{count}\epsilon_n B}, \tag{2.8}$$

where C is the measured γ-ray counts, ϵ_n is the detection efficiency, and B is the branching ratio for the decay path. An additional decay term quantifies the loss of activity during the counting time to produce the following,

$$A = \frac{C\lambda}{f_{lt}\epsilon_n B(1 - e^{-\lambda t_{count}})}. \tag{2.9}$$

A is the activity of the sample at the beginning of the γ-ray measurement and f_{lt} is the livetime fraction (defined as the fraction of time that the data acquisition system is available to record the decay of the radioactive product). To determine the activity at the end of irradiation, another decay term accounts for the time between the start of the count and the end of irradiation, $t_{transfer}$, using the decay law as follows,

$$A = A_{irr}e^{-\lambda t_{transfer}}, \tag{2.10}$$

where A_{irr} is the activity at the end of the irradiation. Solving for A_{irr} and substituting into Eq. (2.9), the relation becomes,

$$A_{irr} = \frac{C\lambda}{f_{lt}\epsilon B(1 - e^{-\lambda t_{count}})e^{-\lambda t_{transfer}}}. \tag{2.11}$$

The reaction rate, I, is then calculated using the evaluated A_{irr}. Assuming a constant incident flux for the irradiation period, the rate of the produced radioactive nuclei, dN, is represented as the number gained from the reaction rate, Idt, and the amount lost from the subsequent radioactive decay, λNdt, shown below,

$$dN = Idt - \lambda Ndt. \tag{2.12}$$

Integrating Eq. (2.12) by substitution, the equation reduces to

$$\lambda N(t) = I(1 - e^{-\lambda t}). \tag{2.13}$$

The activity at the end of the irradiation period, t_{irr}, is thus,

$$A_{irr} = \lambda N(t_{irr}) = I(1 - e^{-\lambda t_{irr}}). \tag{2.14}$$

Finally, solving for I gives,

$$I = \frac{A_{irr}}{1 - e^{\lambda t_{irr}}} = \frac{C\lambda}{f_{lt}\epsilon B(1 - e^{-\lambda t_{count}})e^{-\lambda t_{transfer}}(1 - e^{\lambda t_{irr}})}. \tag{2.15}$$

2.2.2 Evaluated Flux

The reaction rate, I, is defined as,

$$I = N * \int \sigma(E)\phi(E), \tag{2.16}$$

where N is the number of target atoms, E is the energy, σ is the cross section, and ϕ_i is the flux within the foil. When the thin foil approximation is not valid, ϕ_i is not equal to the flux incident on the foil. The incident flux on the foil, f, is added to this equation to produce,

$$I = N * \frac{\int \sigma(E)\phi(E)}{\int f(E)} \int f(E). \tag{2.17}$$

Solving for the integrated incident flux, $f(E)$, results in,

$$\int f(E) = \frac{I \int f(E)}{N \int \sigma(E)\phi(E)}. \tag{2.18}$$

2.3 Neutron Spectrum Unfolding

Activation foil spectral unfolding algorithms are used to determine or improve measured neutron spectra from the observation of radioactive reaction products of multiple activation foils irradiated in the neutron beam. Spectral unfolding is a numerical attempt to solve the following set of n discrete problems,

$$M_n + \epsilon_n = \sum_i R_{n,i} * \sum_i \Phi_i, \tag{2.19}$$

where n is each measurement from $n = 1$ up to a maximum of $n = n_{max}$. M_n is the measured value for each observation, ϵ_n is an uncertainty variable for each measurement, $R_{n,i}$ is the differential response function (e.g., the activity produced in at a given incident neutron energy) of the system for each measurement, i is each discretized energy bin from $i = 1$ up to $i = i_{max}$, and Φ_i is the flux spectrum.

The measurements, M_n, used for this unfolding is the set of measured reaction rates, I_n, from Eq. (2.15) for each measured reaction. The response function, R, is therefore the response due to the beam irradiation of multiple foil materials. The reaction rate is related to the differential flux spectrum through the following,

$$I_n = N_n \sum_i \sigma_{i,n}\phi_{i,n}, \tag{2.20}$$

where $\sigma_{i,n}$ is the grouped cross section for each reaction and each energy bin, $\phi_{i,n}$ is the total energy-dependent flux within the foil associated with the reaction, and N_n is the total number of atoms. The flux within a foil, $\phi_{i,n}$, is different from the flux incident on the foil, f_i, due to scattering within the foil as well as scattering from the environment into the foil. The desired spectrum to unfold is f_i and so Eq. (2.20) is expanded by adding the discrete incident flux, $\sum_i f_i$, as follows,

$$I_n = N_n \sum_i \sigma_{i,n}\phi_{i,n} * \frac{\sum_i f_i}{\sum_i f_i} = \sum_i \omega_{i,n} \sum_i f_i. \tag{2.21}$$

Therefore, the generalized Eq. (2.19) becomes a set of discrete equations,

$$I_n + \epsilon_n = \sum_i \omega_{n,i} * \sum_i f_i, \qquad n = 1, ..., n_{max}. \tag{2.22}$$

I_n is equal to the measured reaction rate, $\omega_{n,i}$ is the energy-dependent response for each reaction, and f_i is the energy-dependent flux. The uncertainty term, ϵ_n, is a free variable

that allows the unfolding algorithm to adjust the reaction rates when determining the best fit. The uncertainty term of the reaction rates are Poisson distributed and so is constrained, due to chi-squared statistics, by the variance of each measurement, V_n, and the degrees of freedom, N_{DOF}. N_{DOF} is equal to the number of measured reaction rates, resulting in the following constraint for the uncertainty term,

$$N_{DOF} = \sum_n \frac{\epsilon_n^2}{V_n} = \text{number of reactions measured.} \tag{2.23}$$

This problem cannot be solved directly, as it is under-determined, since the number of reaction rate data points will be less than the number of bins in the measured neutron flux.

2.3.1 Information Theory: Information Entropy

Solving the unfolding problem requires a numerical solution. Such a solution is possible with principles derived from within information theory. Information theory mathematically quantifies the concept of information by relating it to probability. Information can be thought of as the amount of "surprise" there is in a particular observation. One can postulate that events, or in the case of this work, reactions, have a particular probability of occurring. For example, given only two events are observed where event A has a high probability of occurrence and event B has a low probability of occurrence, it stands to reason that event B is of greater interest since it was less expected, therefore, event B contains more information than event A. From this premise, information theory develops a number of mathematical principles. One of these that is particularly relevant to this work, is the principle of information entropy.

Information entropy represents the average amount of information contained within a distribution and was first introduced in 1948 by Claude Shannon [29]. It is analogous to the concept of entropy in statistical thermodynamics and has the same general formulation, see Eq. (2.24), where S is entropy and p_i is the probability within an interval, i,

$$S = -\sum_i p_i ln(p_i). \tag{2.24}$$

Information entropy is a value that is less than or equal to 0, where 0 means there is no information, aka there are no "surprises" or everything is known.

The equation for relative information entropy between two different probability distributions, S_{rel}, also known as the Kullback-Leibler divergence, is derived from Eq. (2.24) to be the following,

$$S_{rel} = -\sum_i [p_i ln(\frac{p_i}{p_{0i}}) - p_i + p_{0i}], \tag{2.25}$$

where p_{0i} is an initial probability distribution of interest. This equation allows for a discrete comparison of the average information between two probability distributions. If

the distributions are the same, then there are no "surprises" and so the relative entropy is equal to 0.

2.3.2 Maximum Entropy

Given prior data about a probability distribution function, consider the set of all trial probability distributions that would encode the prior data. According to information theory, the distribution with maximal information entropy (closest to 0) is the best choice, since the distribution with the maximum entropy is the one that makes the fewest assumptions about the true distribution of data. Therefore, a new distribution can be calculated by maximizing the entropy value between two measured distributions with high confidence.

2.3.2.1 Unfolding with Maximizing Entropy

The probability distribution described in Eq. (2.25) is directly proportional to the neutron flux, as expressed below,

$$p_i \propto f_i, \tag{2.26}$$

where f_i is the neutron flux as a function of energy for an energy interval, i. Consequently, the relative information entropy between the unfolded flux, f_i, and an initial flux estimate, f_{0i}, is,

$$S_{rel} = -\sum_i [f_i ln(\frac{f_i}{f_{0i}}) - f_i + f_{0i}]. \tag{2.27}$$

The initial flux estimate, f_{0i}, is experimentally measured from the STOF spectrometer. The desired fluence, f_i, is the adjusted fluence given the reaction rates from activation foil analysis. A numerical solution is found using Eqs. (2.22), (2.23) and (2.27).

First the Lagrangian, L, associated with the maximization of Eq. (2.27) is,

$$L = S - \sum_n \lambda_n (\sum_i \omega_{n,i} f_i - I_n - \epsilon_n) - \mu (\sum_n \frac{\epsilon_n^2}{V_n} - N_{DOF}), \tag{2.28}$$

where λ_n and μ are Lagrange multipliers, n is each measured nuclear reaction product, and i is each flux energy bin. Next, substitute into Eq. (2.27) and take the variation with respect to f_i, λ_n ϵ_n, and μ. Variation with respect to f_i leads to,

$$0 = \frac{d}{d(f_i)} L$$

$$= \frac{d}{df_i} (\sum_i [f_i ln(\frac{f_i}{f_{0i}}) - f_i + f_{0i}] - \sum_n \lambda_n (\sum_i \omega_{n,i} f_i - I_n - \epsilon_n) - \mu (\sum_n \frac{\epsilon_n^2}{V_n} - N_{DOF}). \tag{2.29}$$

This reduces to,

$$\frac{d}{d(f_i)}L = -ln(\frac{f_i}{f_{0i}}) + 1 - 1 - \sum_n \lambda_n \omega_{n,i}$$

$$= -ln(\frac{f_i}{f_{0i}}) - \sum_n \lambda_n \omega_{n,i} = 0, \qquad i = 1, ..., i_{max}. \tag{2.30}$$

Equation (2.30) represent a set of i_{max} equations. Similarly, variation with respect to λ_n leads to a set of n_{max} equations,

$$0 = \frac{d}{d(\lambda_n)}L = \sum_i \omega_{n,i} f_i - I_n - \epsilon_n, \qquad n = 1, ..., n_{max}. \tag{2.31}$$

Next, variation with respect to ϵ_n results in,

$$0 = \frac{d}{d(\epsilon_n)}L = \lambda_n - 2\mu \frac{\epsilon_n}{V_n}, \qquad n = 1, ..., n_{max}. \tag{2.32}$$

Finally, variation with respect to μ is

$$0 = \frac{d}{d(\mu)}L = \sum_n \frac{\epsilon_n^2}{V_n} - N_{DOF}. \tag{2.33}$$

Solving Eq. (2.30) and Eq. (2.32) for f_i and ϵ_n respectively gives

$$f_i = f_{0i} e^{-\Sigma_n \lambda_n \omega_{n,i}}, \qquad i = 1, ..., i_{max}, \tag{2.34}$$

and,

$$\epsilon_n = \frac{\lambda_n V_n}{2\mu}, \qquad n = 1, ..., n_{max}. \tag{2.35}$$

Then Eq. (2.35) is plugged into Eq. (2.33) and μ is solved for to get

$$\mu = \sqrt{\frac{\sum_n \lambda_n^2 V_n}{4N_{DOF}}}. \tag{2.36}$$

Plugging Eq. (2.34) and Eq. (2.35) into Eq. (2.31) yields,

$$I_n + \frac{\lambda_n V_n}{2\mu} = \sum_i \omega_{n,i} f_{0i} e^{-\Sigma_n \lambda_n \omega_{n,i}}, \qquad n = 1, .., n_{max}. \tag{2.37}$$

Then plugging in Eq. (2.36) and simplifying,

$$I_n + \frac{\lambda_n V_n}{2\sqrt{\frac{\lambda_n^2 V_n}{4N_{DOF}}}} = \sum_i \omega_{n,i} f_{0i} e^{-\lambda_n \omega_{n,i}}$$

$$= I_n + \sqrt{V_n N_{DOF}} - \sum_i \omega_{n,i} f_{0i} e^{-\lambda_n \omega_{n,i}} = 0, \qquad n = 1, .., n_{max}. \tag{2.38}$$

The optimization problem has been reduced to a system of n_{max} equations with n_{max} unknowns, $\lambda_1, ...\lambda_{n_{max}}$. The collection of Lagrange multipliers, λ_n, in the set of equations expressed in Eq. (2.38) are derived by maximizing its potential function, Z, expressed below,

$$Z = -\sum_i f_{0i} e^{-\Sigma_n \lambda_n \omega_{n,i}} - \sqrt{N_{DOF} \sum_n \lambda_n^2 V_n} - \sum_n I_n \lambda_n. \tag{2.39}$$

Z must be less than zero and so instead of maximizing the above equation, the absolute value of Z is taken and minimized, which allows for numerical minimization methods to be used to determine the best fits for λ_n. Once the λ_n values are estimated, they are used along with Eq. (2.34) to determine the new spectra.

Chapter 3

Experimental Configuration

3.1 88-Inch Cyclotron

The 88-Inch Cyclotron at LBNL is a K140 sector-focused cyclotron with both light and heavy-ion capabilities [1]. It is used by the GENESIS project to send mono-energetic deuterons along the -20° beamline, as seen in Fig. 3.1, towards Cave 5 where the neutron spectrometer, GENESIS array, and other experimental setups are located. A neutron beam is produced by focusing the deuteron beam on a target (e.g. Ta, Be, or C) in the Vault. All experiments analyzed in this work use a 3.7 mm thick natural carbon plate as the deuteron target. The deuteron target is mounted on a Faraday cup to monitor charged-particle flux. The measured integrated charged particle current over the STOF operational time period for each experiment is recorded in Table 3.1. Past the deuteron target, there is a copper collimator placed at the entrance to the beamline from the Vault into Cave 5 (black box in the Vault). This collimator was present for all datasets; however, it was realigned between each dataset. After progressing into Cave 5, the neutron beam travels through the GENESIS array where a thin GENESIS target (black box in Cave 5) is placed to perform inelastic cross section measurements. Further past the GENESIS target, the STOF spectrometer (green box in Cave 5) is set up.

Dataset	14(^{56}Fe)	14(NaCl)	23(Al_2O_3)
Integrated Current [μC]	7915500	3663826	1179118

Table 3.1: Total integrated current measured over each experiment's STOF operating time interval using the Faraday cup with the deuteron target.

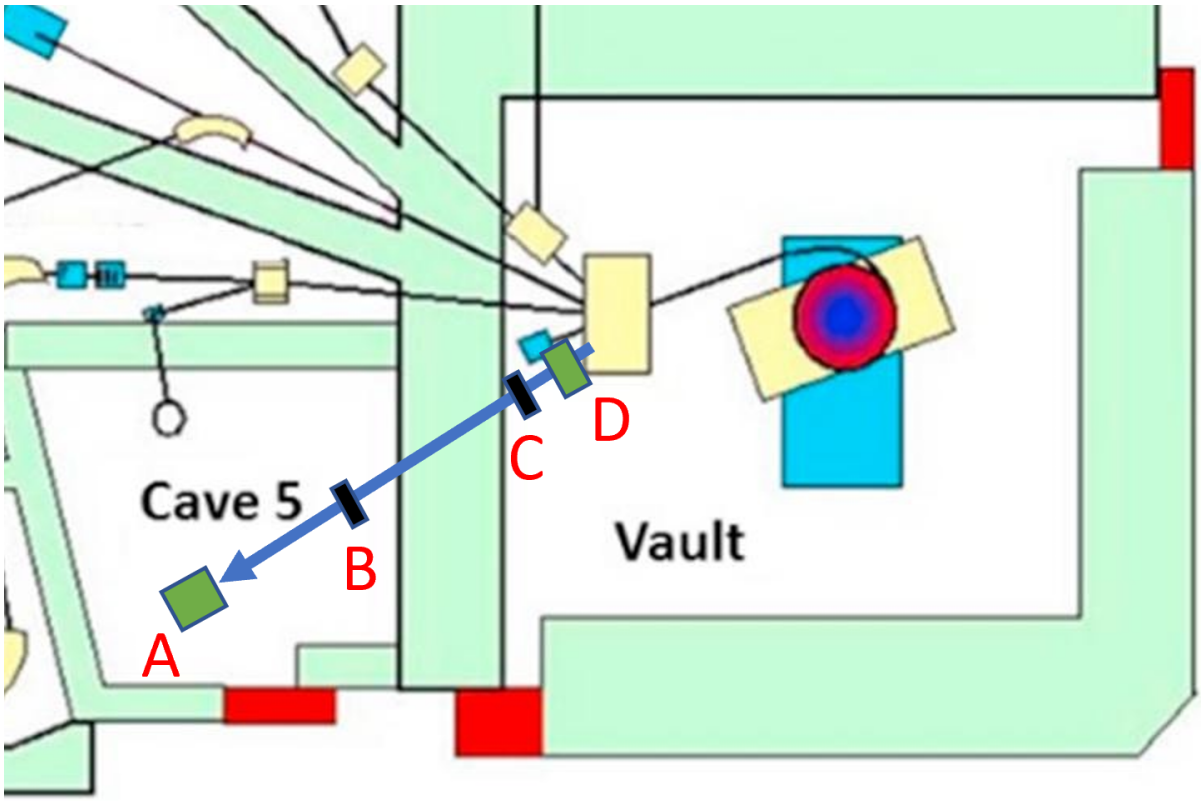

Figure 3.1: Layout of the 88-Inch Cyclotron at LBNL. The green box (D) in the Vault is the location of the deuteron breakup target. The black box (C) in the Vault is the location of a collimator. The blue line extending from the deuteron target (D) into Cave 5 is the neutron beam path. The black box (B) in Cave 5 is the GENESIS target. The green box (A) in Cave 5 is STOF.

3.2 Scatter Time of Flight System

3.2.1 Neutron Detectors

Organic scintillators are commonly produced in solid form (e.g. plastics and Stilbenes) or liquid forms (e.g. Eljen Technologies's, EJ-309). Liquid scintillators were used in this work because of their elevated resistance to neutron damage. Solid materials, with high enough flux and time, will exhibit radiation damage due to the development of discontinuities within the microstructure of the scintillator. This damage results in degraded timing and energy resolution of the detector. The lack of a solid crystalline structure in liquid scintillators means there is no mechanism for this type of radiation damage to occur within the scintillator itself, thus making them ideal for use in high flux environments.

EJ-309 liquid scintillators [30] were used as the detection medium for all detectors. The properties of EJ-309 provided by Eljen Technology are shown in Table 3.2. The in-beam

detector, referred to as the target cell, TC, consists of a dual-window scintillator with a PMT placed at each of the windows. A real interaction within the scintillator will produce two measured events, one from each PMT. There are two main benefits to this setup. The first is it improves timing. The timing resolution is dependent on multiple factors, one of them being the size of the scintillator. Light will take longer to reach the PMT and produce a signal if the scintillation event occurs on the side of the scintillator opposite of the PMT, therefore, for a single PMT-mounted scintillator there is a timing uncertainty related to the scintillator size. Using two PMTs on opposite ends of the scintillator allows for improved timing of the initial scatter event by averaging the timestamp between the two PMT events. Second, it enables the exclusion of non-scintillation events from the post-processing analysis. Since the target cell will be in the neutron beam, false signals can be generated from interactions between γ rays or neutrons within the PMT itself. Radiative particle interactions can ionize electrons within the PMT causing an electron cascade and subsequent amplification that did not result from the absorption of photons from scintillation. By gating on signals from both PMTs these false events that are generated in only one PMT are vetoed. The target cell scintillator is a 1.27 cm radius by 1.27 cm tall right cylinder, shown in Fig. 3.2. The out-of-beam detectors, referred to as scatter cells (SC), are single-window 1.27 cm radius by 2.54 cm right cylinders, as seen in Fig. 3.3. All the scintillators are housed within an aluminum frame.

Light Output (% Anthracene)	80
Scintillation Efficiency (photons/1 MeV e-)	12,300
Specific Gravity	0.959
No. of H Atoms per cm^3 ($x10^{22}$)	5.43
No. of C Atoms per cm^3 ($x10^{22}$)	4.35
No. of Electrons per cm^3 ($x10^{23}$)	3.16

Table 3.2: Properties of EJ-309 organic liquid scintillator [30].

The PMTs used are Hamamatsu H6533 photomultiplier assemblies [31]. They are coupled to the scintillators through a layer of EJ-550 optical grease. The scintillators and PMTs are attached through a custom-designed and 3D-printed Polylactic Acid (PLA) plastic holder. This holder is attached to a custom-designed and 3D-printed PLA plastic joint. The holders can be printed at various angles depending on the desired configuration. 90° joints are used for the target cell and 45° joints are used for the scatter cells. The holder/joint combinations (example shown in Fig. 3.4) are used to securely attach the detectors to the structural frame and are printed with a 50% fill density.

The detector assembly is bolted to a freestanding structure, constructed out of 80/20 bars (see Fig. 3.5). The scatter cells (out-of-beam detectors) are positioned around a hexagon frame. The hexagon is constructed out of 80/20 bars and custom-designed 3D-printed corner joints. The target cell is bolted to an 80/20 bar, itself attached to an 80/20 post.

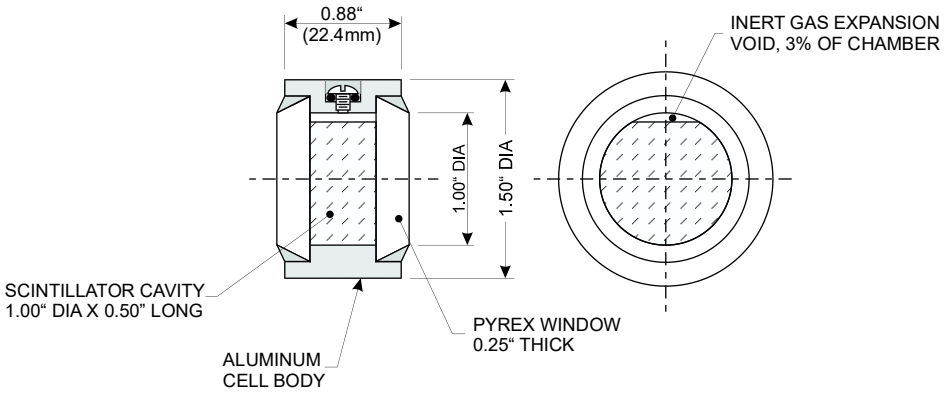

Figure 3.2: Engineering drawing of the EJ-309 scintillator used for the target cell in STOF.

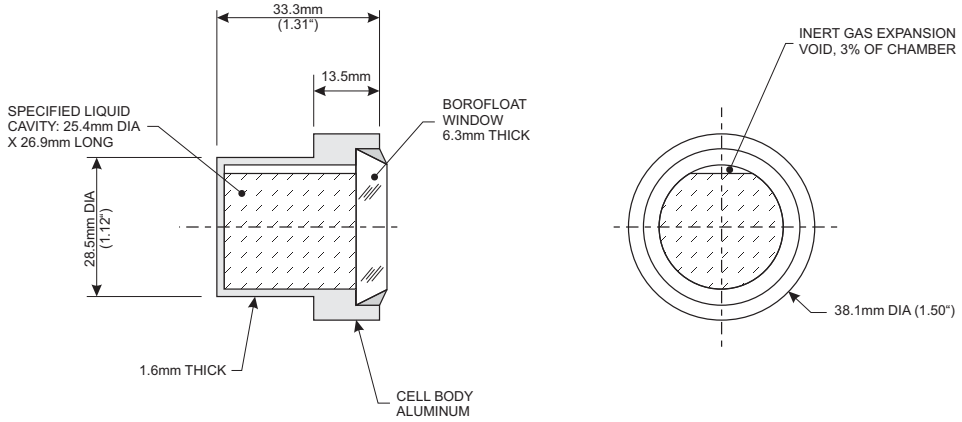

Figure 3.3: Engineering drawing of the EJ-309 scintillator used for the scatter cell in STOF.

Position measurements were taken with a Leica DISTO S910 [32] and a python script was used to determine precise angles and distances between the scatter cells and target cell and the precise distance between the target cell, the deuteron target, and the GENESIS target. The unique ID numbers given to each scatter cell are defined and shown in Fig. 3.6. The results of these measurements for each dataset are shown in Table 3.3.

These PMTs are powered with a negative bias using a CAEN R8033N 8-channel power supply [33]. All detectors in dataset 14(^{56}Fe)were visually gain-matched with an oscilloscope for a ^{137}Cs source Compton-edge pulse to correspond to a 50mV amplitude pulse. The same was done for the detectors in dataset 14(NaCl)but for a 170mV amplitude pulse. The detectors in dataset 23(Al_2O_3)were set to the same bias used in dataset 14(^{56}Fe). Table 3.4 shows the bias voltage used for each detector for each dataset.

Figure 3.4: 3D printed holder and joint combined. This is used to attach the PMT and scintillator to the structural frame of STOF. PLA is used as the printing material.

Dataset	14(^{56}Fe)	14(NaCl)	23(Al_2O_3)
Distance from TC to GENESIS target [m]	2.7306	2.9072	2.5919
Distance from TC to deuteron target [m]	10.0835	10.0516	10.06561
Distance from TC to SC #1 [m]	0.416	0.434	0.481
Distance from TC to SC #2 [m]	0.405	0.425	0.470
Distance from TC to SC #3 [m]	0.402	0.421	0.462
Distance from TC to SC #4 [m]	0.414	0.431	0.473
Angle between TC and SC #1 [degrees]	47.6	44.2	39.1
Angle between TC and SC #2 [degrees]	46.2	44.1	38.5
Angle between TC and SC #3 [degrees]	46.7	43.9	38.9
Angle between TC and SC #4 [degrees]	47.1	44.2	39.2

Table 3.3: Distance and angle measurements for each STOF configuration. All measurements were taken with a Leica DISTO S910 and corrected for center-to-center distances. See Fig. 3.6 for the details of the detector ID labels.

Figure 3.5: The STOF array consists of one target cell and four scatter cells arranged approximately 45 degrees from the beamline.

Detector	Dataset 14(^{56}Fe): Bias Voltage [V]	Dataset 14(NaCl): Bias Voltage [V]	Dataset 23(Al_2O_3): Bias Voltage [V]
TC1	1290	1465	1290
TC2	1550	1890	1550
SC1	1300	1545	1300
SC2	1250	1405	1250
SC3	1225	1380	1225
SC4	1300	1470	1300

Table 3.4: Voltage bias used for target cell (TC) PMTs and scatter cell (SC) PMTs. See Fig. 3.6 for the details of the detector ID labels.

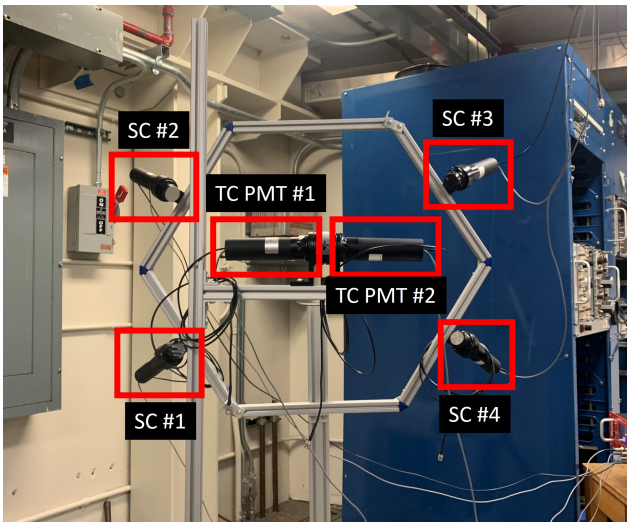

Figure 3.6: Upstream view of the STOF array. The scatter cells are distinguished with an ID number starting from the bottom left and moving clockwise, the ID numbers are SC1, SC2, SC3, and SC4. The target cell's PMTs are labeled, with the left PMT being TC1 and the right PMT being TC2. The same general configuration was used for each analyzed dataset and so the same IDs apply to every dataset.

3.3 Digital Acquisition Setup

The datasets were collected using a CAEN 5730S desktop digitizer [34] with CAEN's DPP-PSD [35] firmware. The CAEN Multi-PArameter Spectroscopy Software (CoMPASS) [36] software package (Linux version) was used to record and store the information and to set the various waveform processing settings. The information was stored as ROOT files. The CERN ROOT [37] data analysis framework stores event-wise data in a highly efficient and compact manner through the use of the ROOT TTree class.

The CoMPASS project settings for each data set are shown in Tables 3.5 to 3.7. Data was collected in LIST mode without recording waveforms. This was necessary as the rate in the target cell was high enough that the writing of event data with waveforms could not keep up and large losses of events due to the filling of the memory buffer in the digitizer were observed.

A brief description of applicable settings is described here, the full description of all possible settings can be found in the CoMPASS manual [36]. The "Record Length" is the size of the window used in the CoMPASS built-in digital oscilloscope, as well as the window that is recorded if waveforms are recorded. The "Pre-trigger" is the amount of time before an event trigger to start the "Record Length" window. The "N-samples baseline" is the number of samples the digitizer uses to estimate the baseline of an event pulse. The "DC Offset" is a percent magnitude adjustment of an event pulse. Setting this value to non-zero ensures that a pulse does not dip below the lowest acceptable voltage of the digitizer. Any

part of the pules that falls below the minimum acceptable voltage is not recorded, which will result in inaccurate measurements of the event, such as the pulse integral. The "Input Dynamic" is set to the maximum voltage that the digitizer can accept.

The digitizer was run using the built-in Constant Fraction Discrimination (CFD) mode. The "CFD Threshold" is set using the digitizer internal units referred to as Least Significant Bit (LSB) which are directly proportional to the voltage of the measured pulse. This was set to minimize the accumulation of events associated with noise. The "Trigger Holdoff" is the amount of time from a triggered event that the digitizer does not accept a new pulse as a separate event. This value was set so that it was slightly longer than the endpoint of the "Gate" setting. The "CFD Delay" is the amount of time that a pulse is delayed when performing CFD. After testing with multiple values no discernible difference with the CFD functionality was found so it was set to the default value.

The "Energy Coarse Gain" sets the scale for the signal charge. This was set to the lowest setting to minimize the saturation of the pulse integral values. The "Gate," commonly called the long gate, is the width used by the digitizer to calculate the integral of the accepted pulse. This value was set to a value longer than the accepted pulses. The "Short Gate" is the range used by the digitizer to calculate the integral from the beginning of the pulse to a time less than that of the long gate. This value is used to create the shape parameter used for the PSD analysis. The "Pre-Gate" is the parameter used to set the start time of the "Gate" and "Short Gate." The input is the number of nanoseconds before the trigger time. The CAEN digitizer has the following required relation between the "Pre-trigger" setting and the "Pre-Gate" setting,

$$\text{Pre-gate} \leq \text{Pre-trigger} - 32[ns] \tag{3.1}$$

If the relation in Eq. (3.1) does not hold true, then the firmware automatically adjusts the "Pre-Gate" setting until the relation is met. The "Energy N Channels" sets the maximum number of channels used for the CoMPASS code live energy (pulse integral) spectra plots. Importantly, this value also sets the maximum value the software will set for a recorded pulse integral. Additionally, the realtime of each STOF measurement was recorded with CoMPASS and is listed in Table 3.8.

Detector PMT	TC1	TC2	SC1	SC2	SC3	SC4
CoMPASS Input Settings						
Record Length [ns]	336	336	336	336	336	336
Pre-trigger [ns]	40	40	40	40	40	40
N-samples baseline [samples]	256	256	256	256	256	256
DC Offset [%]	20	20	20	20	20	20
Input Dynamic [V_{pp}]	2	2	2	2	2	2
Discriminator Settings						
Mode	CFD	CFD	CFD	CFD	CFD	CFD
CFD Threshold [LSB]	40	40	40	40	40	40
Trigger Holdoff [ns]	296	296	296	296	296	296
CFD Delay [ns]	4	4	4	4	4	4
QDC Settings						
Energy Coarse Gain [$\frac{fC}{LSB*V_{pp}}$]	2.5	2.5	2.5	2.5	2.5	2.5
Gate [ns]	300	300	300	300	300	300
Short Gate [ns]	18	18	18	18	18	18
Pre-Gate [ns]	50 (8)	50 (8)	50 (8)	50 (8)	50 (8)	50 (8)
Spectra Settings						
Energy N channels	4096	4096	4096	4096	4096	4096

Table 3.5: CoMPASS settings used for each detector in Dataset 14(^{56}Fe). See Fig. 3.6 for the details of the detector ID labels. For the "Pre-Gate" setting, the value outside the parentheses was the user-inputted setting, and the value inside the parentheses is the value used due to the firmware auto-adjustment.

Detector PMT	TC1	TC2	SC1	SC2	SC3	SC4
CoMPASS Input Settings						
Record Length [ns]	336	336	336	336	336	336
Pre-trigger [ns]	40	40	40	40	40	40
N-samples baseline [samples]	256	256	256	256	256	256
DC Offset [%]	5	5	5	5	5	5
Input Dynamic [V_{pp}]	2	2	2	2	2	2
Discriminator Settings						
Mode	CFD	CFD	CFD	CFD	CFD	CFD
CFD Threshold [LSB]	100	100	100	100	100	100
Trigger Holdoff [ns]	296	296	296	296	296	296
CFD Delay [ns]	4	4	4	4	4	4
QDC Settings						
Energy Coarse Gain [$\frac{fC}{LSB*V_{pp}}$]	2.5	2.5	2.5	2.5	2.5	2.5
Gate [ns]	300	300	300	300	300	300
Short Gate [ns]	22	22	22	22	22	22
Pre-Gate [ns]	50 (8)	50 (8)	50 (8)	50 (8)	50 (8)	50 (8)
Spectra Settings						
Energy N channels	4096	4096	4096	4096	4096	4096

Table 3.6: CoMPASS settings used for each detector in Dataset 14(NaCl). See Fig. 3.6 for the details of the detector ID labels. For the "Pre-Gate" setting, the value outside the parentheses was the user-inputted setting, and the value inside the parentheses is the value used due to the firmware auto-adjustment.

Detector PMT	TC1	TC2	SC1	SC2	SC3	SC4
CoMPASS Input Settings						
Record Length [ns]	1296	1296	1296	1296	1296	1296
Pre-trigger [ns]	48	48	48	48	48	48
N-samples baseline [samples]	256	256	256	256	256	256
DC Offset [%]	5	5	5	5	5	5
Input Dynamic [V_{pp}]	2	2	2	2	2	2
Discriminator Settings						
Mode	CFD	CFD	CFD	CFD	CFD	CFD
CFD Threshold [LSB]	100	100	100	100	100	100
Trigger Holdoff [ns]	296	296	296	296	296	296
CFD Delay [ns]	4	4	4	4	4	4
QDC Settings						
Energy Coarse Gain [$\frac{fC}{LSB*V_{pp}}$]	2.5	2.5	2.5	2.5	2.5	2.5
Gate [ns]	300	300	300	300	300	300
Short Gate [ns]	22	22	22	22	22	22
Pre-Gate [ns]	50 (6)	50 (6)	50 (6)	50 (6)	50 (6)	50 (6)
Spectra Settings						
Energy N channels	4096	4096	4096	4096	4096	4096

Table 3.7: CoMPASS settings used for each detector in Dataset 23(Al_2O_3). See Fig. 3.6 for the details of the detector ID labels. For the "Pre-Gate" setting, the value outside the parentheses was the user-inputted setting, and the value inside the parentheses is the value used due to the firmware auto-adjustment.

Dataset	Realtime [s]
14(^{56}Fe)	394108
14(NaCl)	316940
23(Al_2O_3)	399701

Table 3.8: Recorded realtimes for each dataset. Value comes from CoMPASS.

3.4 Activation Foil Setup

3.4.1 Foil Configuration

Each dataset also has an associated foil activation experiment and analysis. A foil pack was made for each experiment and placed at the GENESIS target location. Table 3.9 shows the foils and placement order used for each foil pack. Tables 3.10 to 3.12 list the properties of each foil within each pack.

Dataset	Foils in order from deuteron target to STOF
14(^{56}Fe)	Zirconium, Nickel, Indium, Aluminum, and Gold
14(NaCl)	Gold, Aluminum, Indium, and Nickel
23(Al_2O_3)	Gold, Aluminum, Indium, Zirconium, and Nickel

Table 3.9: List of foils used for each dataset and the order they were positioned in.

Foil	Mass[g]	thickness [mm]	Composition
Indium	14.37	1	natural
Nickel	17.22	1	natural
Aluminum	5.32	1	natural
Zirconium	13.00	1	natural
Gold	0.28	0.025	natural

Table 3.10: Properties of the foils used for the activation experiment for dataset 14(^{56}Fe). The gold is a 2.54 cm square foil and the rest are 5 cm-diameter circular foils.

Foil	Mass[g]	thickness [mm]	Composition
Indium	14.37	1	natural
Nickel	17.13	1	natural
Aluminum	5.37	1	natural
Gold	0.28	0.025	natural

Table 3.11: Properties of the foils used for the activation experiment for dataset 14(NaCl). The gold is a square foil and the rest are circular foils.

3.4.2 Counting Station

All gamma-ray measurements were obtained using the same 50% Poptop ORTEC HPGe detector [38], detector settings, and setup. The HPGe detector was biased to -4000V, and

Foil	Mass[g]	thickness [mm]	Composition
Indium	14.37	1	natural
Nickel	17.30	1	natural
Aluminum	5.32	1	natural
Zirconium	13.00	1	natural
Gold	0.28	0.025	natural

Table 3.12: Properties of the foils used for the activation experiment for dataset 23(Al_2O_3). The gold is a square foil and the rest are circular foils.

cooled with liquid nitrogen. It is in a vertical configuration within a 10 cm thick lead box. All calibration sources and foils were placed 10 cm from the detector face on a thin-walled plastic housing, as shown in Fig. 3.7.

All spectra were collected using the GammaVision Maestro [39] data acquisition software. The collected data was analyzed using a combination of Fitzpeaks [40] and python scripts.

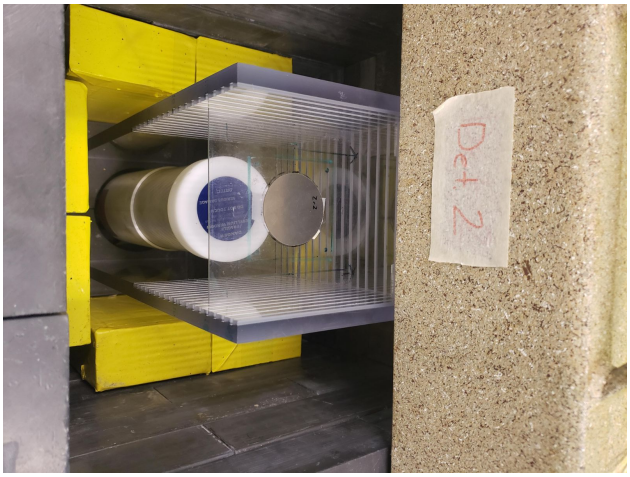

Figure 3.7: Picture of the HPGe detector setup used to measure gamma rays from in-beam activated foils. The detector is in a vertical configuration with a plastic shelving unit on top. In this picture, a zirconium foil is on the shelf. The detector is inside a lead box with a lead lid that can be rolled closed or open.

Chapter 4

Data Analysis and Processing

4.1 Scatter Time-of-Flight

A C++ based post-processing analysis framework of the raw data collected by CoMPASS was developed and integrated as part of the Bay Area Neutron Group's NSD-Rootscripts library [41]. A simulation using GEANT4 was also used for various parts of the analysis. The same Geant4 model and simulated beam profile were used for all sections that used simulated datasets. The GEANT4 model for dataset 14(^{56}Fe) is shown in Fig. 4.1. Note, the density used for the EJ309 liquid was reduced by 3% to account for the 3% bubble void within the scintillator. This same model, with the appropriate distance and angle configuration from Table 3.3, was used for each dataset. The simulated neutron beam consisted of uniformly distributed neutron energies from 0 to 32 MeV. The beam was a rectangular, parallel beam that perfectly filled the cross-sectional size of the target cell's scintillator. The model does not include the walls, floor, roof, and structural 80/20 material. As of such, coincidences due to room return are not accounted for in this model. These background events are small compared to the flux uncertainty. The events are recorded in CERN ROOT files and then analyzed using C++. The same simulated events are used for each analysis, with variations in how the events are tallied depending on the analysis. The details of how the tallies were done are further described in the appropriate analysis section.

The long-gate and short-gate values recorded by CoMPASS for each event represent the integral of the waveform received by the digitizer. This integral is directly proportional to the light yield absorbed by the PMT. The long gate represents the total light yield, while the short gate represents a subset of the total light yield, consisting primarily of the waveform peak. For this work, the term light yield (LY), in arbitrary units, is used to refer to the recorded pulse integral values.

The various individual detectors are referred to by a detector ID: TC1, TC2, SC1, SC2, SC3, or SC4. The corresponding detector each of these IDs is referring to is discussed in Section 3.2.1.

Numerous parameters from histograms were calculated in this section of analysis. If a fit

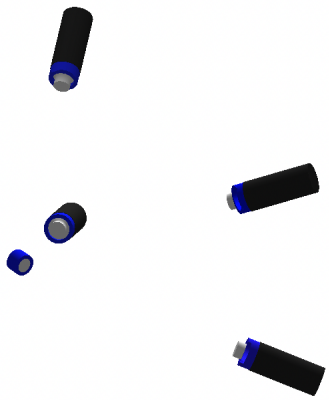

Figure 4.1: Geant4 Model for dataset 14(^{56}Fe). The blue colored objects are the 3D-printed holders, the black objects are the PMTs, and the gray objects are the scintillator and its aluminum housing.

was performed, e.g. a Gaussian and/or N^{th}-order polynomial fit, the default CERN ROOT fitting routine was used. This function uses the Minuit2 minimizer package to estimate parameters as well as appropriate uncertainties. If a fit was not stated to be used, then a mean and/or σ value was estimated from the histogram using the ROOT [37] TH1:GetMean() and/or TH1:GetStdDev() functions.

4.1.1 Distance and Angle Determination

The determination of the distance and scattering angle between the target cell (TC) and the scatter cells (SC) is non-trivial. It is not self-evident that the distance and angle between the center of the cylindrical TC and the center of the cylindrical SC is the mean distance and angle at which neutrons will travel. To determine the mean distance and scattering angle, a quasi-ray-tracing method was employed using the GEANT4 simulated events.

All distances and scatter angles of single scattered neutrons that interacted within the TC and then interacted in an SC without scattering on air or the scintillator housing were tallied into a histogram for each SC, as shown in Figs. 4.2 to 4.7. The means for these histograms are tabulated in Tables 4.1 to 4.3. All means of the simulated distances and angles differ up to 3.8% and 5.1% of the distances and angles determined by the laser measurements described in Section 3.2. The simulated mean distances and angles are used in this analysis.

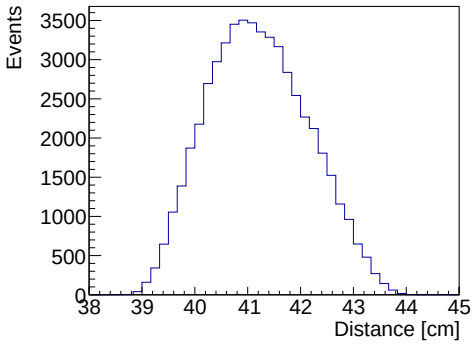

(a) Neutron travel distances between the TC and SC1.

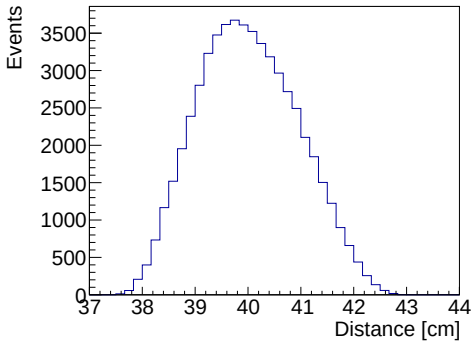

(b) Neutron travel distances between the TC and SC2.

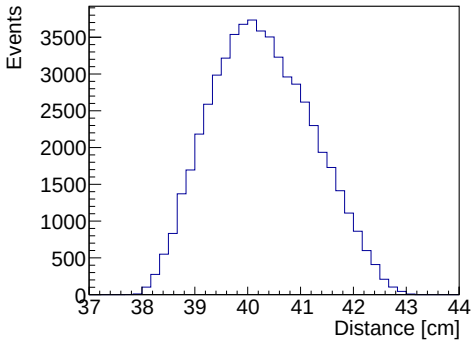

(c) Neutron travel distances between the TC and SC3.

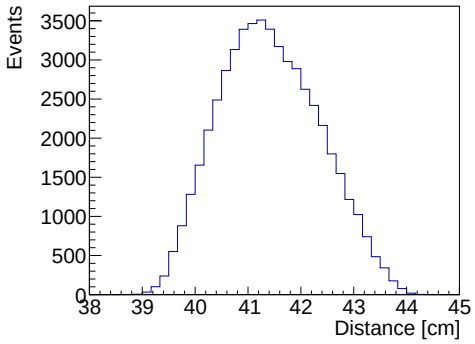

(d) Neutron travel distances between the TC and SC4.

Figure 4.2: Neutron travel distances between the TC and each SC for single scattered neutrons as determined by GEANT4. Model configuration is from dataset 14(^{56}Fe).

Det. ID	Distance [cm]	Angle [degrees]
SC1	41.20	47.01
SC2	40.01	46.66
SC3	40.28	46.17
SC4	41.42	47.62

Table 4.1: Mean of the tallied neutron scatter distance between the TC and each SC (see Fig. 4.2) and the mean of the tallied neutron scatter angle between the beamline and each SC (see Fig. 4.3) in dataset 14(^{56}Fe).

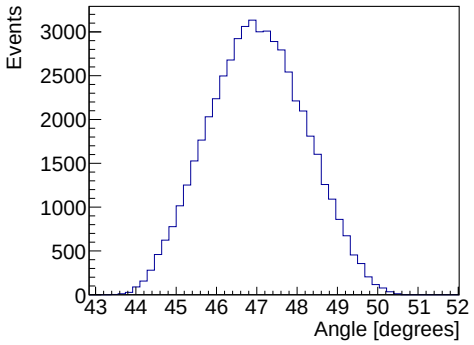

(a) Neutron scattering angle between the TC and SC1.

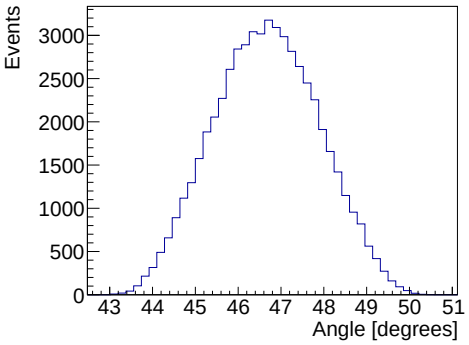

(b) Neutron scattering angle between the TC and SC2.

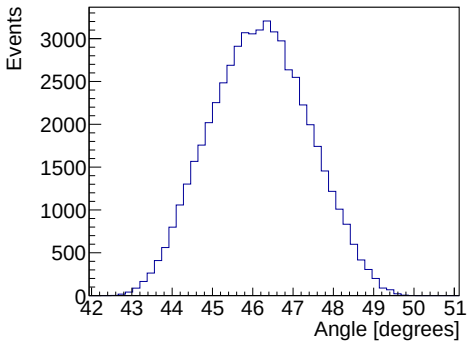

(c) Neutron scattering angle between the TC and SC3.

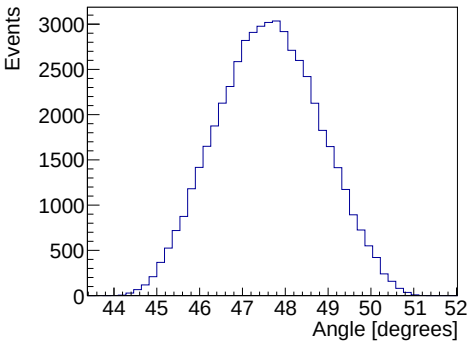

(d) Neutron scattering angle between the TC and SC4.

Figure 4.3: Neutron scattering angle between the TC and each SC for single scattered neutrons as determined by GEANT4. The scattering angle is relative to the beam line center. Model configuration is from dataset 14(^{56}Fe).

Det. ID	Distance [cm]	Angle [degrees]
SC1	44.38	42.17
SC2	43.44	41.82
SC3	43.79	41.96
SC4	44.72	42.13

Table 4.2: Mean of the tallied neutron scatter distance between the TC and each SC (see Fig. 4.4) and the mean of the tallied neutron scatter angle between the beamline and each SC (see Fig. 4.5) in dataset 14(NaCl).

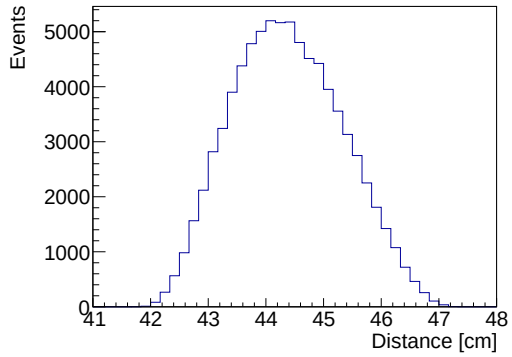

(a) Neutron travel distances between the TC and SC1.

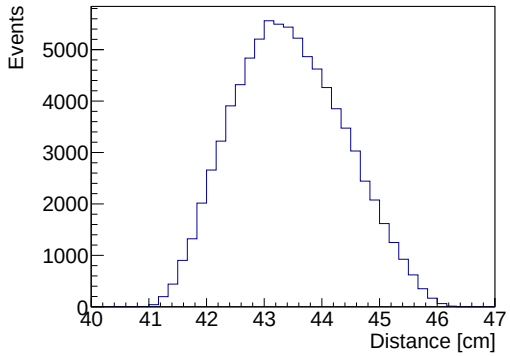

(b) Neutron travel distances between the TC and SC2.

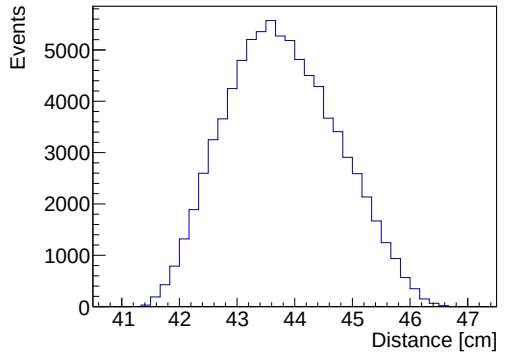

(c) Neutron travel distances between the TC and SC3.

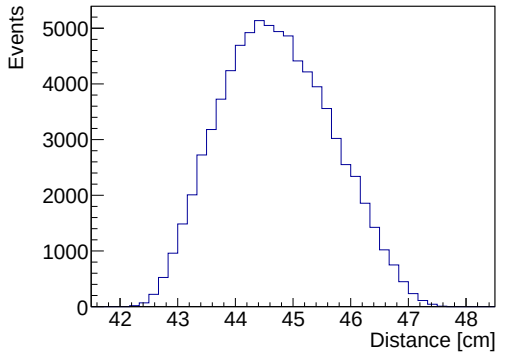

(d) Neutron travel distances between the TC and SC4.

Figure 4.4: Neutron travel distances between the TC and each SC for single scattered neutrons as determined by GEANT4. Model configuration is from dataset 14(NaCl).

Det. ID	Distance [cm]	Angle [degrees]
SC1	47.08	39.20
SC2	46.01	38.90
SC3	46.83	38.56
SC4	47.97	39.14

Table 4.3: Mean of the tallied neutron scatter distance between the TC and each SC (see Fig. 4.6) and the mean of the tallied neutron scatter angle between the beamline and each SC (see Fig. 4.7) in dataset 23(Al_2O_3).

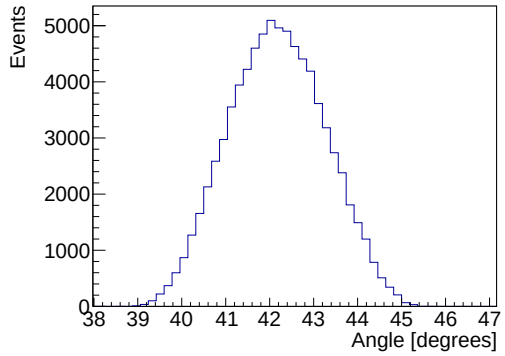

(a) Neutron scattering angle between the TC and SC1.

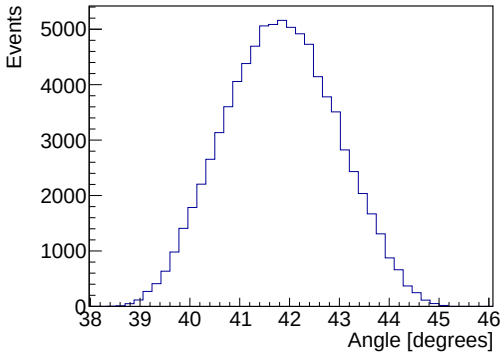

(b) Neutron scattering angle between the TC and SC2.

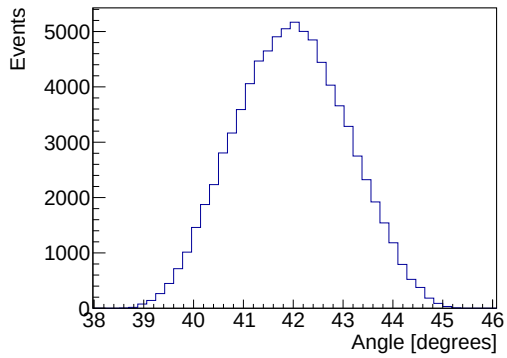

(c) Neutron scattering angle between the TC and SC3.

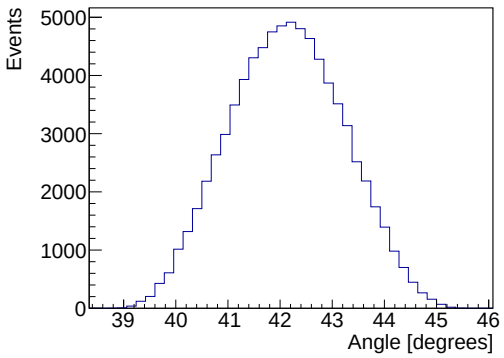

(d) Neutron scattering angle between the TC and SC1.

Figure 4.5: Neutron scattering angle between the TC and each SC for single scattered neutrons as determined by GEANT4. The scattering angle is relative to the beam line center. Model configuration is from dataset 14(NaCl).

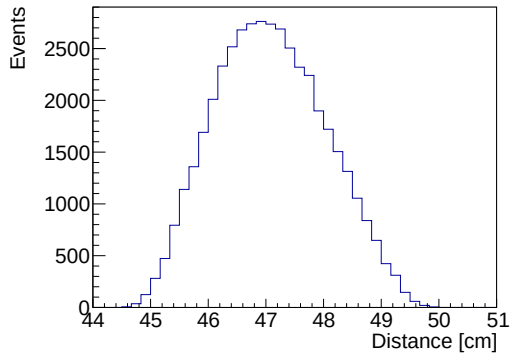

(a) Neutron travel distances between the TC and SC1.

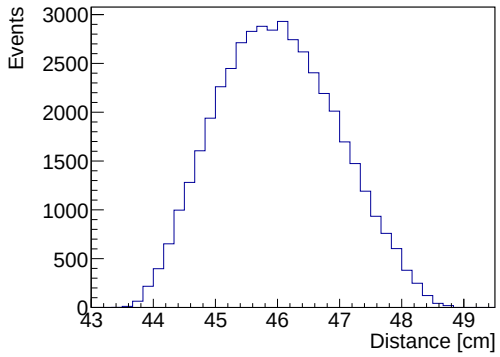

(b) Neutron travel distances between the TC and SC2.

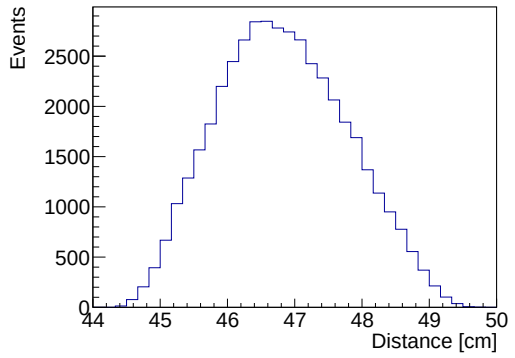

(c) Neutron travel distances between the TC and SC3.

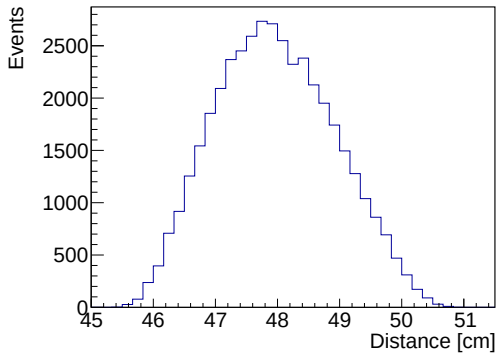

(d) Neutron travel distances between the TC and SC4.

Figure 4.6: Neutron travel distances between the TC and each SC for single scattered neutrons as determined by GEANT4. Model configuration is from dataset 23(Al_2O_3).

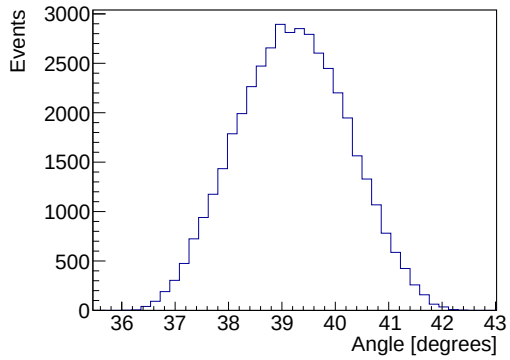

(a) Neutron scattering angle between the TC and SC1.

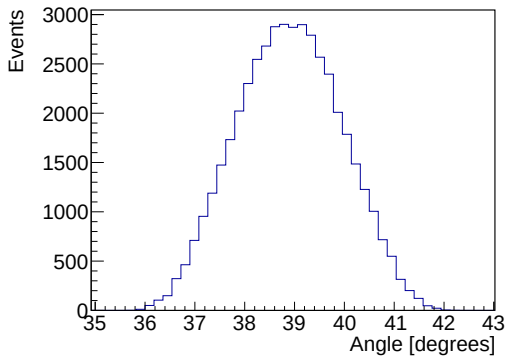

(b) Neutron scattering angle between the TC and SC2.

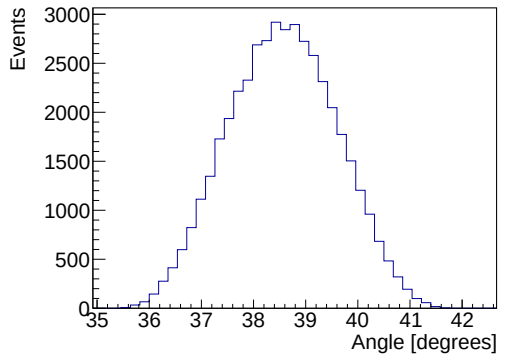

(c) Neutron scattering angle between the TC and SC3.

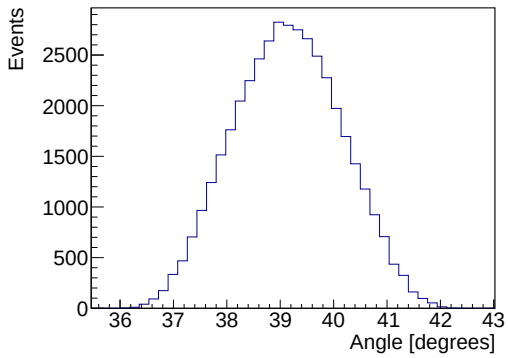

(d) Neutron scattering angle between the TC and SC4.

Figure 4.7: Neutron scattering angle between the TC and each SC for single scattered neutrons as determined by GEANT4. The scattering angle is relative to the beam line center. Model configuration is from dataset 23(Al_2O_3).

4.1.2 CoMPASS Singles Event Processing

Every recorded event has an associated "flag" value. This is a 32-bit integer, where each bit corresponds to a true or false statement about the event. Two types of flagged events are outright rejected from all further analysis: the pile-up flag and the input-saturation flag.

The pile-up flag is triggered when the built-in pile-up rejection algorithm is triggered. This algorithm relies on one input user parameter, the PUR value, set in CoMPASS. This value was set conservatively high to ensure that no real events were accidentally recorded as pile-up events. The result of this is some pile-up events populate the datasets; however, some of these additional pile-up events not caught by the CoMPASS algorithm are rejected by using pulse shape discrimination as described in Section 4.1.4. Tables 4.4 to 4.6 show the percentage of rejected events due to this flag for each detector.

The input-saturation flag is triggered when a signal is received by the digitizer whose amplitude is larger than what the digitizer is capable of recording. This results in a pulse that is "clipped." The CFD of such pulses behaves abnormally, and so the recorded timestamp for these pulses cannot be trusted. These events only correspond to large energy deposits. As such, the biases for all three datasets were chosen to limit clipped events. Tables 4.4 to 4.6 show the percent of rejected events due to this flag are small ($<0.2\%$).

The last relevant flag is the gate-saturation flag. The maximum value that CoMPASS stores for the pulse integral is 16384. However, this maximum value can be manually lowered to a user-selected value by setting the "Energy N channels" setting within the "Spectra Tab" of the software. The CoMPASS software defaults this setting to 4096. The default value was used for all three datasets. The recorded LY values are, therefore, capped at 4096. As outlined in Section 4.1.6, for datasets 14(^{56}Fe) and 23(Al_2O_3) the biases were low enough that this makes no impact on the analysis. However, the set bias for dataset 14(NaCl) was high enough that at the higher end of the spectrum, real events were capped at 4096. To achieve flux values for the high end of the energy spectrum, events flagged as gate-saturation were included for dataset 14(NaCl). These events are included because most of them ($>98.5\%$ across all detectors) are not flagged as input-saturation events, see Table 4.7. Events that are flagged as gate-saturating but not as input-saturating are not clipping, and so the recorded timestamp can be trusted. However, because the LY is unknown for these events, they have to be excluded from any event cuts that rely on this value. This means that there is a higher background for the spectrum resulting from dataset 14(NaCl).

Det.	Total	Gate-saturation (%)	Input-saturation (%)	Pilup (%)
TC1	5456732520	3343216 (0.0613)	374 (6.85e-6)	991382 (1.82e-2)
TC2	5485261940	3037740 (0.0554)	323 (5.89e-06)	987659 (1.80e-2)
SC1	29986197	12681 (0.0423)	83 (2.77e-4)	360 (1.20e-3)
SC2	34825212	28721 (0.0825)	29 (8.33e-5)	21 (6.03e-5)
SC3	34072712	24478 (0.0718)	185 (5.43e-4)	19 (5.58e-5)
SC4	33280417	29631 (0.0890)	273 (8.20e-4)	739 (0.00222)

Table 4.4: Total number of events and total number of flagged events recorded for each detector in dataset 14(^{56}Fe). The (%) represents the percent of recorded events with that flag in that detector.

Det.	Total	Gate-saturation (%)	Input-saturation (%)	Pilup (%)
TC1	12042655845	936828852 (7.78)	9787541 (0.0813)	13175220 (0.109)
TC2	12356817233	1028100987 (8.32)	14357604 (0.116)	15922780 (0.129)
SC1	57953481	2073941 (3.58)	19902 (0.0343)	2129 (0.00367)
SC2	73210926	1730283 (2.36)	4336 (0.00592)	382 (5.22e-4)
SC3	57026222	2152879 (3.78)	20582 (0.0361)	147 (2.58e-4)
SC4	56430983	2197566 (3.89)	29891 (0.0530)	6875 (0.0122)

Table 4.5: Total number of events and total number of flagged events recorded for each detector in dataset 14(NaCl). The (%) represents the percent of recorded events with that flag in that detector

Det.	Total	Gate-saturation (%)	Input-saturation (%)	Pilup (%)
TC1	8278942223	57483708 (0.694)	263 (3.18e-6)	8904662 (0.108)
TC2	8217588108	45091643 (0.549)	75 (9.13e-7)	7204155 (0.0877)
SC1	32027662	67551 (0.211)	1160 (0.00362)	1512 (0.00472)
SC2	38716497	392714 (1.01)	413 (0.00107)	26957 (0.0696)
SC3	39079963	342935 (0.878)	270 (6.91e-4)	25587 (0.0655)
SC4	38794717	330483 (0.852)	192 (4.95e-4)	22562 (0.0582)

Table 4.6: Total number of events and total number of flagged events recorded for each detector in dataset 23(Al_2O_3). The (%) represents the percent of recorded events with that flag in that detector

Det.	Gate-saturation	Input-saturation and Gate-saturation (%)
TC1	936828852	9784442 (1.04)
TC2	1028100987	14352624 (1.40)
SC1	2073941	19894 (0.959)
SC2	1730283	4336 (0.251)
SC3	2152879	20582 (0.956)
SC4	2197566	29891 (1.36)

Table 4.7: Total number of flagged gate-saturated events and total number of flagged input-saturated events that are also flagged as gate-saturated in dataset 14(NaCl). The (%) represents the percent of gate-saturated events that are also input-saturated for each detector.

4.1.3 Target Cell Events

The target cell (TC) consists of a single scintillator cell connected to two photomultiplier tubes (PMT). Every real event that occurs in the TC has two measured events. The delta time relation between the two TC PMT events is plotted in Fig. 4.8 for each dataset. As observed in this figure, all the TC events are present within a 5 nanoseconds time window. Target cell events are merged by iterating through the events of TC1 and finding the closest TC2 event within a 5 nanosecond time window. Each merged event is given new timestamps, long-gate LY values, and the short-gate LY values. The new timestamp, TS_{new} is averaged as follows,

$$TS_{new} = \frac{TS_1 + TS_2}{2}, \tag{4.1}$$

where TS_1 is the TC1 timestamp and TS_2 is the TC2 timestamp.

The new long and short LY values, LY_{new} are combined, as recommended in Knoll chapter 10 section C.1 [42], by using geometric averaging,

$$LY_{new} = \sqrt{LY_1 * LY_2}, \tag{4.2}$$

where LY_1 is the TC1 LY and LY_2 is the TC2 LY.

Each event that is not paired was rejected as a false event. Such false events occur due to ionization within one PMT caused by incident radiation. This is specifically prominent with the TC PMTs because they are within the beam itself. This effect is negligible in the scatter cells that are outside the beam and far from large potential scattering sources (e.g. the floor and the walls). Table 4.8 shows the percentage of rejected TC1 and TC2 events due to this timing cut.

All parts of the analysis henceforth use these consolidated TC events.

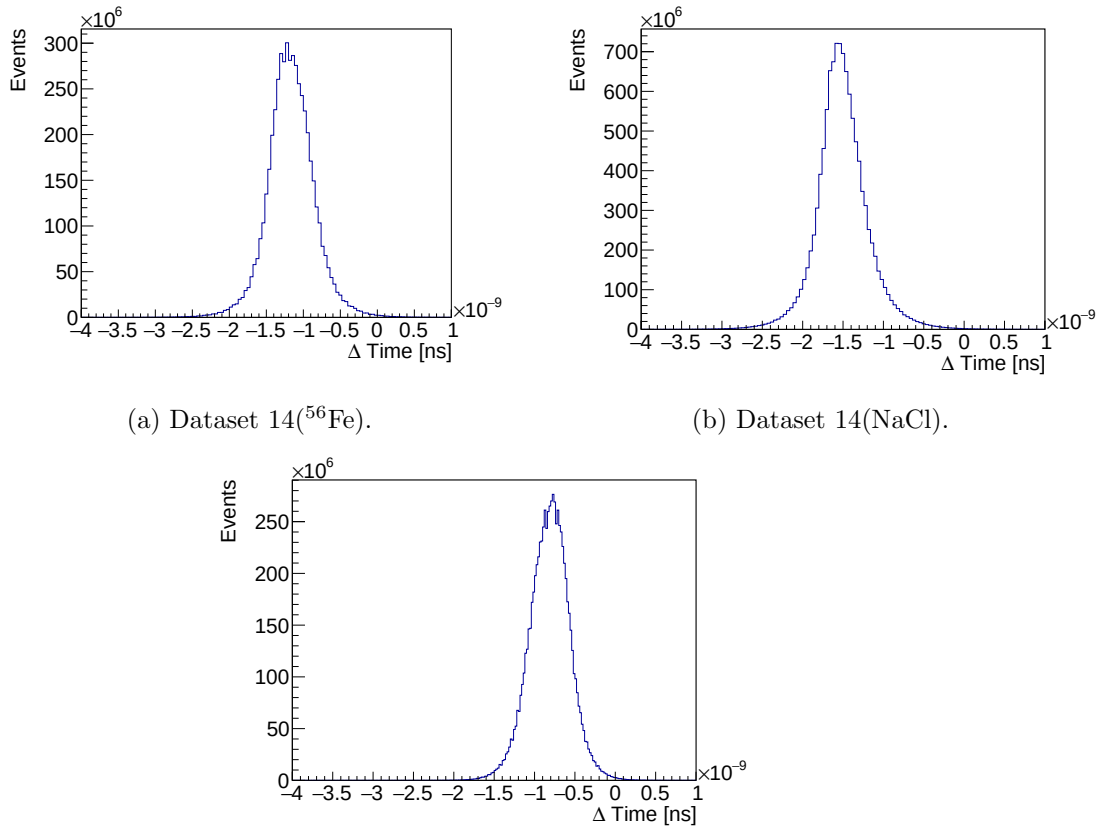

(a) Dataset 14(^{56}Fe).

(b) Dataset 14(NaCl).

(c) Dataset 23(Al_2O_3).

Figure 4.8: The timestamp difference between a TC1 and TC2 within a 10 nanosecond window for each dataset.

Dataset	Total TC Events	% TC1 Events Rejected	% TC2 Events Rejected
14(^{56}Fe)	5167600587	5.30	5.79
14(NaCl)	11418299027	5.19	7.60
23(Al_2O_3)	7963157229	3.81	3.10

Table 4.8: Total number TC events for each dataset. Percent of TC1 and TC2 events that are of rejected.

4.1.4 Pulse Shape Discrimination

For the following Pulse Shape Discrimination (PSD) analysis, all events flagged as pileup, input-saturation, and gate-saturation (see Section 4.1.2) are excluded.

PSD is a data analysis technique where measured events are distinguished based on particle type by the shape of the measured waveforms. The difference in pulse shapes occurs primarily due to a difference between prompt and delayed fluorescence (see Section 2.1.2). A PSD shape parameter, Tail-over-Total, is calculated from each detected event as follows,

$$\text{Tail-over-Total} = \frac{LY_{long} - LY_{short}}{LY_{long}}, \tag{4.3}$$

where LY_{long} is the recorded long-gate LY and LY_{short} is the recorded short-gate LY. This ratio, when plotted against the long-gate LY, produces a PSD plot. Two example PSD plots from the 14(^{56}Fe) dataset are shown in Fig. 4.9. Figure 4.9a consists of all TOF coincidences between a target cell (TC) event and all scatter cell (SC) events within a 100 nanosecond time window. Figure 4.9b consists of all TOF coincidences between a TC event and a SC1 event within a 100 nanosecond time window. The x-axis for both figures is the LY within the TC for each coincidence.

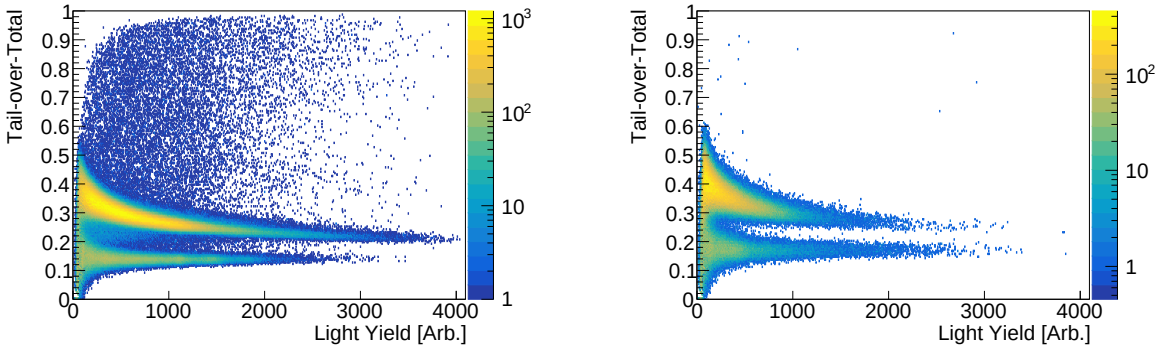

(a) PSD plot of all TOF coincidences between the TC and all SCs. The x-axis is the LY in the TC.

(b) PSD plot of all TOF coincidences between the TC and SC1. The x-axis is the LY in the SC1.

Figure 4.9: PSD Plots from the 14(^{56}Fe) Dataset. Only events that are included within TOF coincidences between a TC and SC within 100 nanoseconds are filled in the histogram.

A clear γ band (bottom band) is distinguishable from the neutron band (top band). From these PSD histograms a γ band cut can be fitted. Vetoing the γ events will reduce the background within the characterized neutron flux. Additionally, gating on the γ events is critical for determining an accurate timing calibration and timing resolution.

For the TC PSD plot, plotted in Fig. 4.9a, a PSD-dependent and LY-dependent background spread is visible above the neutron band. These events are due to pileup

events that made it past the built-in CoMPASS pileup rejection algorithm, as described in Section 4.1.2. For all datasets, waveforms were not taken due to memory overflow limitations. While these events cannot be shown as pileup events by reviewing the waveforms, an inference with a high degree of confidence can be made. Figure 4.9b shows this background is nearly non-existent in SC1, which holds for all SCs, as shown in Fig. 4.12. The SCs are positioned outside the beam and so experience an event rate that is orders of magnitude smaller than the in-beam TC. This, combined with the large PUR parameter, outlined in Section 4.1.2, indicates that this background is due to pileup. This effect is observed in all collected datasets, see Figs. 4.13 to 4.15. Since these events are pileup, vetoing as many as possible without removing valid neutron events further reduces the background. Therefore, a cut of the events above the neutron band for all TC events is also made.

To find these PSD cuts the histogram is sliced at various points along the x-axis. Each resulting y-projection was fitted either to a double Gaussian distribution or a single Gaussian distribution. Two example projections and the resulting fits are shown in Fig. 4.10. The projection in Fig. 4.10b is fitted to two Gaussians and the projection in Fig. 4.10a is fitted to a single Gaussian.

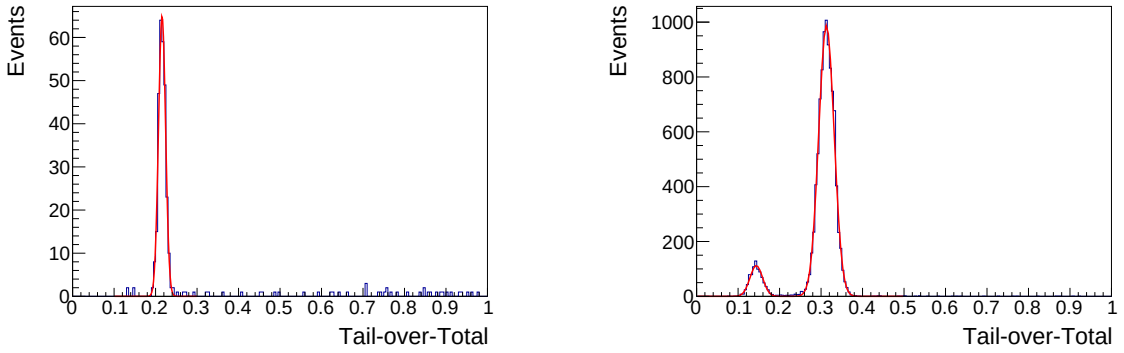

(a) Y-projection slice at a LY value of 3000.

(b) Y-projection slice at a LY value of 750.

Figure 4.10: Y-projections taken from Fig. 4.9a.

The means and sigmas for each fitted Gaussian are calculated for each slice. Five arrays of points are calculated. Two are arrays of the mean values of the neutron band and the γ band. Another array is the mean values of the neutron band plus 7σ. The last two arrays are the means of the γ bands plus and minus 3σ. The PSD cuts for all LY values up to 4096 were found. If the band ended before reaching 4096 then the last array values were copied and extended along the LY axis up to 4096. Each series of points is then fitted to an N^{th}-order polynomial of the form,

$$\Sigma_i A_i * x_{LY}^i, \tag{4.4}$$

where A_i is each fitted parameter, x_{LY} is the LY, and i is an integer from 0 to the N^{th} order. The results for datasets 14(^{56}Fe), 14(NaCl), and 23(Al_2O_3) are plotted in Figs. 4.11 and 4.12, Figs. 4.13 and 4.14, and Figs. 4.15 and 4.16 respectively. The red lines are the fitted PSD cuts and the fitted mean line. The black dots are the points used for each red line fit. The fitted parameters for each PSD cut for each detector for datasets 14(^{56}Fe), 14(NaCl), and 23(Al_2O_3) are shown in Tables 4.9 to 4.11 respectively.

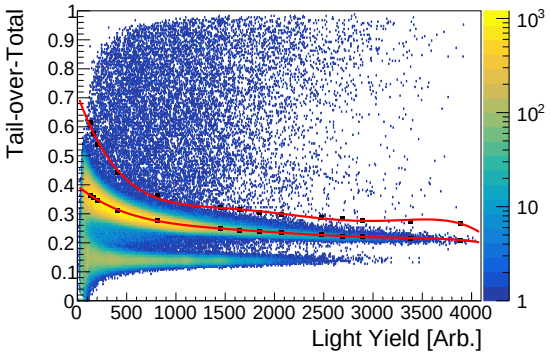

(a) PSD plot of the TC events. The upper red line is the fitted cut used for vetoing the false events above the neutron band. The lower red line is a fit to the means of the neutron band.

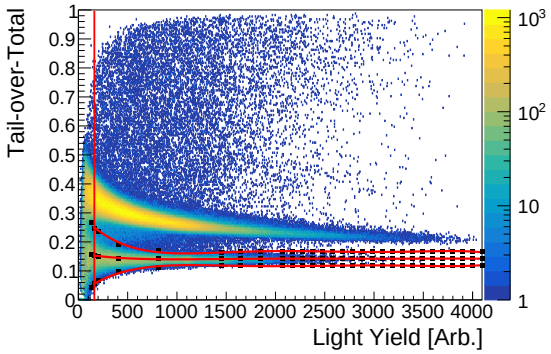

(b) PSD plot of the TC events. Upper red line is the fitted upper γ band cut. The lower red line is the fitted lower γ band cut. The middle red line is a fit for the mean values. The vertical red line is the lower energy cut-off for the γ cut.

Figure 4.11: PSD plots for the TC detector in the 14(^{56}Fe) dataset. The black dots are the values used to produce the red line fits. Only events that are included within TOF coincidences between a TC and SC within 100 nanoseconds are filled in the histogram.

The role of these cuts in determining the final flux characterization, is to remove as many invalid events as possible without removing true neutron events. Using 7σ to determine the upper neutron band cut ensures that the removed events are not true neutron events. This does mean that a small percentage of false events will remain, however, this value is expected to be small compared to the actual number of events. Tables 4.12 to 4.14 show the percentage of events above this cut is less than 1.1% for all TCs. The non-rejected pileup events are expected to have an effect of less than 1%. Notably, an additional background subtraction, described in Section 4.1.12, also will reduce the pileup background contribution in the final spectrum.

Similarly, 3σ was used for the lower and upper γ band cut because the narrow cut limits the likelihood of cutting neutron events while rejecting γ events. In addition to the fitted upper and lower cut, a lower LY threshold was set for each γ cut. This value was chosen at the point where the neutron and γ bands start to overlap. Two variations of the γ band cut are used in this analysis. For determining the timing calibration and timing resolution in Section 4.1.5, a cut on events within the upper and lower cuts is used. For all other analyses,

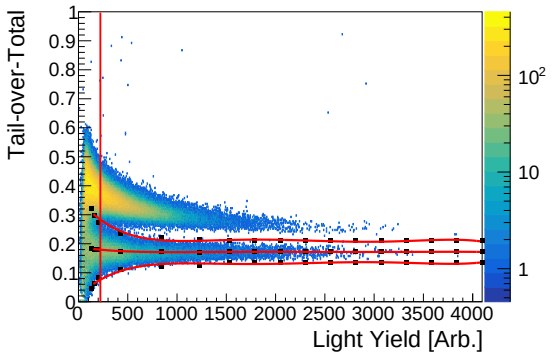

(a) PSD plot of the SC1 events.

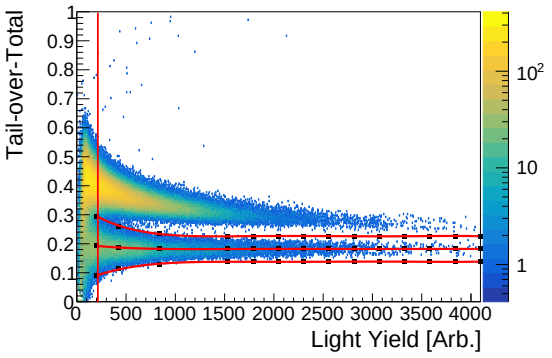

(b) PSD plot of the SC2 events.

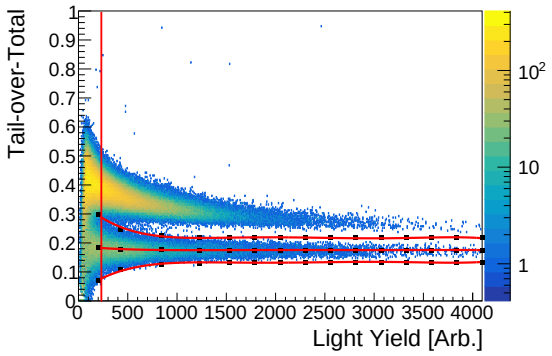

(c) PSD plot of the SC3 events.

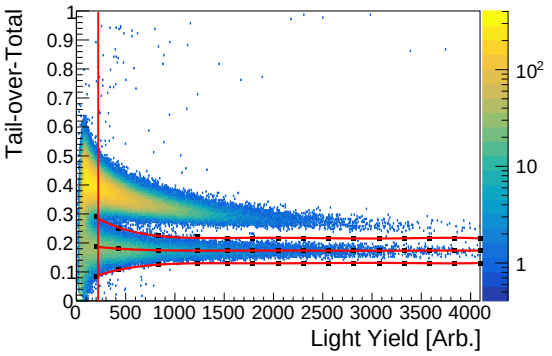

(d) PSD plot of the SC4 events.

Figure 4.12: PSD plots for each SC detector in dataset 14(^{56}Fe). The horizontal upper red line is the fitted upper γ band cut. The horizontal lower red line is the fitted lower γ band cut. The horizontal middle red line is a fit for the mean values. The vertical red line is the lower energy cut-off for the γ cut. The black dots are the values used to produce the red line fits. Only events that are included within TOF coincidences between a TC and SC within 100 nanoseconds are filled in the histogram.

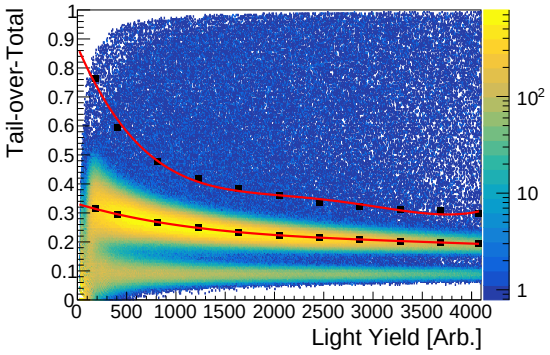

(a) PSD plot of the TC events. The upper red line is the fitted upper neutron band cut used for vetoing the false events above the neutron band. The lower red line is a fit to the means of the neutron band.

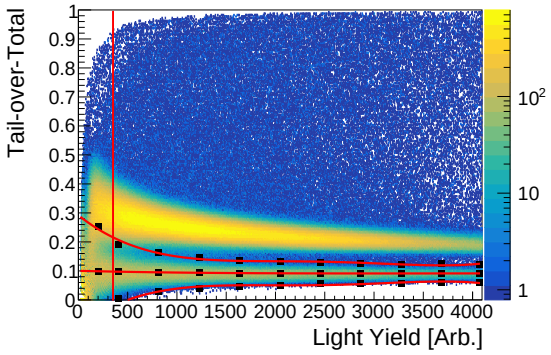

(b) PSD plot of the TC events. The upper red line is the fitted upper γ band cut. The lower red line is the fitted lower γ band cut. The middle red line is a fit for the mean values. The vertical red line is the lower energy cut-off for the γ cut.

Figure 4.13: PSD plots for the TC detector in dataset 14(NaCl). The red lines are the means and neutron and γ band cuts. The black dots are the values used to produce the red line fits. Only events that are included within TOF coincidences between a TC and SC within 100 nanoseconds are filled in the histogram.

Det.: PSD Cut	A_0	$A_1(\times 10^{-4})$	$A_2(\times 10^{-7})$	$A_3(\times 10^{-10})$	$A_4(\times 10^{-14})$	$A_5(\times 10^{-18})$
TC: Pileup	0.71	-9.63	9.64	-4.74	11.0	-9.71
TC: Upper γ	0.30	-3.74	3.76	-1.74	3.77	-3.08
TC: Lower γ	0.022	2.49	-2.46	1.14	-2.46	2.01
SC1: Upper γ	0.35	-4.00	4.13	-1.96	4.32	-3.58
SC1: Lower γ	0.022	3.07	-3.18	1.52	-3.37	2.81
SC2: Upper γ	0.33	-2.34	1.96	-0.790	1.53	-1.15
SC2: Lower γ	0.063	1.61	-1.33	0.530	-1.03	0.773
SC3: Upper γ	0.35	-3.43	3.29	-1.48	3.12	-2.50
SC3: Lower γ	0.027	2.71	-2.61	1.18	-2.49	2.01
SC4: Upper γ	0.34	-2.87	2.65	-1.16	2.41	-1.91
SC4: Lower γ	0.054	1.83	-1.68	0.736	-1.53	1.22

Table 4.9: Fitted parameters for the PSD cuts shown in Figs. 4.11 and 4.12 for the 14(^{56}Fe) dataset. The A parameter in the table represents the fitted parameters for the N^{th}-order polynomial expressed in Eq. (4.4). All parameters were found using the ROOT fitting routine with the Minit2 minimizer methods.

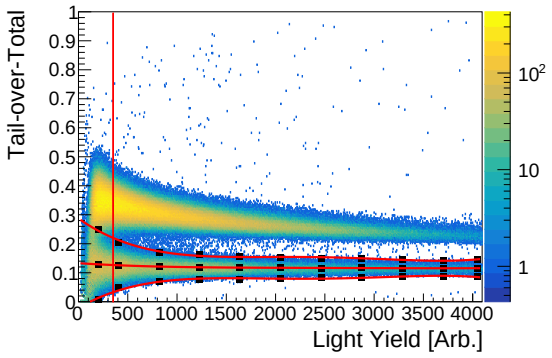

(a) PSD plot of the SC1 events.

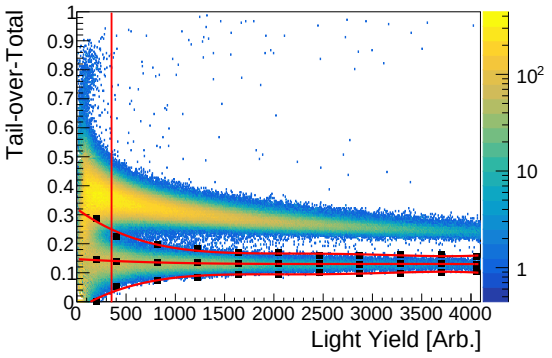

(b) PSD plot of the SC2 events.

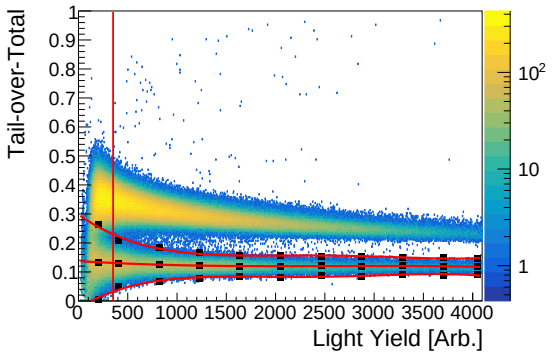

(c) PSD plot of the SC3 events.

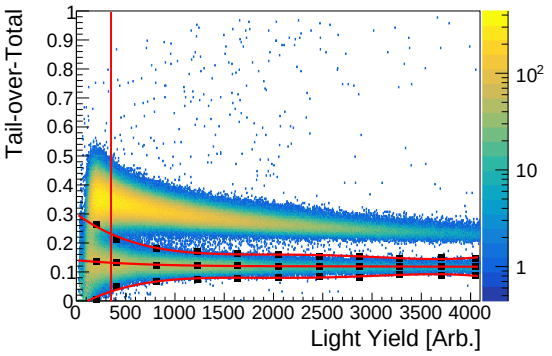

(d) PSD plot of the SC4 events.

Figure 4.14: PSD plots for each SC detector in dataset 14(NaCl). The horizontal upper red line is the fitted upper γ band cut. The horizontal lower red line is the fitted lower γ band cut. The horizontal middle red line is a fit for the mean values. The vertical red line is the lower energy cut-off for the γ cut. The black dots are the values used to produce the red line fits. Only events that are included within TOF coincidences between a TC and SC within 100 nanoseconds are filled in the histogram.

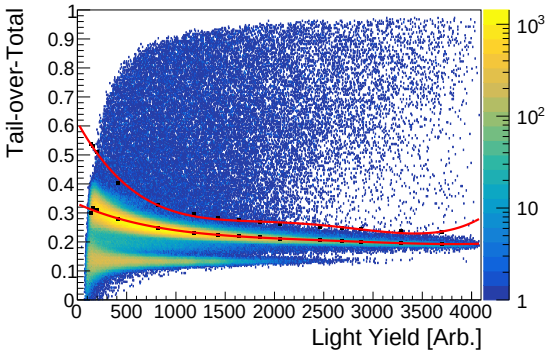

(a) PSD plot of the TC events. The upper red line is the fitted upper neutron band cut used for vetoing the false events above the neutron band. The lower red line is a fit to the means of the neutron band.

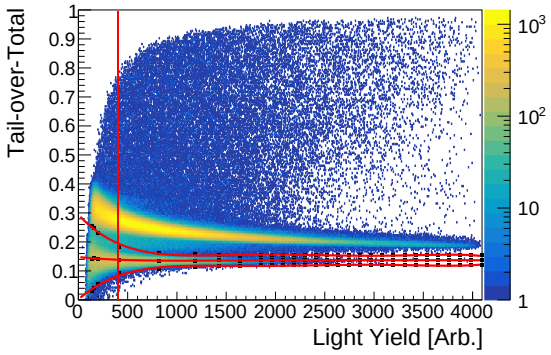

(b) PSD plot of the TC events. The upper red line is the fitted upper γ band cut. The lower red line is the fitted lower γ band cut. The middle red line is a fit for the mean values. The vertical red line is the lower energy cut-off for the γ cut.

Figure 4.15: PSD plots for the TC detector in dataset 23(Al_2O_3). The red lines are the means and neutron and γ band cuts. The black dots are the values used to produce the red line fits. Only events that are included within TOF coincidences between a TC and SC within 100 nanoseconds are filled in the histogram.

Det.: PSD Cut	A_0	$A_1(\times 10^{-4})$	$A_2(\times 10^{-7})$	$A_3(\times 10^{-11})$	$A_4(\times 10^{-15})$
TC: Pileup	0.708	-6.12	3.67	-9.95	9.76
TC: Upper γ	0.236	-2.08	1.38	-3.88	3.88
TC: Lower γ	-0.0295	1.78	-1.22	3.56	-3.65
SC1: Upper γ	0.287	-2.46	1.66	-4.73	4.77
SC1: Lower γ	-0.0177	1.89	-1.31	3.79	-3.86
SC2: Upper γ	0.321	-2.56	1.58	-4.21	4.04
SC2: Lower γ	-0.0260	2.12	-1.37	3.77	-3.71
SC3: Upper γ	0.300	-2.53	1.61	-4.36	4.18
SC3: Lower γ	-0.0243	2.06	-1.40	4.01	-4.04
SC4: Upper γ	0.303	-2.61	1.75	-5.01	5.07
SC4: Lower γ	-0.0175	1.86	-1.29	3.77	-3.88

Table 4.10: Fitted parameters for the PSD cuts shown in Figs. 4.13 and 4.14 for the 14(NaCl) dataset. The A parameter in the table represents the fitted parameters for the N^{th}-order polynomial expressed in Eq. (4.4). All parameters were found using the ROOT fitting routine with the Minit2 minimizer.

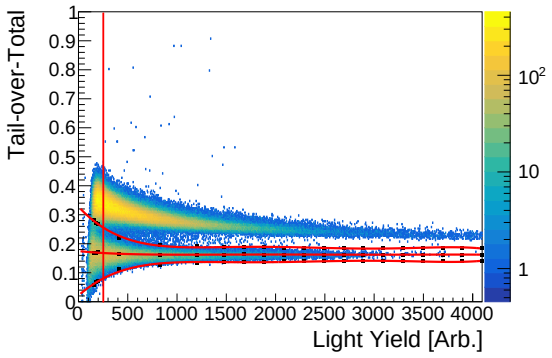

(a) PSD plot of the SC1 events.

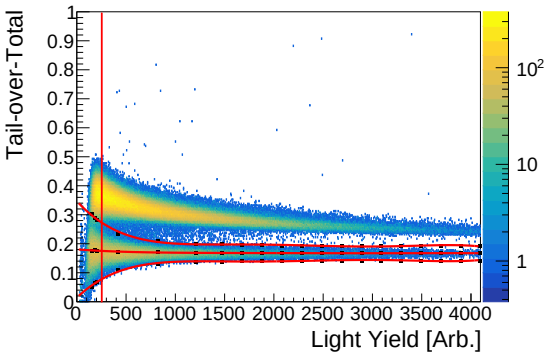

(b) PSD plot of the SC2 events.

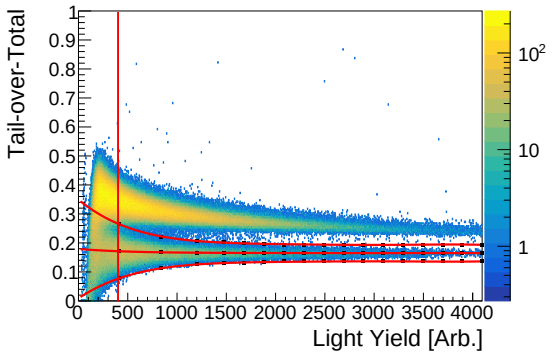

(c) PSD plot of the SC3 events.

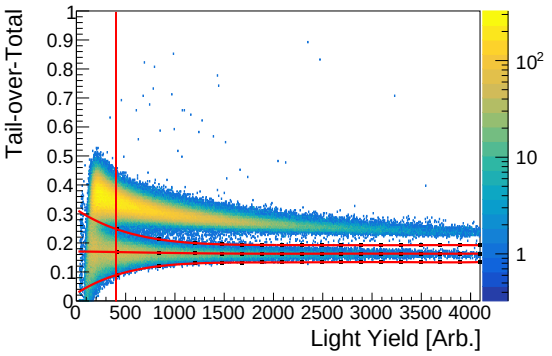

(d) PSD plot of the SC4 events.

Figure 4.16: PSD plots for each SC detector in dataset 23(Al_2O_3). The horizontal upper red line is the fitted upper γ band cut. The horizontal lower red line is the fitted lower γ band cut. The horizontal middle red line is a fit for the mean values. The vertical red line is the lower energy cut-off for the γ cut. The black dots are the values used to produce the red line fits. Only events that are included within TOF coincidences between a TC and SC within 100 nanoseconds are filled in the histogram.

Det.: PSD Cut	A_0	$A_1(\times 10^{-4})$	$A_2(\times 10^{-7})$	$A_3(\times 10^{-10})$	$A_4(\times 10^{-14})$	$A_5(\times 10^{-18})$
TC: Pileup	0.62	-6.33	4.34	-1.30	1.40	-
TC: Upper γ	0.29	-3.62	3.56	-1.65	3.60	-2.97
TC: Lower γ	0.0026	2.93	-2.84	1.29	-2.78	2.27
SC1: Upper γ	0.33	-3.69	3.64	-1.69	3.65	-2.99
SC1: Lower γ	0.021	3.02	-2.96	1.37	-2.97	2.43
SC2: Upper γ	0.35	-3.79	3.66	-1.68	3.63	-2.97
SC2: Lower γ	0.014	3.23	-3.17	1.46	-3.17	2.60
SC3: Upper γ	0.35	-2.81	2.12	-0.818	1.57	-1.18
SC3: Lower γ	0.0084	2.29	-1.71	0.647	-1.22	0.907
SC4: Upper γ	0.32	-2.26	1.65	-0.595	1.06	-0.747
SC4: Lower γ	0.026	2.17	-1.74	0.683	-1.31	0.975

Table 4.11: Fitted parameters for the PSD cuts shown in Figs. 4.15 and 4.16 for the 23(Al_2O_3) dataset. The A parameter in the table represents the fitted parameters for the N^{th}-order polynomial expressed in Eq. (4.4).

Det.	PSD Cut	Rejected	Total	Percent [%]
TC	Pileup	11347	2323719	0.488
TC	γ	67819	2323719	2.92
SC1	γ	13297	514213	2.59
SC2	γ	19395	619132	3.13
SC3	γ	17688	607512	2.91
SC4	γ	17445	583038	2.99

Table 4.12: Total number of rejected single events for each detector in the 14(^{56}Fe) dataset

Det.	PSD Cut	Rejected	Total	Percent [%]
TC	Pileup	65545	6005196	1.09
TC	γ	205497	6005196	3.42
SC1	γ	50598	1375091	3.68
SC2	γ	50331	1781705	2.83
SC3	γ	53417	1451009	3.68
SC4	γ	51160	1298069	3.94

Table 4.13: Total number of rejected single events for each detector in the 14(NaCl) dataset

Det.	PSD Cut	Events in Cut	Total Events	Percent [%]
TC	Pileup	29814	3053145	0.977
TC	γ	72143	3053145	2.36
SC1	γ	16915	646173	2.62
SC2	γ	23305	806834	2.89
SC3	γ	16314	815811	2.00
SC4	γ	15626	784558	1.99

Table 4.14: Total number of rejected single events for each detector in the 23(Al_2O_3) dataset

all events below the upper γ band cut and above the LY cut were rejected. For the timing calibration and resolution determination, it is important to restrict events to only γ events. For other parts of the analysis, all events above the upper neutron cut and all events below the upper γ cut are excluded to reduce background.

4.1.5 Timing Calibration and Timing Resolution

The timestamps recorded for each detector in the STOF array need to be time-corrected to ensure the time-of-flight values are accurate. Timing offsets arise primarily due to differences in the amount of time it takes a signal from the detector to travel to the digitizer. The primary cause of the time difference can be attributed to variations in cable length impedance and PMT response time. To achieve a proper timing calibration between the TC events and the SC events, γ-rays incident on the target cell that are scattered and detected in the scatter cells are used. First, the γ-ray PSD events cut determined in Section 4.1.4 is implemented to limit the events to only γ-ray events. Then the difference in recorded timestamps between a TC and every detected SC event within a 100 nanosecond window is found and plotted for each scatter cell, see Figs. 4.17 to 4.19.

Table 4.15 contains the mean and σ of a fitted Gaussian for each histogram.

The expected time-of-flight of a γ-ray between each scatter cell, TOF_e, is calculated by the following equation,

$$TOF_e = \frac{D}{c}, \tag{4.5}$$

where D is the mean neutron travel distance between the TC and the SC (see Tables 4.1 to 4.3 for tabulated distances), and c is the speed of light. Table 4.16 lists the average time it will take a photon to travel between the target cell and each scatter cell for all datasets.

Subtracting the observed mean from Table 4.15 of the TOF histograms from the corresponding photon travel time in Table 4.16, the timing correction factor is found, see Table 4.16.

The timing correction in Table 4.16 is applied to all subsequent analyses that use the measured time-of-flight coincidences.

Det.	Dataset	Mean [ns]	σ [ns]
SC1	14(^{56}Fe)	2.540	0.1969
SC2	14(^{56}Fe)	5.101	0.2146
SC3	14(^{56}Fe)	3.068	0.2056
SC4	14(^{56}Fe)	2.970	0.2150
SC1	14(NaCl)	2.449	0.2361
SC2	14(NaCl)	5.305	0.2389
SC3	14(NaCl)	3.254	0.2312
SC4	14(NaCl)	3.152	0.2389
SC1	23(Al_2O_3)	4.304	0.1834
SC2	23(Al_2O_3)	3.278	0.1964
SC3	23(Al_2O_3)	3.113	0.1850
SC4	23(Al_2O_3)	3.023	0.1865

Table 4.15: Mean and σ of the γ TOF histograms, Figs. 4.17 to 4.19. The mean values are used for timing calibration, and the σ is the timing resolution.

Det.	Dataset	Photon Travel Time [ns]	Timing Correction [ns]
SC1	14(^{56}Fe)	1.374	-1.165
SC2	14(^{56}Fe)	1.335	-3.767
SC3	14(^{56}Fe)	1.344	-1.725
SC4	14(^{56}Fe)	1.382	-1.588
SC1	14(NaCl)	1.480	-0.9683
SC2	14(NaCl)	1.449	-3.856
SC3	14(NaCl)	1.461	-1.794
SC4	14(NaCl)	1.492	-1.660
SC1	23(Al_2O_3)	1.571	-2.734
SC2	23(Al_2O_3)	1.535	-1.743
SC3	23(Al_2O_3)	1.562	-1.551
SC4	23(Al_2O_3)	1.600	-1.423

Table 4.16: The photon travel time is the expected average TOF for a photon between the TC and each SC. The timing correction is the difference between the observed γ TOF, Table 4.15 and the expected γ TOF.

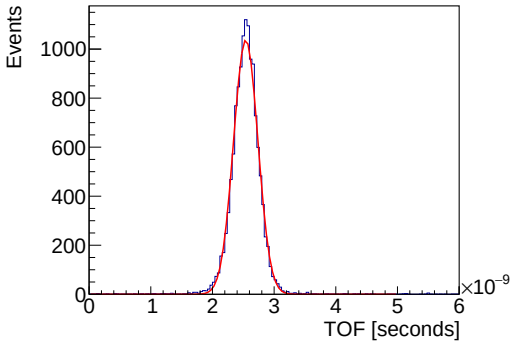

(a) TOF events between TC and SC1. $\chi^2_\nu = 2.64$.

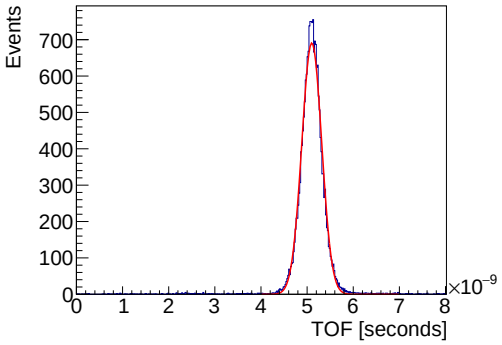

(b) TOF events between TC and SC2. $\chi^2_\nu = 2.90$.

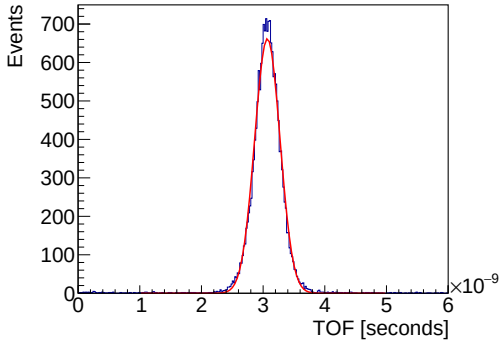

(c) TOF events between TC and SC3. $\chi^2_\nu = 2.26$.

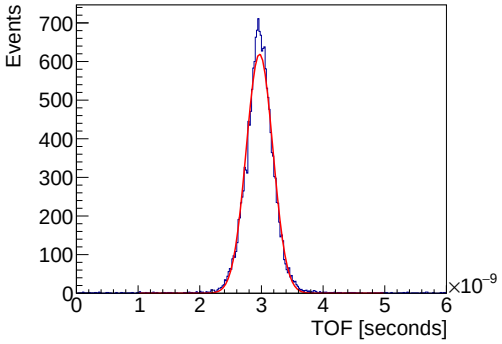

(d) TOF events between TC and SC4. $\chi^2_\nu = 2.44$.

Figure 4.17: TOF plots for γ events determined by a PSD cut from Section 4.1.4 for dataset 14(^{56}Fe). The red lines are a Gaussian fit to the histogram. χ^2_ν is the reduced Chi-squared of the fit.

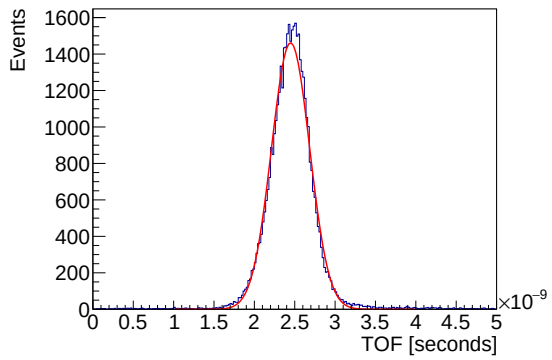

(a) TOF events between TC and SC1. $\chi^2_\nu = 6.84$.

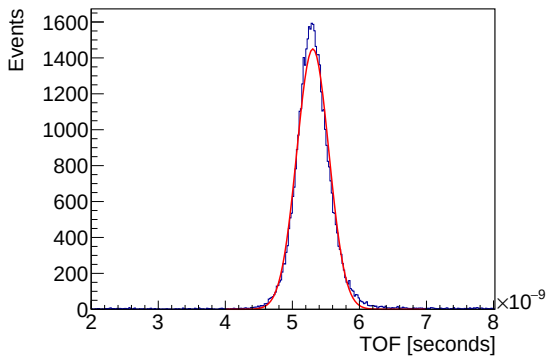

(b) TOF events between TC and SC2. $\chi^2_\nu = 7.71$.

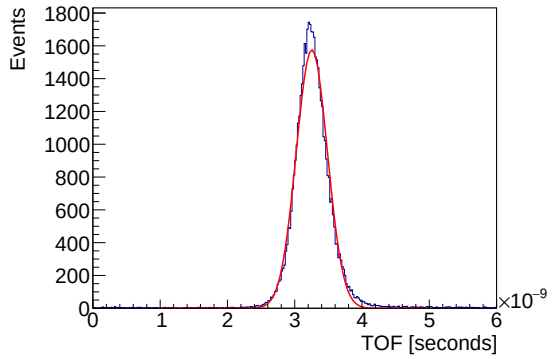

(c) TOF events between TC and SC3. $\chi^2_\nu = 7.58$.

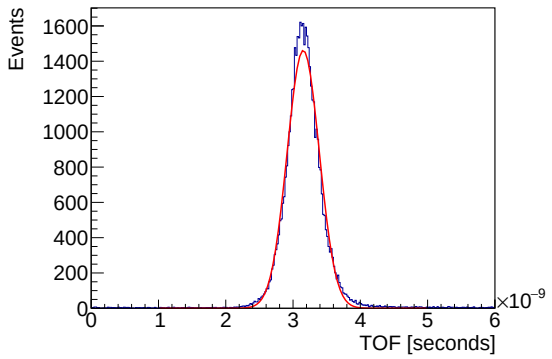

(d) TOF events between TC and SC4. $\chi^2_\nu = 7.21$.

Figure 4.18: TOF plots for γ events determined by a PSD cut from Section 4.1.4 for dataset 14(NaCl). The red lines are a Gaussian fit to the histogram. χ^2_ν is the reduced chi-squared for the fit.

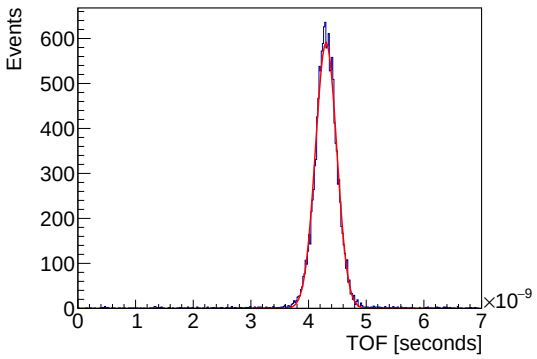

(a) TOF events between TC and SC1. $\chi^2_\nu = 2.18$.

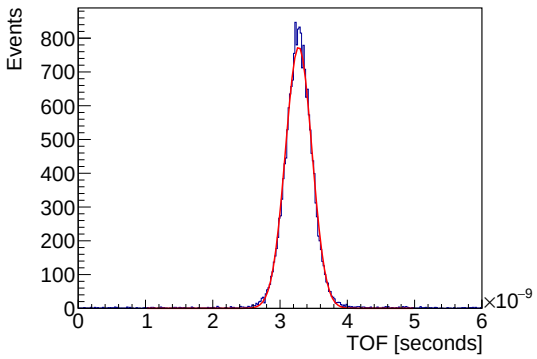

(b) TOF events between TC and SC2. $\chi^2_\nu = 2.41$.

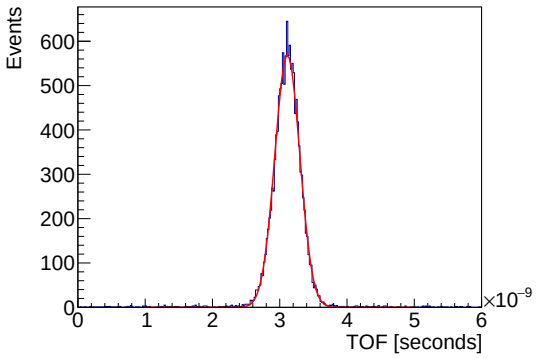

(c) TOF events between TC and SC3. $\chi^2_\nu = 1.77$.

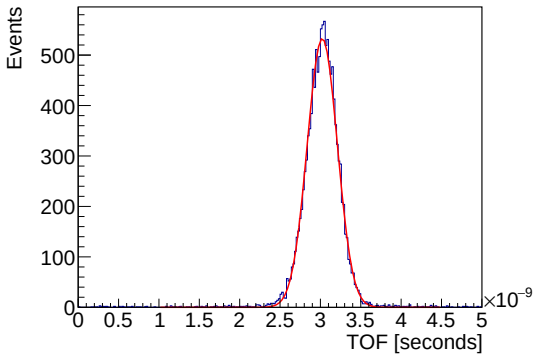

(d) TOF events between TC and SC4. $\chi^2_\nu = 1.97$.

Figure 4.19: TOF plots for γ events determined by a PSD cut from Fig. 4.19 for dataset 23(Al_2O_3). The red lines are a Gaussian fit to the histogram.

4.1.6 Light Yield Cuts

4.1.6.1 Lower and Upper Light Yield Cuts

The discriminator settings, as described in Section 3.3, for the datasets implemented a CFD cut at low light yield to minimize triggering on noise. Consequently, there is a PSD-dependent light yield where events were rejected by the discriminator. This rejection is observable in the PSD plots shown in figures Figs. 4.11 to 4.16. The discriminator LY rejection is higher for neutrons than for γ rays. This shape parameter is not replicated within the simulations. Therefore, a flat lower light yield cut is implemented for all detectors based on where the events begin to fall off in the neutron band in the PSD plots. The lower light yield cuts used in all datasets are tabulated in Table 4.17.

Det.	Dataset	LY [Arb.]
TC	14(^{56}Fe)	100
SC1	14(^{56}Fe)	100
SC2	14(^{56}Fe)	100
SC3	14(^{56}Fe)	100
SC4	14(^{56}Fe)	100
TC	14(NaCl)	200
SC1	14(NaCl)	200
SC2	14(NaCl)	100
SC3	14(NaCl)	200
SC4	14(NaCl)	200
TC	23(Al_2O_3)	200
SC1	23(Al_2O_3)	200
SC2	23(Al_2O_3)	200
SC3	23(Al_2O_3)	200
SC4	23(Al_2O_3)	200

Table 4.17: Lower LY cut used for each detector event for each dataset.

Implementation of an upper light yield cut was considered, but not implemented. Histograms of the incoming neutron energy versus TC light yield are plotted in Fig. 4.20. The incoming neutron energy was calculated based on the measured TOF using the methodology discussed in Section 2.1.1.1. For datasets 14(^{56}Fe) and 23(Al_2O_3), Figs. 4.20a and 4.20c show that all the anticipated measured events (14 MeV and 23 MeV respectively), fall well within the maximum recorded light yield value of 4096. Therefore, an upper light yield cut was not implemented. For dataset 14(NaCl), Fig. 4.20b shows the events saturating into the maximum light yield value of 4096. However, as detailed in Section 4.1.2, this is not due to input-saturation clipping but to gate-saturation. Placing an upper light yield cut at 4096 to exclude these events will remove most information about the neutron spectrum above

about 10 MeV. Rather than losing information above 10 MeV, no upper light yield cut was applied. This will result in a spectrum with an increased background, as fewer high-energy background events can be identified.

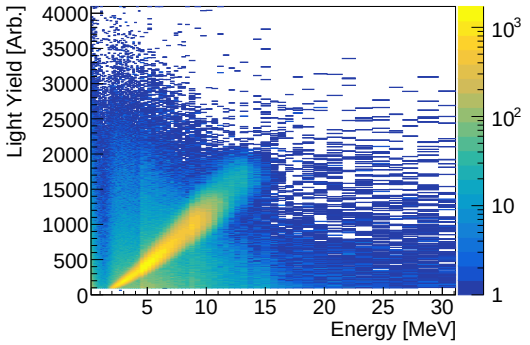

(a) Dataset 14(^{56}Fe).

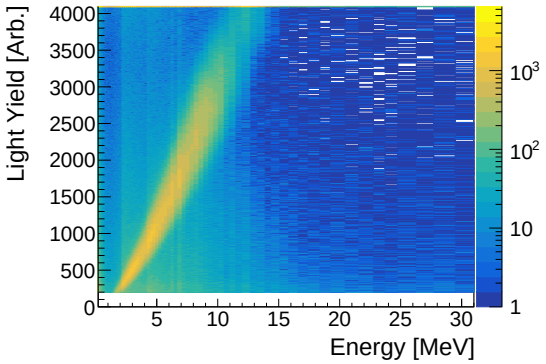

(b) Dataset 14(NaCl).

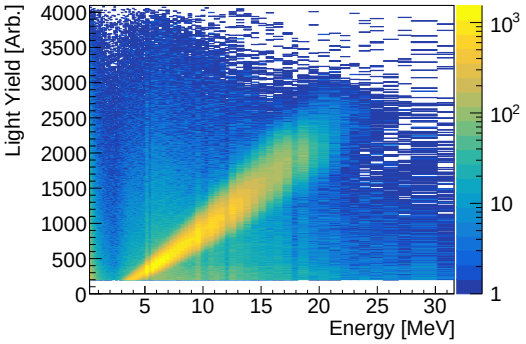

(c) Dataset 23(Al_2O_3).

Figure 4.20: Measured LY's versus TOF-determined incoming neutron energy, excluding PSD-rejected pile-up and *gamma* events.

4.1.6.2 Proton Energy Vs Light Yield Rejection

Rejection of additional background events is implemented through a proton energy versus light yield cut. A 2D histogram of the estimated proton recoil energy, as determined by the measured outgoing TOF, in the target cell versus the measured light yield in the target cell is tallied. Events determined by PSD to be pileup or γ events, as outlined in Section 4.1.4, are excluded. Additionally, the LY cuts from Section 4.1.6.1 is also implemented. The proton energy is estimated from every measured coincidence within one cyclotron pulse time window, using Eq. (2.3). The proton light yield has a quantifiable relationship to the recoiling proton energy. Events outside of this are background, primarily due to electronic

noise, random coincidences, and pileup. Projections of small slices, representing proton energies, were taken along the entire length of the spectrum. For each proton energy, a combined Gaussian and linear model was fit to the light yield distribution. Examples from SC1 of dataset 14(^{56}Fe) are shown in Fig. 4.21. The red lines are the fits and the black histograms are the data. The red lines represent rejection thresholds defined at $\pm 5\sigma$ of the means. 5σ was chosen to minimize inclusion of real events in this rejection cut. Each of the sets of points are then fitted to a 2^{nd} degree polynomial fit of the form,

$$Y_{LY} = \Sigma_{i=0}^{2} A_i * E_p^i, \tag{4.6}$$

where Y_{LY} is the measured LY in the TC, E_p is the estimated proton recoil energy, and A_i are the fitted parameters. The fitted cuts are shown in Figs. 4.22 to 4.23 and the fitted parameters are in Tables 4.18 and 4.19.

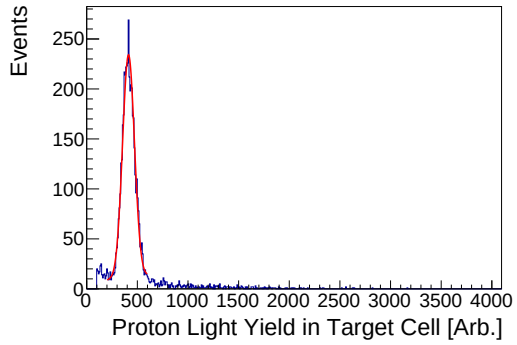

(a) SC1 at proton energy 2.5 MeV.

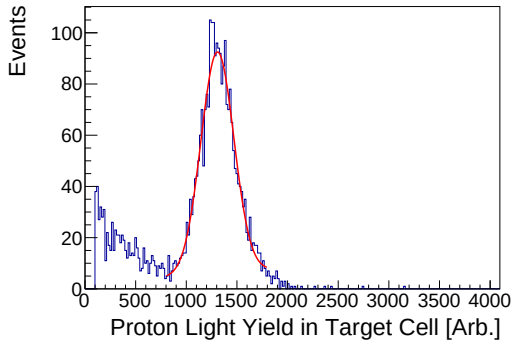

(b) SC1 at proton energy 5.9 MeV.

Figure 4.21: Proton energy slices of the proton energy versus LY histogram for SC1 from dataset 14(^{56}Fe), see Fig. 4.22a. The red line is the result of a fit of the spectra to a combined Gaussian and linear function.

Gate-saturated events are excluded from this cut. For dataset 14(NaCl), this will result in a spectrum with higher uncertainty due to an increased background, as fewer background events are rejected.

Det.	Dataset	A_0	A_1	A_2
SC1	14(^{56}Fe)	-170.8	361.9	6.210
SC2	14(^{56}Fe)	-226.4	406.9	-3.758
SC3	14(^{56}Fe)	-163.4	338.3	12.05
SC4	14(^{56}Fe)	-116.5	309.2	8.693
SC1	14(NaCl)	-538.2	1191	2.689
SC2	14(NaCl)	-386.0	970.0	39.55
SC3	14(NaCl)	-394.6	940.9	38.69
SC4	14(NaCl)	-373.2	934.7	38.19
SC1	23(Al_2O_3)	-222.3	367.3	17.15
SC2	23(Al_2O_3)	-153.1	350.5	22.67
SC3	23(Al_2O_3)	-164.3	353.5	20.55
SC4	23(Al_2O_3)	-154.8	345.8	21.60

Table 4.18: Quadratic fit parameters to Eq. (4.6) of the upper proton energy vs LY cut for each detector for each dataset, corresponding to the lower red line in Figs. 4.22 to 4.24.

Det.	Dataset	A_0	A_1	A_2
SC1	14(^{56}Fe)	-63.84	101.5	8.699
SC2	14(^{56}Fe)	-31.63	68.57	14.50
SC3	14(^{56}Fe)	-59.27	112.9	6.438
SC4	14(^{56}Fe)	-283.7	169.2	0.9081
SC1	14(NaCl)	-54.96	179.8	59.56
SC2	14(NaCl)	-88.38	224.4	46.51
SC3	14(NaCl)	-30.45	156.6	56.00
SC4	14(NaCl)	-33.61	150.7	59.85
SC1	23(Al_2O_3)	-143.1	136.8	4.251
SC2	23(Al_2O_3)	-138.3	142.7	6.564
SC3	23(Al_2O_3)	-174.8	155.8	3.322
SC4	23(Al_2O_3)	-179.9	159.9	2.642

Table 4.19: Quadratic fit parameters to Eq. (4.6) of the lower proton energy vs LY cut for each detector for each dataset, corresponding to the lower red line in Figs. 4.22 to 4.24.

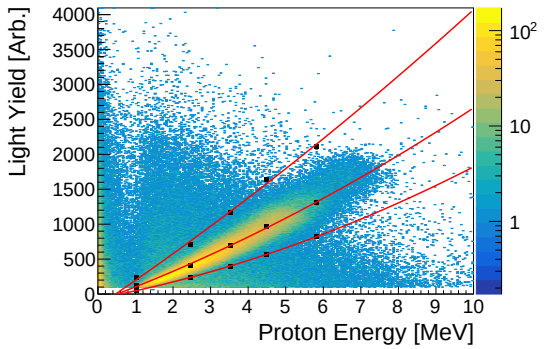

(a) SC1.

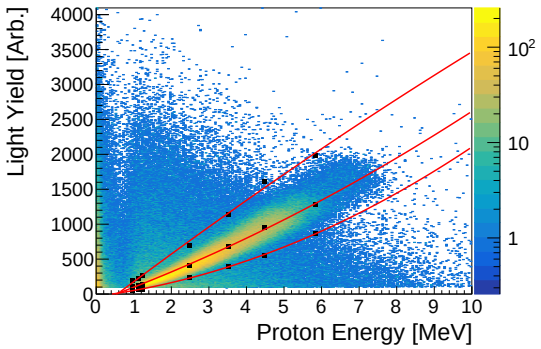

(b) SC2.

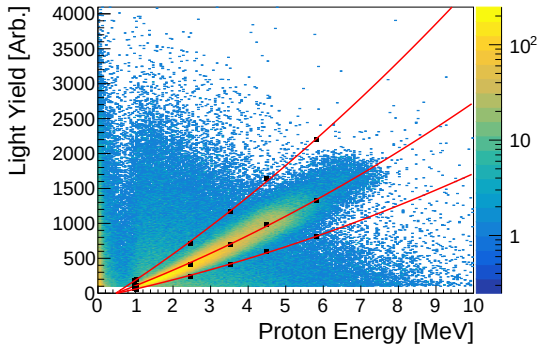

(c) SC3.

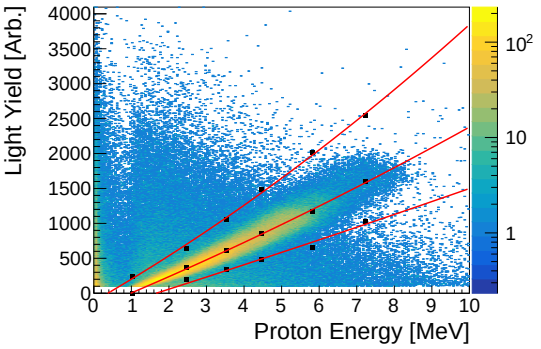

(d) SC4.

Figure 4.22: The proton recoil energy in the TC versus the measured LY in the TC, for each detector in dataset 14(^{56}Fe), excluding pileup and γ events as determined by PSD from Section 4.1.4. The middle red line is a fit to the mean of the event band (black center points); the top and bottom red lines are fits to the mean $\pm$ 5σ black top and bottom points).

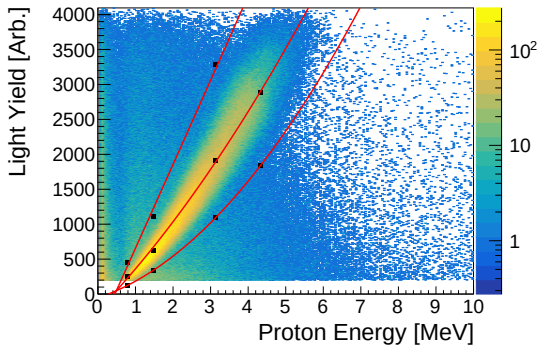

(a) SC1.

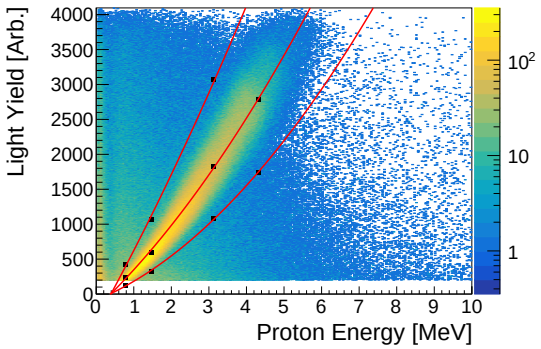

(b) SC2.

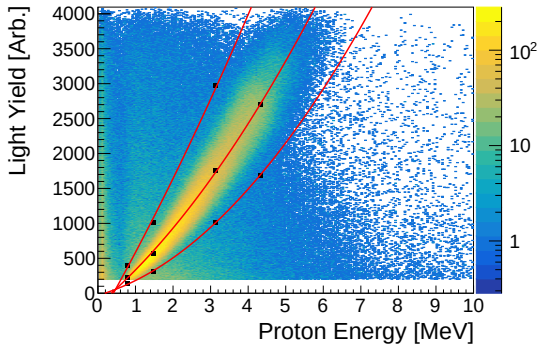

(c) SC3.

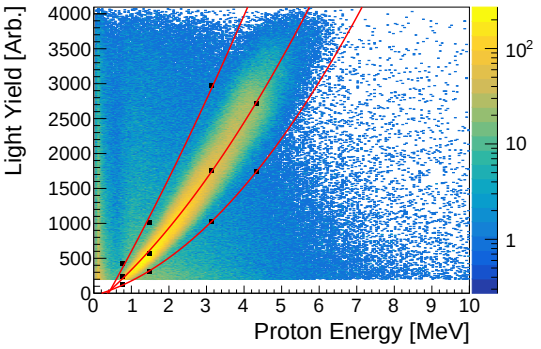

(d) SC4.

Figure 4.23: The proton recoil energy in the TC versus the measured LY in the TC, for each detector in dataset 14(NaCl), excluding pileup and γ events as determined by PSD from Section 4.1.4. The middle red line is a fit to the mean of the event band (black center points); the top and bottom red lines are fits to the mean $\pm 5\sigma$ black top and bottom points).

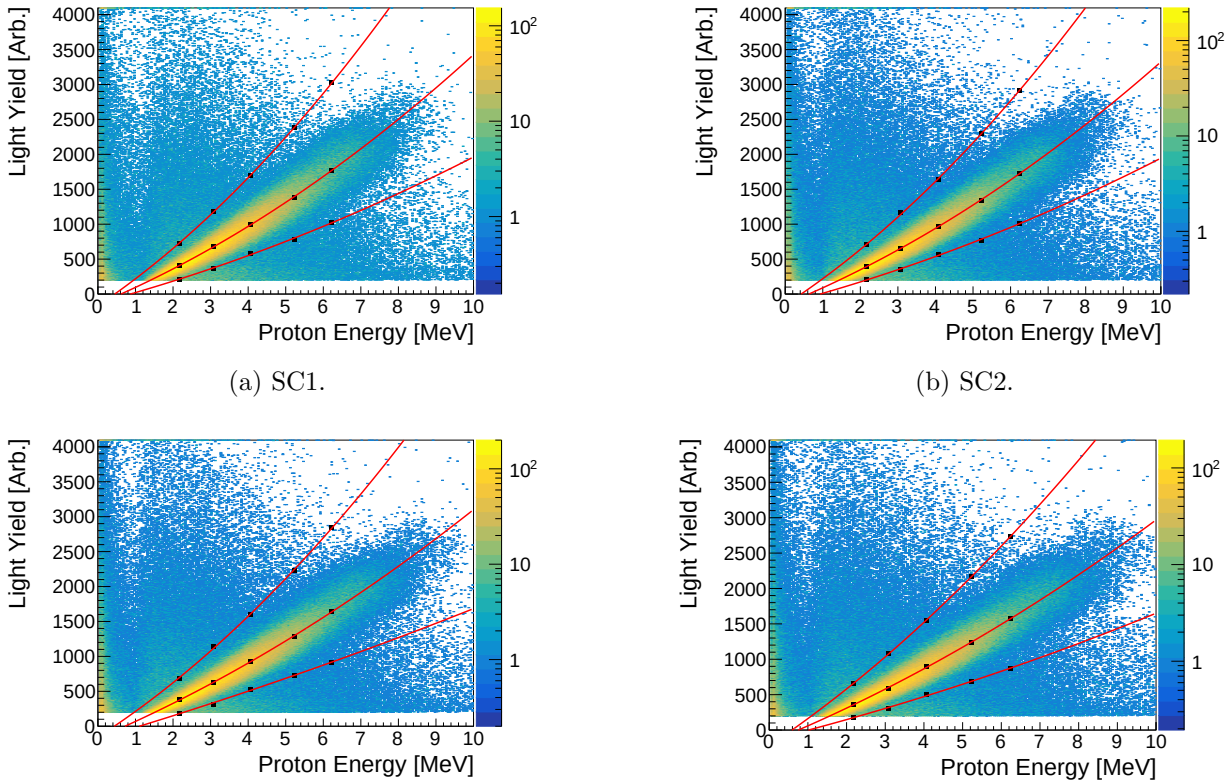

(a) SC1.

(b) SC2.

(c) SC3.

(d) SC4.

Figure 4.24: The proton recoil energy in the TC versus the measured LY in the TC, for each detector in dataset 23(Al_2O_3), excluding pileup and γ events as determined by PSD from Section 4.1.4. The middle red line is a fit to the mean of the event band (black center points); the top and bottom red lines are fits to the mean $\pm$ 5σ black top and bottom points).

4.1.7 Energy Resolution and Bin Selection

An energy histogram binning was chosen based on the resolution of the spectrometer determined via a Geant4 simulation.

Valid coincidences are events where neutrons deposit energy though elastic recoils with the hydrogen in the target cell, and then deposit energy by reactions with either hydrogen or carbon of only one of the scattered cells. Coincidences where the neutron interacted with a carbon nucleus within the target cell scintillator are excluded. Additionally, coincidences that had scattered within multiple scatter cells or multiple times within the target cell are excluded. Coincidences where the neutron interacted outside the scintillating material were also excluded. The simulated time-of-flight coincidences are also smeared based on a Gaussian random number generator with a sigma based on the experimentally-determined timing resolution from Table 4.15.

The known initial energy of the simulated neutron versus the time-of-flight determined energy is plotted in Fig. 4.25. These plots represent the energy resolution for a given neutron energy of the STOF spectrometer for single scattered neutron events. A C++ function was developed to determine the energy-binning structure from this plot automatically. The function starts at a user-defined energy and produces a 1D histogram slice. The standard deviation, σ, and mean, μ, of the histogram is found. Then the following value is calculated,

$$BE = \mu + \frac{\sigma}{4}, \tag{4.7}$$

where BE is the upper bin edge for the first energy bin. The program then iterates through the bins on the x-axis in Fig. 4.25, producing a new x-slice and determining a new mean, μ_{new}, and standard deviation, σ_{new}, until it finds the first bin where the following is true,

$$BE - \mu_{new} + \frac{\sigma_{new}}{4} < 0. \tag{4.8}$$

Once this condition is met, the next bin edge is calculated using the same method. This process is repeated up until the end of the spectrum. The bin structure used for the differential flux in this work is, therefore, representative of one-quarter of the energy resolution of the STOF spectrometer for that given energy.

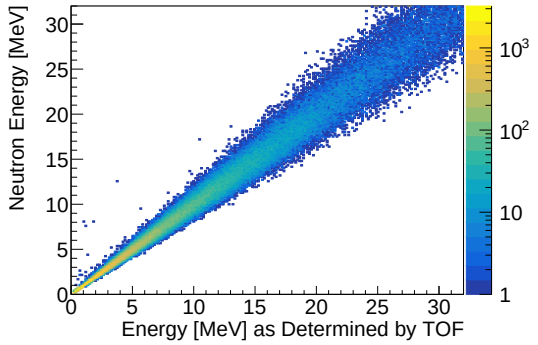

(a) Dataset 14(^{56}Fe).

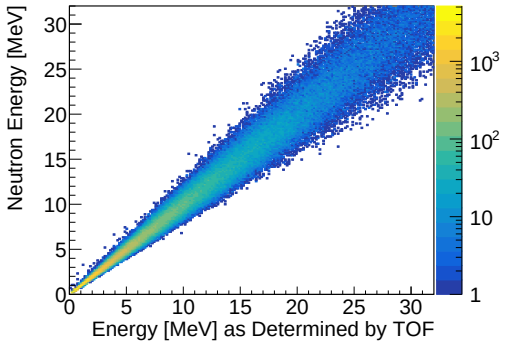

(b) Dataset 14(NaCl).

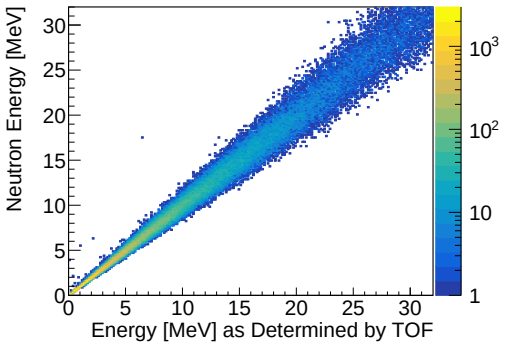

(c) Dataset 23(Al_2O_3).

Figure 4.25: Simulated neutron energy versus the energy calculated from the time-of-flight between detectors.

4.1.8 Dead Time

The terms used in this section are defined in Chapter 3. Three potential contributions to dead time, periods in which detectors were unable to collect or record data, were evaluated. The first consideration is due to a memory full condition in the digitizer. Signals received by the digitizer are stored within a memory buffer before it is sent to the computer for processing with CoMPASS. This transfer takes time, so with high event rates, the memory buffer may fill up before it can offload recorded signals to the computer. The CAEN digitizer is configured through the firmware to flag events if a memory full condition occurs. By processing the flag value associated with each event, such time periods can be determined. For all measured data sets in this work, no memory buffer full conditions occurred.

A second contribution is the amount of time due to trigger hold-off as described in Section 3.3. A trigger hold-off was set that was slightly longer than the long gate. Therefore, there is a small time period between the end of the long gate and the end of the trigger hold-

off where the detector does not accept pulses and is considered dead, t_{dead}. This contribution to dead time is dependent on the total number of events recorded by each detector. This dead time contribution is estimated by taking the total number of target cell events and multiplying by t_{dead}.

Third, any events that are determined to be pile-up (see Tables 4.4 to 4.6 and 4.12 to 4.14), or input-saturated events (see Tables 4.4 to 4.6) result in additional dead time. This dead time is estimated by taking the total number of all these events and multiplying it by the total trigger hold-off time.

The dead time contribution due to individual detectors is proportional to the total number of events. The events in all four scatter cells are 2–3 orders of magnitude less than the in-beam target cell, Tables 4.4 to 4.6. Contributions to dead time due to the scatter cells are <1% of that of the target cell. Therefore, the dead time contributions solely from the target cell are considered. The total estimated dead time for each dataset is shown in Table 4.20.

Dataset	Dead time [s]	Livetime [s]
14(^{56}Fe)	22.3	394085.8
14(NaCl)	58.4	316881.7
23(Al_2O_3)	22.2	399678.8

Table 4.20: Calculated dead time. The livetime, the realtime (Table 3.8) minus the dead time, is also tabulated.

4.1.9 Calibration of Scintillator Light

An existing light yield calibration framework was used to perform a light yield calibration. The framework was initially developed in [7]. This method is used to estimate the relationship between the electron-light equivalent of proton energy deposition (MeVee) and the measured proton light yields. The relationship is fitted to the following linear functional form

$$L = b + a * x, \tag{4.9}$$

where L is the light yield in MeVee, a and b are the fit parameters, and x is the measured proton light yield. The best fit to a and b are found by minimizing to the best fit of the light yield resolution function,

$$\frac{\Delta L}{L} = (E_c^2 * \frac{E_1^2}{L} * \frac{E_2^2}{L^2})^{1/2}. \tag{4.10}$$

$\frac{\Delta L}{L}$ is the light yield resolution. E_c, E_1, and E_2 represents the light yield variation due to photon losses from the interaction location in the scintillator, light conversion/amplification, and electronic noise respectively. This relation comes from [43]. The calibration points used for the minimization are taken from multiple scattered time-of-flight slices as a function of

measured light yield. The time-of-flight versus light-yield plots for dataset 14(^{56}Fe) for each target-scatter cell pair are shown in Fig. 4.26. The plots include all coincidences between the target cell and the scatter cell within a 100 ns time window. Three projections, shown in the same figures as red boxes, along the x-axis were taken. For all dataset results, see Appendix C.

The MeVee light yield as a function of neutron time of flight was simulated using the Geant4 model from Section 4.1.7. The MeVee values are estimated by taking the proton energy deposited in a given detector and comparing it to previously measured and fitted light yield data [44]. This paper's measured light yield values are fitted to Eq. (2.5) as described in Section 2.1.3. These plots are shown in Fig. 4.27 for the 14(^{56}Fe) dataset. For comparison with the raw measured data, no coincidences are excluded as background. Light yield curves for the same time-of-flight slices in Figs. 4.26 and 4.27 were used as inputs into a C++ function, which convolves the measured LY with the simulated detector response function. This class applies the proton energy-to-LY relation of Eq. (4.9) and iterates over E_c, E_1, and E_2 parameters from Eq. (4.10) to determine the best fit to the measurements. All results from each dataset are in Appendix C.

These calibrations are used to reproduce the LY based cuts used on the measured data, as described in see Sections 4.1.6.1 and 4.1.6.2, within the Geant4 simulation.

Dataset	Det. ID	a	b
14(^{56}Fe)	TC	0.00226	0.0231
14(^{56}Fe)	SC1	0.00202	0.0704
14(^{56}Fe)	SC2	0.00164	0.0706
14(^{56}Fe)	SC3	0.00155	0.0731
14(^{56}Fe)	SC4	0.00153	0.0313
14(NaCl)	TC	0.000670	0.00674
14(NaCl)	SC1	0.000749	0.00178
14(NaCl)	SC2	0.000741	0.00872
14(NaCl)	SC3	0.000740	0.000927
14(NaCl)	SC4	0.000753	0.00309
23(Al_2O_3)	TC	0.00207	0.106
23(Al_2O_3)	SC1	0.00276	0.0188
23(Al_2O_3)	SC2	0.00217	0.0266
23(Al_2O_3)	SC3	0.00211	0.0367
23(Al_2O_3)	SC4	0.00212	0.0293

Table 4.21: The parameters listed in this table are the resulting fit of the light yield to MeVee calibration. The parameters a and b represent the values in Eq. (4.9).

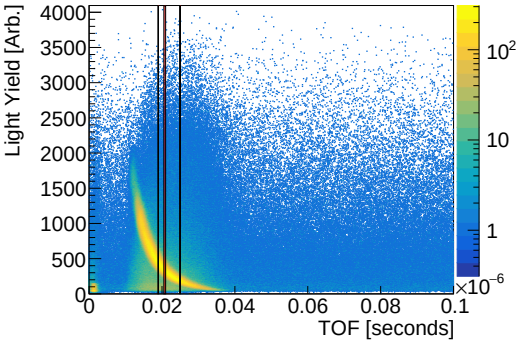

(a) TC-All SCs. Y-axis is LY in TC.

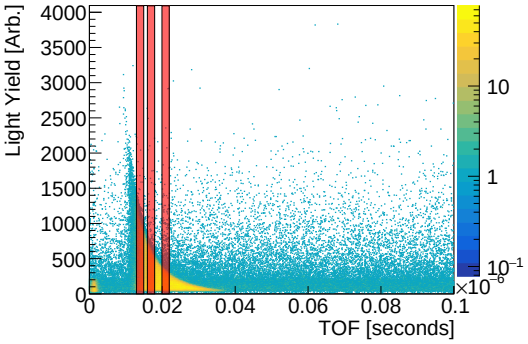

(b) TC-SC1. Y-axis is LY in SC1.

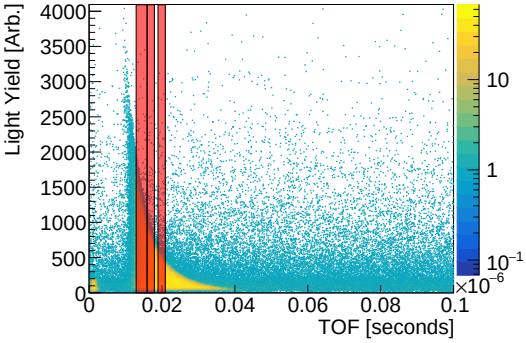

(c) TC-SC2. Y-axis is LY in SC2.

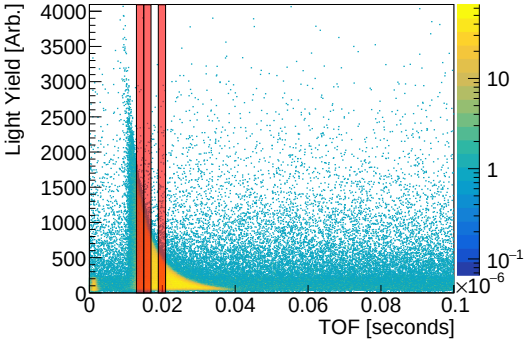

(d) TC-SC3. Y-axis is LY in SC3.

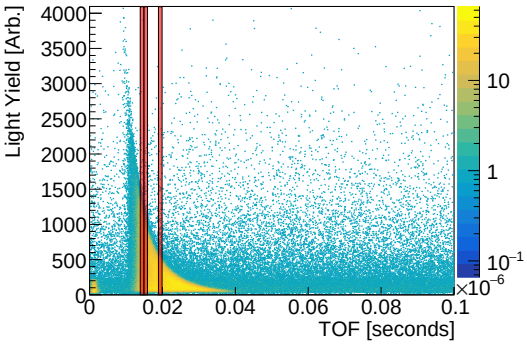

(e) TC-SC4. Y-axis is LY in SC4.

Figure 4.26: Measured TOF versus light yield for dataset 14(^{56}Fe). Red bands indicate the TOF slices used for LY calibration.

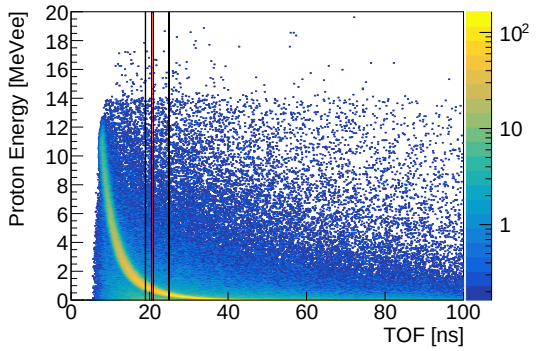

(a) TC-All SCs. Y-axis is proton energy deposited in TC.

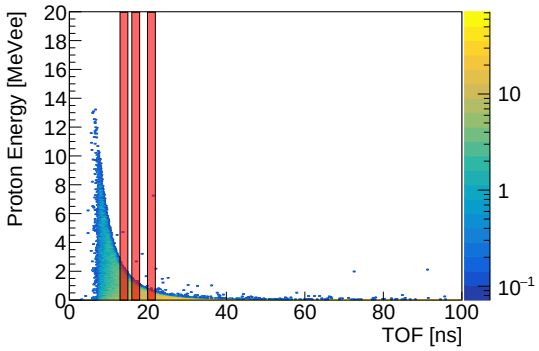

(b) TC-SC1. Y-axis is proton energy deposited in SC1.

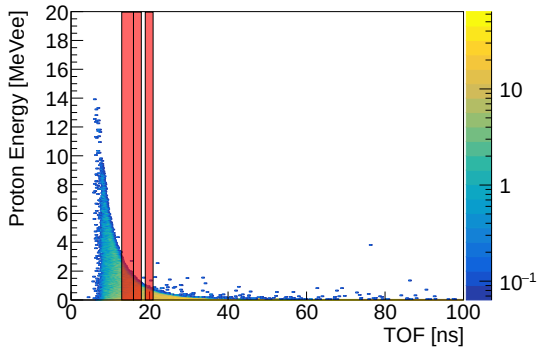

(c) TC-SC2. Y-axis is proton energy deposited in SC2.

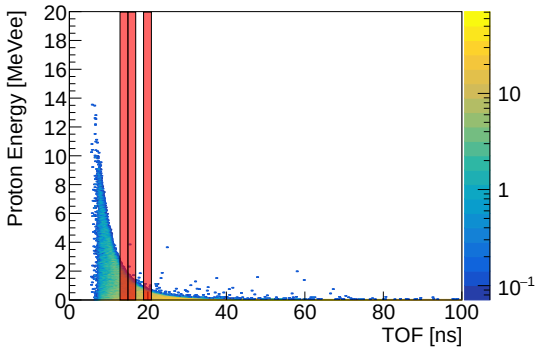

(d) TC-SC3. Y-axis is proton energy deposited in SC3.

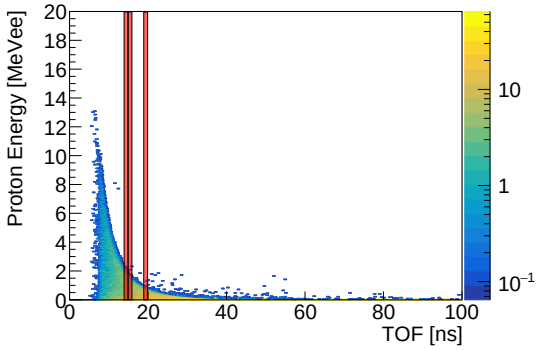

(e) TC-SC4. Y-axis is proton energy deposited in SC4.

Figure 4.27: Simulated TOF versus proton energy deposited (in MeVee) for dataset 14(^{56}Fe).

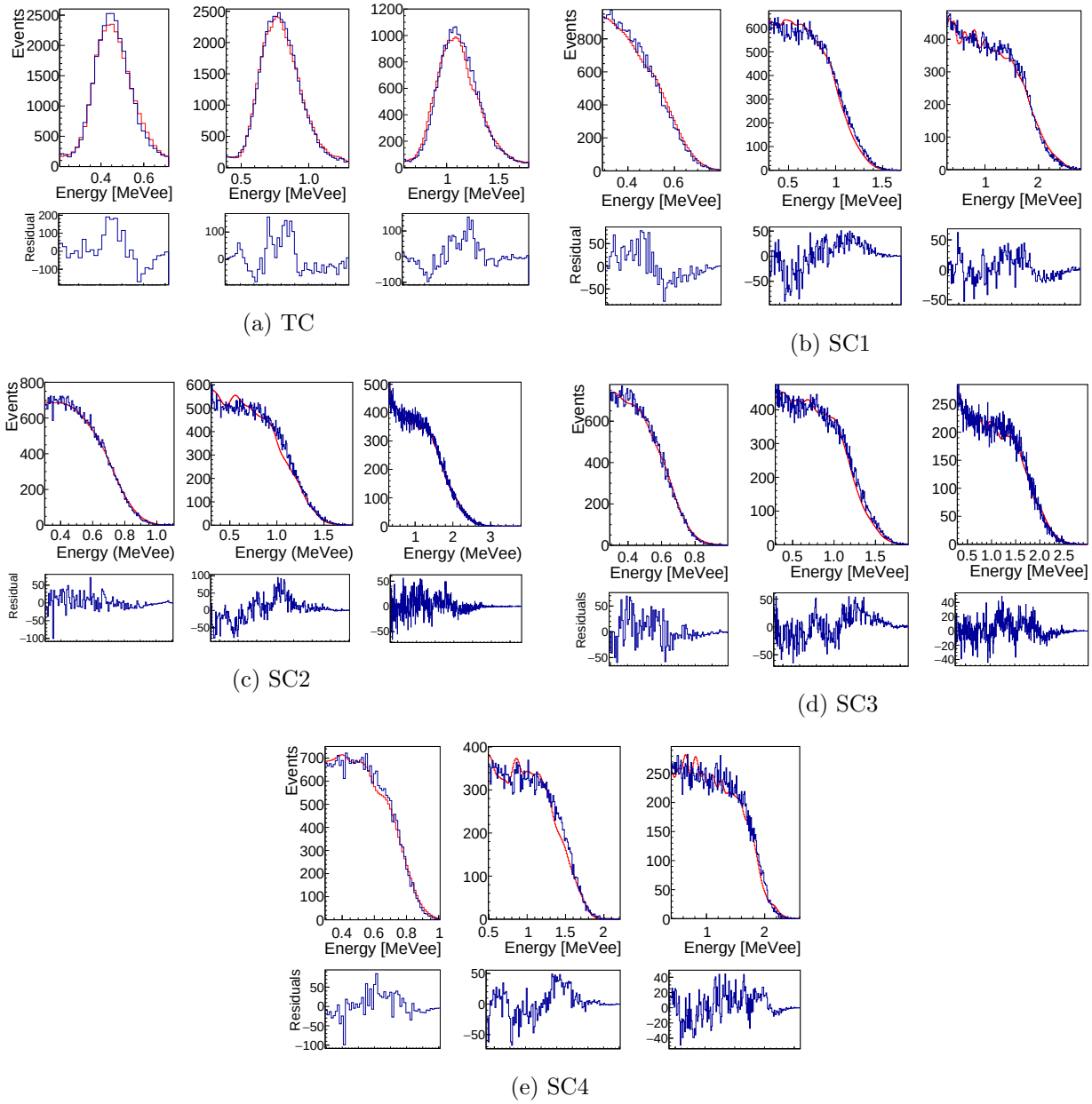

(a) TC

(b) SC1

(c) SC2

(d) SC3

(e) SC4

Figure 4.28: TOF versus proton energy deposited (in MeVee) histogram for dataset 14(^{56}Fe). The blue lines in the top plots are the experimental data, and the red lines in the top plots are the simulation results smeared by the energy resolution function. The bottom plots are the residuals between the red and blue lines from the top plots.

4.1.10 Efficiency Modeling

The efficiency spectrum for the spectrometer configuration is determined by the Geant4 simulation. The known initial energies of valid coincident events are tallied. A valid coincidence is an event where the neutron elastically scattered off of a hydrogen atom in the target cell, and then deposited energy within a single scatter cell. Events that scattered multiple times within the TC scintillator were rejected. The LY cuts from Sections 4.1.6.1 and 4.1.6.2 are implemented in the efficiency calibration. This is achieved by converting the cuts into units of MeVee using the LY calibration from Table 4.21. The proton energy vs LY cut from Section 4.1.6.2 used the simulated timestamps of the first proton energy deposition in each detector to estimate the TOF-determined proton recoil energy. The simulated TOFs were also smeared using a random number generated from a Gaussian probability distribution with an σ of the appropriate timing resolutions from Table 4.15.

Events where the neutron scattered off a carbon in the TC were rejected. The simulated deposition energy was converted to LY in units of MeVee as described in Section 4.1.9. Each bin in the tallied spectrum is normalized to the total number of simulated neutrons that started in the energy range of that bin to calculate the energy-dependent efficiency, shown in Fig. 4.29.

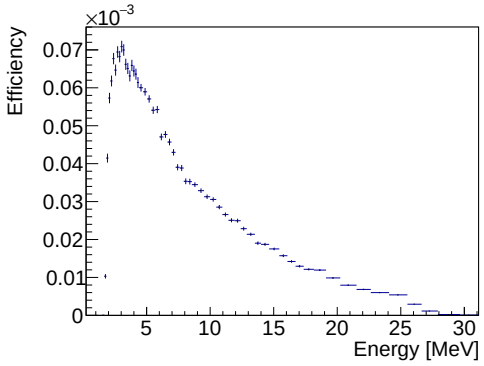

(a) Dataset 14(^{56}Fe) Configuration.

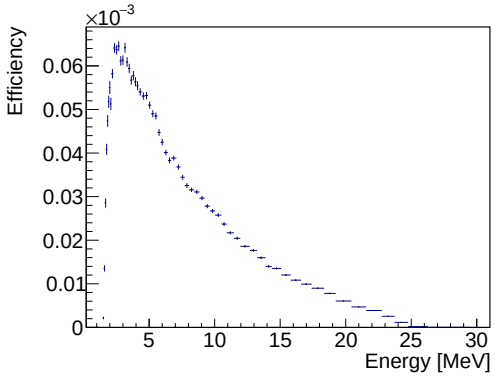

(b) Dataset 14(NaCl) Configuration.

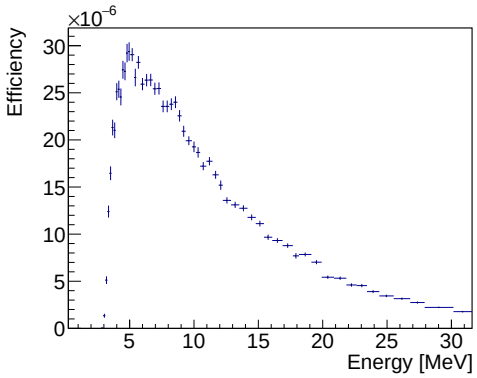

(c) Dataset 23(Al_2O_3) Configuration.

Figure 4.29: Simulated efficiency curves for all datasets.

4.1.11 STOF Energy Spectra (Counts)

The energy spectrum is tallied for each dataset. Rejected single events include the flagged pileup events and input saturated events from Section 4.1.2, the PSD-based upper γ event cut and the pileup event cut from Section 4.1.4, and the LY cut from Section 4.1.6.1. Additionally, the coincident event cut from Section 4.1.6.2 is implemented. A timing window equal to one cyclotron pulse width is used to determine the coincidences. The incoming neutron energy is determined using the measured TOF, distances, and angles using the methodology as described in Section 2.1.1.1. The resulting histograms are shown in Figs. 4.30 to 4.32. Notably, Fig. 4.31 for dataset 14(NaCl), shows a significant background not present in the other two datasets shown in Figs. 4.30 and 4.32. This is due to the gate-saturated events not being rejected as previously described in Sections 4.1.2 and 4.1.6.

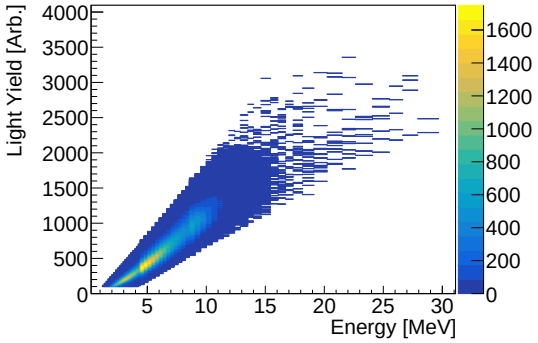

(a) Y-axis is the measured LY in the TC for the coincident event and the x-axis is the incoming neutron energy as determined by TOF and kinematics from Section 2.1.1.1.

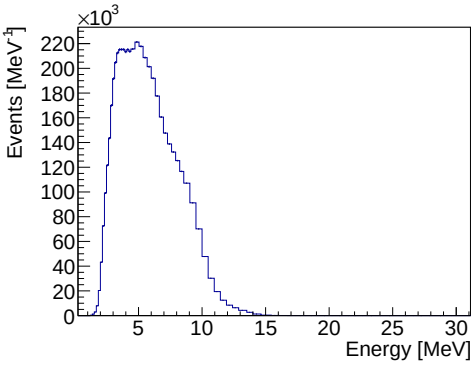

(b) x-projection of Fig. 4.30a.

Figure 4.30: Raw energy spectra for dataset 14(^{56}Fe).

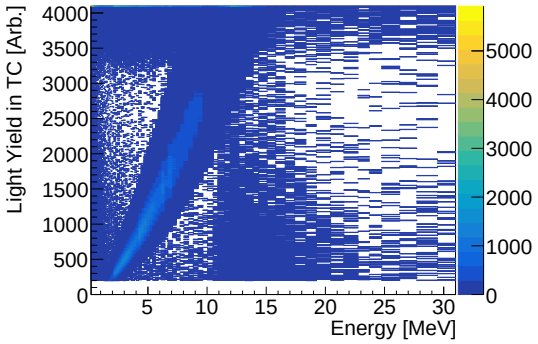

(a) Y-axis is the measured LY in the TC for the coincident event and the x-axis is the incoming neutron energy as determined by TOF and kinematics from Section 2.1.1.1.

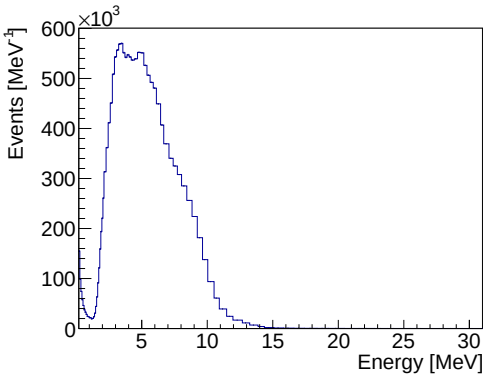

(b) x-projection of Fig. 4.30a.

Figure 4.31: Raw energy spectra for dataset 14(NaCl).

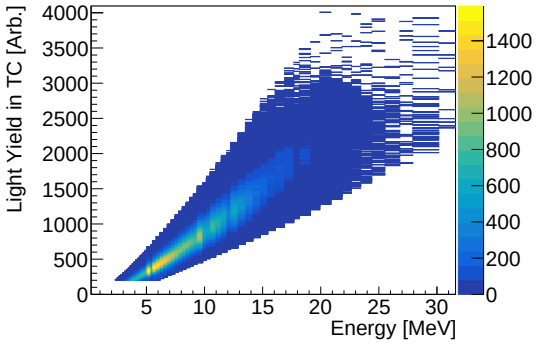

(a) Y-axis is the measured LY in the TC for the coincident event and the x-axis is the incoming neutron energy as determined by TOF and kinematics from Section 2.1.1.1.

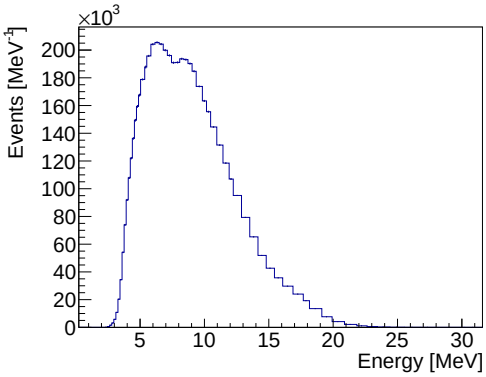

(b) x-projection of Fig. 4.30a.

Figure 4.32: Raw energy spectra for dataset 23(Al_2O_3).

4.1.12 Background Spectra

A background spectrum of random uncorrelated events is determined to subtract from the STOF energy spectra result from Section 4.1.11.

Numerous energy spectra were tallied using multiple time window ranges for the datasets, far removed in time from the triggering event. Figure 4.33 is the results of tallying coincidences with an SC detection within a time window between 2 and 3 cyclotron pulse lengths after the detected TC event, etc..., up to between 5 and 6 cyclotron pulse lengths. The events in these pulses consist primarily either of random coincident events from radiation interactions in the PMT or uncorrelated neutron interactions in the scintillators. This effect is consistent between cyclotron pulses. There is also a contribution of coincident events from neutrons that have interacted within the TC, scattered into the environment, and then scattered into the SC. These long-TOF events should not be included in this background subtraction, since their effect is not consistent between cyclotron pulses. Contributions from these events decrease over time and so are expected to be negligible at long time periods from the initial TC event. To minimize the possibility of these events in the background, only events beyond the second cyclotron pulse were included in this analysis.

For each group of tallied events, the TOF is subtracted by the starting value of the TOF window (e.g. the coincidences found between 2 and 3 cyclotron pulse lengths are subtracted by 2 cyclotron pulse). These TOF values are converted to "energy" following the same method in Section 2.1.1.1 resulting in a series of background event histograms, shown in Figs. 4.30b, 4.31b and 4.32b, where each bin represents the background of the corresponding bin in the energy histogram. The background determined this way has a very low number of counts, and so has a high variance between bins. This means that there is a high risk of

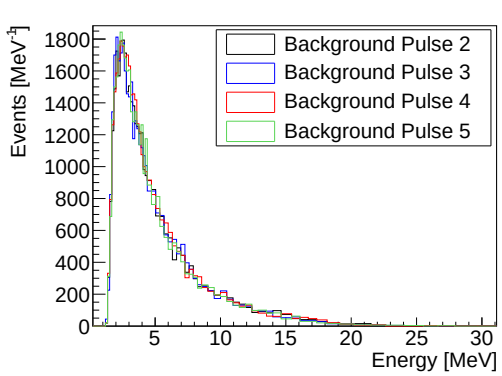

(a) Dataset 14(^{56}Fe).

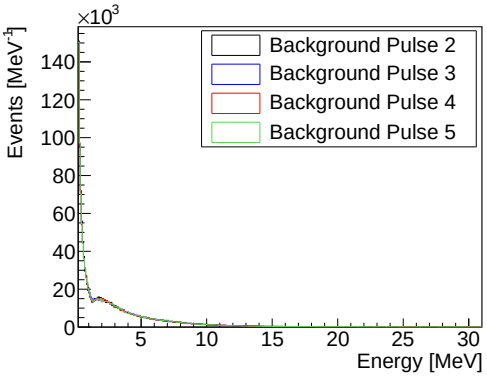

(b) Dataset 14(NaCl).

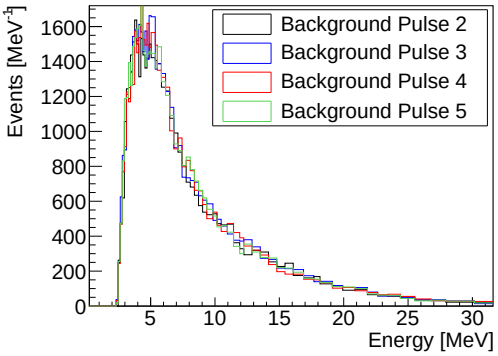

(c) Dataset 23(Al_2O_3).

Figure 4.33: Background histogram for each dataset. The black line represents events between 2×cyclotron pulse width (CPW) and 3×CPW. The blue line represents events between 3×CPW and 4×CPW. The red line represents events between 4×CPW and 5×CPW. The green line represents events between 5×CPW and 6×CPW. The measured TOF is subtracted by the beginning time of the interval it is in, this TOF is used to calculate an "incoming neutron energy." X-axis bin structure is correlated with the bin structure in the raw energy spectra, Figs. 4.30 to 4.32.

significantly over-subtracting or under-subtracting counts from the energy histogram, which is a concern for the edges of the measured spectrum where the counts are low. Therefore, the average across the four histograms from the start of the 2nd cyclotron pulse length to the end of the 5th cyclotron pulse length is used as the spectrum for performing a background subtraction.

Figure 4.34 shows the averaged background spectrum (black lines). Additionally, the spectrum from the last pulse (5th pulse) analyzed is plotted (red line) alongside the ratio of the two spectrum. The ratio plot shows that the average is randomly distributed about 1, indicating that the spectrum does not have an energy (time) bias.

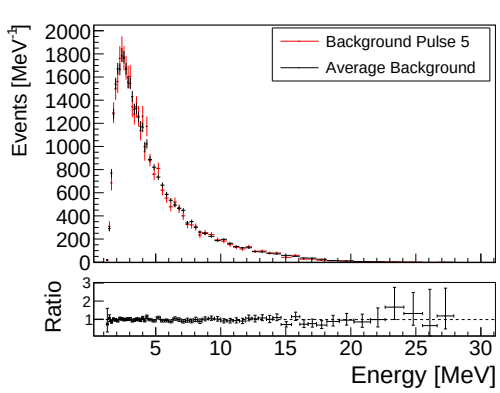

(a) Dataset 14(^{56}Fe).

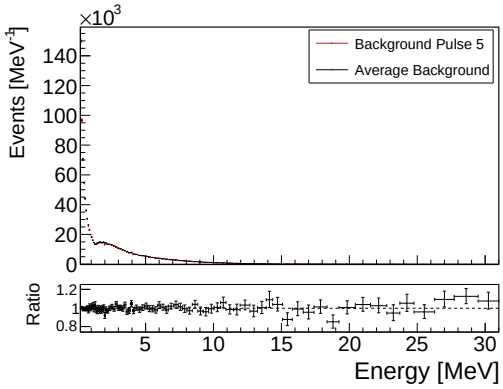

(b) Dataset 14(NaCl).

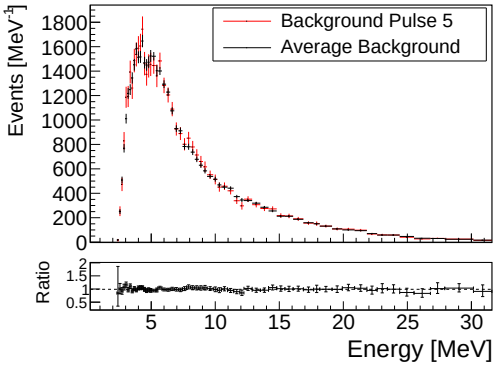

(c) Dataset 23(Al_2O_3).

Figure 4.34: The mean background histograms for each dataset. The black line represents the average of the corresponding plots in Fig. 4.33. The red line is the "Background Pulse 5" from Fig. 4.33. The bottom plot is the ratio between the black and red lines.

The background histogram for dataset 14(NaCl) is notably larger than the other two datasets. This is due to the gate-saturation events as described in Section 4.1.2. These events cannot be rejected based on LY cuts, resulting in the larger background that is

observed here. Since there is a larger background to subtract, the resulting spectrum for dataset 14(NaCl) has a larger relative error.

4.1.13 STOF Flux Spectrum

The final STOF incoming neutron energy spectra are shown in Figs. 4.35 to 4.37. The mean background spectrum, see Fig. 4.34, is subtracted from the energy spectra, and then it is normalized to the average current (see Table 3.1), the livetime (see Table 4.20), the efficiency spectrum (see Fig. 4.29), and the solid angle (calculated from information in Table 3.3). The uncertainty in the plot includes the Poisson statistical uncertainties associated with the raw energy spectrum, the background spectrum, and the efficiency spectrum. All datasets have large errors and unrealistic spikes in flux for the lowest 2-3 bins. The timing resolution of the spectrometer translates to an energy uncertainty greater than the chosen bin widths. This primarily results in a smoothing of bin-scale features in most of the spectrum where there are sufficient statistics and the efficiency curve is not rapidly changing. However, the high sensitivity near the threshold is expected to cause the extreme discontinuities observed, due to misattributed neutron flux in bins where the model predicts near-zero efficiency. Therefore, the bins at the low energy end that curve upwards are excluded (the excluded bins are listed in Appendix A).

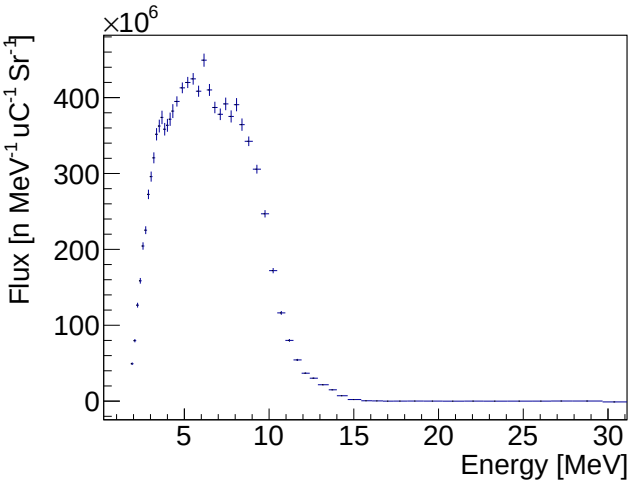

Figure 4.35: The STOF-determined neutron flux for dataset 14(^{56}Fe). The first 2 non-zero bins are excluded.

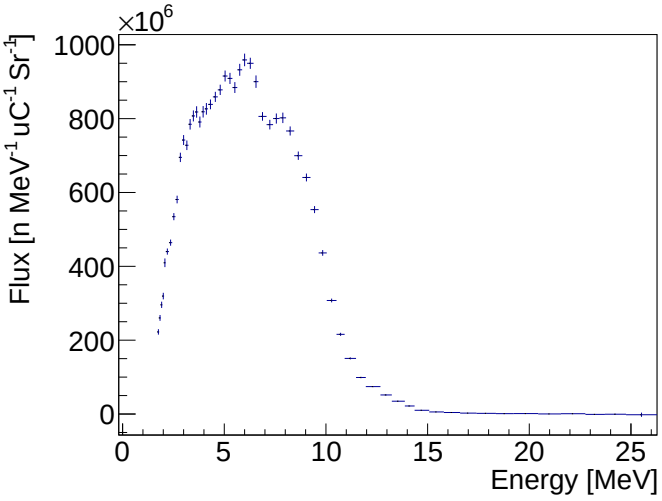

Figure 4.36: The STOF-determined neutron flux for dataset 14(NaCl). The first 3 non-zero bins are excluded.

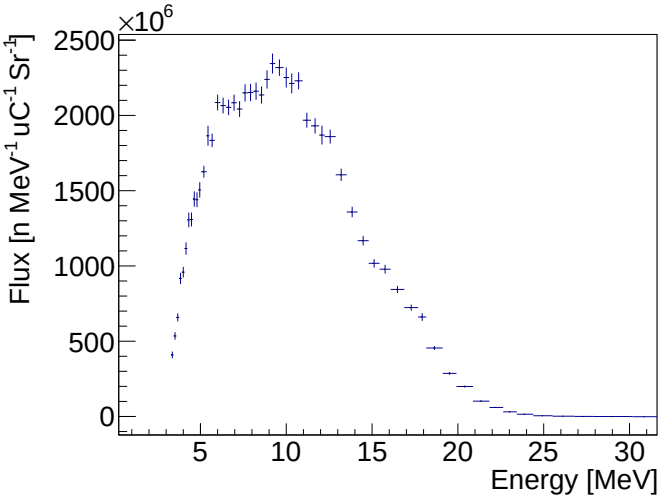

Figure 4.37: The STOF-determined neutron flux for dataset 23(Al_2O_3). The first 3 non-zero bins are excluded.

4.2 Activation Foil Analysis

Three threshold reactions were selected for activation analysis for all datasets, ^{115}In(n,n')^{115m}In, ^{58}Ni(n,p)^{58}Co and ^{27}Al(n,α)^{24}Na. For dataset 23(Al_2O_3) an additional two threshold reactions, ^{90}Zr(n,2n)^{89}Zr and ^{197}Au(n,2n)^{196}Au, were analyzed. These reactions were chosen for two reasons. First, each cross section [45], shown in Fig. 4.38, exhibits thresholds at different energies. This allows some insight into the energy dependence of the neutron flux. Second, each reaction produces an isolated photopeak that is easily measured by a high purity Germanium (HPGe) detector.

Foil packs consisting of stacked foils of indium, nickel, aluminum, gold, and/or zirconium were placed in the neutron beam, in place of the GENESIS target, for each experiment. The irradiation time for each dataset is listed in Table 4.22. These foils were transferred to a coaxial HPGe detector in a lead-shielded container. Spectra were collected for each foil using the GammaVision acquisition software [39]. The Fitzpeaks [40] software was used to perform the energy calibration and peak fitting.

Dataset	t_{irr} [s]	Average Current [μA]
14(^{56}Fe)	7218	8.39
14(NaCl)	8412	13.72
23(Al_2O_3)	7752	3.57

Table 4.22: Activation foil irradiation times, t_{irr}, and average current during irradiation.

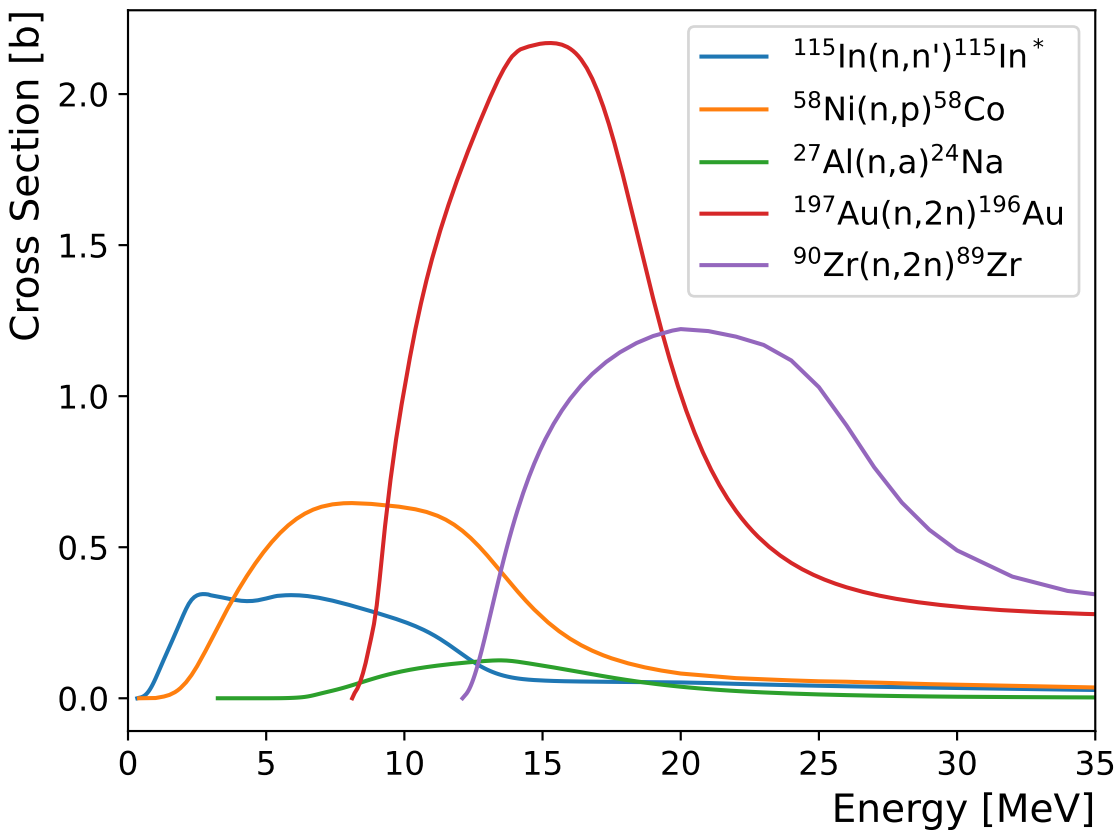

Figure 4.38: Reaction cross sections from IRDFF-II [45].

4.2.1 Gamma Spectrum Energy Calibration and Efficiency Determination

A spectrum was measured of a ^{152}Eu sealed source, to obtain an energy calibration for each measured activation foil dataset. A spread of 10 isolated peaks were chosen across the measured spectrum range to estimate a linear fit to use as the energy calibration. The peak fitting and energy calibration were done using the Fitzpeaks software package. The measured spectra are shown in Figs. 4.39 to 4.41. The dashed red lines in these spectra represent the fitted centroids for the peaks used in the energy calibration. Tables 4.24 to 4.26 list the fitted channel mean, the reference energy from literature, and the fitted energy centroid post implantation of the energy calibration. The ^{152}Eu peaks were used to find a first-order linear energy calibration fit of the form,

$$E = A_0 + A_1 * Ch, \tag{4.11}$$

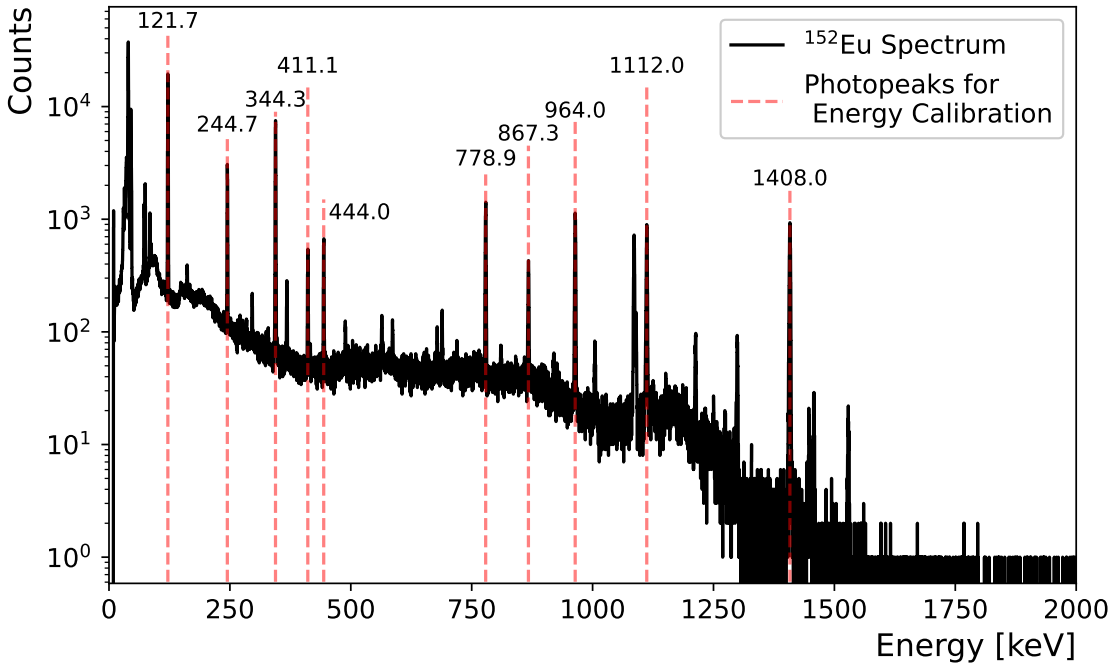

Figure 4.39: ^{152}Eu γ spectra from dataset 14(^{56}Fe). The red dashed lines are the peaks used for the energy calibration.

where A_0 and A_1 are the fit parameters, E is the energy in keV, and Ch is the spectrum channel number. The fitted parameters for each dataset are tabulated in Table 4.23.

Dataset	A_0	A_1
14(^{56}Fe)	-0.0771	0.187
14(NaCl)	0.0492	0.194
23(Al_2O_3)	0.0681	0.194

Table 4.23: Energy calibrations for each dataset using the peaks from a ^{152}Eu source. A_0 and A_1 are the fitted parameters to the functional form found in Eq. (4.11).

The detector used for these measurements has undergone a detailed characterization by Dr. Bleuel [46]. The efficiency curve from this characterization was used for the collected datasets.

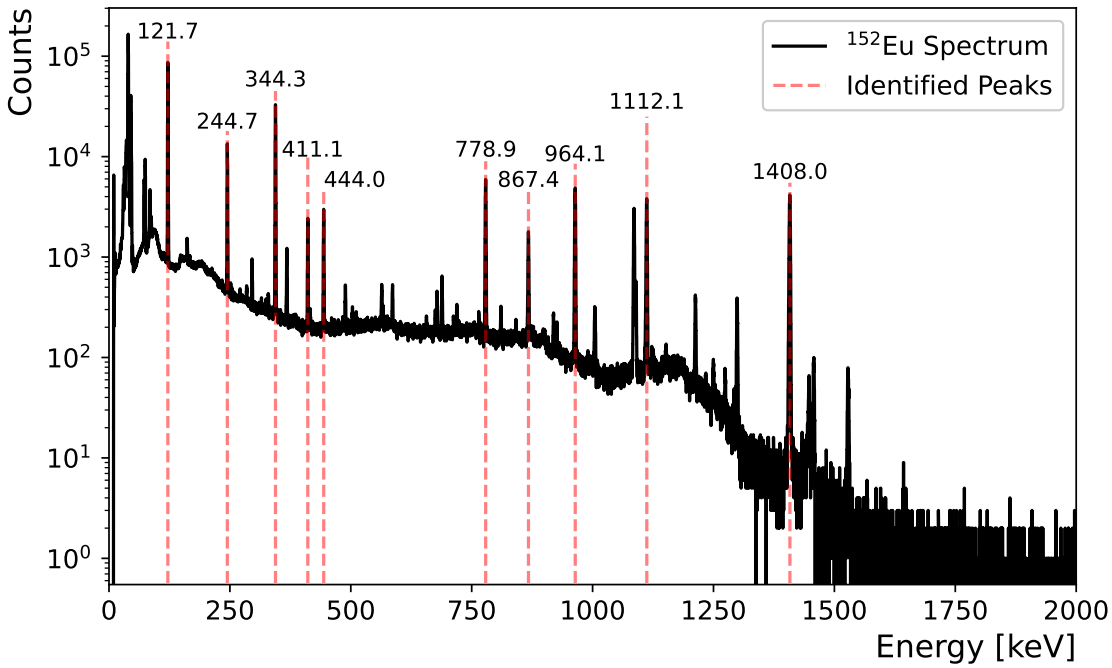

Figure 4.40: ^{152}Eu γ spectra from dataset 14(NaCl). The red dashed lines are the peaks used for the energy calibration.

Channel #	Ref. Energy [keV]	Centroid [keV]
650.2	121.78	121.71
1306.9	244.70	244.71
1838.6	344.28	344.32
2195.4	411.13	411.15
2370.9	443.96	444.01
4158.9	778.90	778.92
4631.1	867.38	867.37
5147.1	964.10	964.02
5937.6	1112.10	1112.08
7517.6	1408.00	1408.04

Table 4.24: ^{152}Eu peak information for energy calibration for dataset 14(^{56}Fe). The "Channel #" is the fitted mean of the peak. The "Ref. Energy" is the peak energy from the literature [47]. The "Centroid" is the estimated energy of the peak after energy calibration.

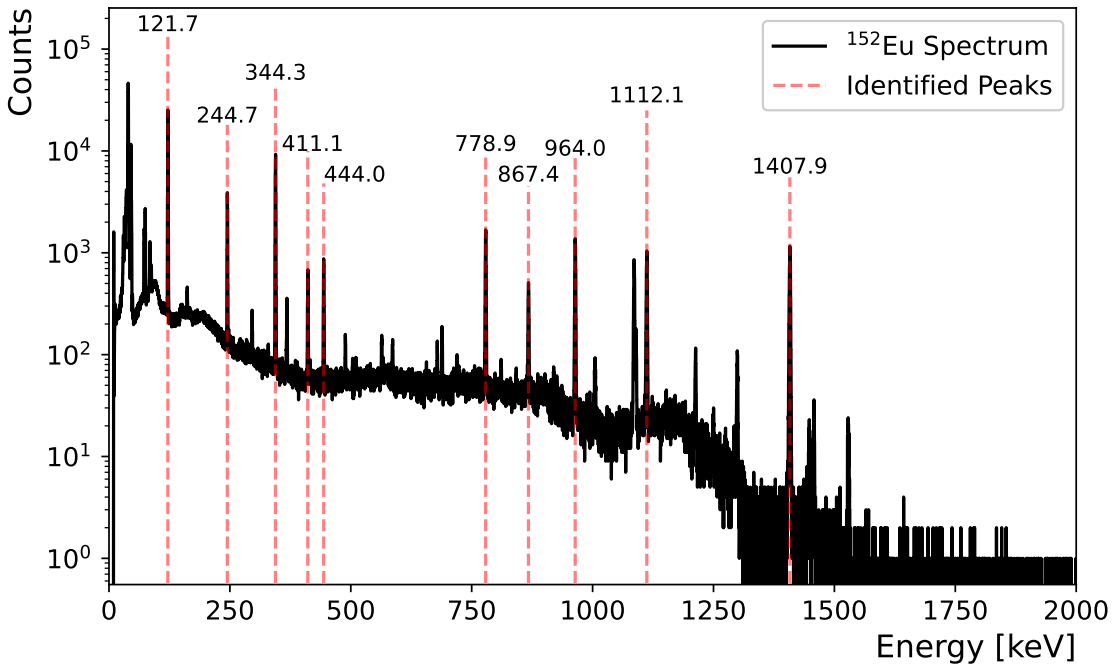

Figure 4.41: ^{152}Eu γ spectra from dataset 23(Al_2O_3). The red dashed lines are the peaks used for the energy calibration.

Channel #	Ref. Energy [keV]	Centroid [keV]
626.7	121.78	121.73
1259.9	244.70	244.70
1772.8	344.28	344.30
2117.1	411.13	411.14
2286.2	443.96	443.98
4011.2	778.90	778.94
4466.7	867.38	867.39
4964.6	964.10	964.07
5726.8	1112.10	1112.08
7250.8	1408.00	1408.00

Table 4.25: ^{152}Eu peak information for energy calibration for dataset 14(NaCl). The "Channel #" is the fitted mean of the peak. The "Ref. Energy" is the peak energy from the literature [47]. The "Centroid" is the estimated energy of the peak after energy calibration.

Channel #	Ref. Energy [keV]	Centroid [keV]
626.1	121.78	121.72
1259.0	244.70	244.70
1771.6	344.28	344.30
2115.6	411.13	411.15
2284.6	443.96	443.98
4008.4	778.90	778.95
4463.5	867.38	867.38
4961.0	964.10	964.06
5722.9	1112.10	1112.09
7245.7	1408.00	1407.99

Table 4.26: ^{152}Eu peak information for energy calibration for dataset 23(Al_2O_3). The "Channel #" is the fitted mean of the peak. The "Ref. Energy" is the peak energy from the literature [47]. The "Centroid" is the estimated energy of the peak after energy calibration.

4.2.2 Gamma Spectra for Foils

The measured γ spectra are shown in Figs. 4.42, 4.45 and 4.48. Fitzpeaks was used to find and fit peaks above 200 keV. All peaks that are greater than 10% of the photopeak of interest are identified. The red dashed lines represent photopeaks as a result of the activated foil and positron-electron annihilation. The blue dashed lines are photopeaks from background isotopes (e.g. ^{40}K or photopeaks from Uranium decay). For some of the measured spectra, there are distinctive sawtooth peak shapes. These are caused by neutron reactions within the Germanium. These neutrons come from secondary comic rays (e.g. muons) reacting within the lead shielding around the detector. All the photopeaks (red and blue lines) are tabulated in Tables 4.27 to 4.29. For datasets 14(^{56}Fe) and 14(NaCl) there were three photopeaks of interest, the peak at 336 keV due to the ^{115}In(n,n') reaction, the peak at 810 keV due to the ^{58}Ni(n,p) reaction, and the peak at 1369 keV due to the ^{27}Al(n,a) reaction. For dataset 23(Al_2O_3) there were two additional peaks considered, the peak at 909.15 keV due to the ^{90}Zr(n,2n) reaction and the peak at 355.73 keV due to the ^{197}Au(n,2n) reaction. The fitted results and relevant nuclear data for each of these peaks is listed in Table 4.30.

Foil	Centroid	Ref. Energy [47]	Source
In	336.3	336.241	^{115}In(n,n')^{115}In
In	391.7	391.698	^{115}In(n,3n)^{113}In
In	416.9	416.90	^{115}In(n, γ)^{116}In
In	1097.2	1097.28	^{115}In(n,γ)^{116}In
In	1293.6	1293.56	^{115}In(n,γ)^{116}In
Ni	205.3	205.311	^{235}U (UA)
Ni	238.7	238.632	^{212}Pb (Th)
Ni	241.8	241.995 +	^{214}Pb (U) + ^{224}Ra (Th)
Ni	295.3	295.224	^{214}Pb (U)
Ni	352.0	351.9320 + 351.07	^{214}Pb (Th) + ^{211}Bi (UA)
Ni	511.1	511.0	Annihilation
Ni	583.3	583.187	^{208}Tl (Th)
Ni	609.4	609.321	^{214}Bi (U)
Ni	803.2	803.06	^{206}Pb(n,n'γ)^{206}Pb
Ni	810.9	810.7593	^{58}Ni(n,p)^{58}Co
Ni	911.3	911.204	^{228}Ac (Th)
Ni	1001.2	1001.03	^{234m}Pa (U)
Ni	1461.0	1460.820	^{40}K
Ni	2615.1	2614.511	^{208}Tl (U)
Al	238.7	238.632	^{212}Pb (Th)
Al	295.4	295.224	^{214}Pb (U)
Al	352.0	351.9320 + 351.07	^{214}Pb (Th) + ^{211}Bi (UA)
Al	511.0	511.0	Annihilation
Al	583.0	583.187	^{208}Tl (Th)
Al	609.3	609.321	^{214}Bi (U)
Al	911.2	911.204	^{228}Ac (Th)
Al	1000.9	1001.03	^{234m}Pa (U)
Al	1368.5	1368.625	^{27}Al(n,α)^{24}Na
Al	1460.8	1460.820	^{40}K
Al	2614.4	2614.511	^{208}Tl (U)
Al	2754.1	2754.008	^{27}Al(n,α)^{24}Na

Table 4.27: Tabulation of the fitted photopeaks for all the foils in dataset 14(^{56}Fe). If the peak is from neutron irradiation, then the reaction and isotope are stated. *U* means the isotope comes from the Uranium-238 decay chain. *UA* means the isotope comes from the Uranium-235 decay chain. *Th* means the isotope comes from the Thorium-232 decay chain.

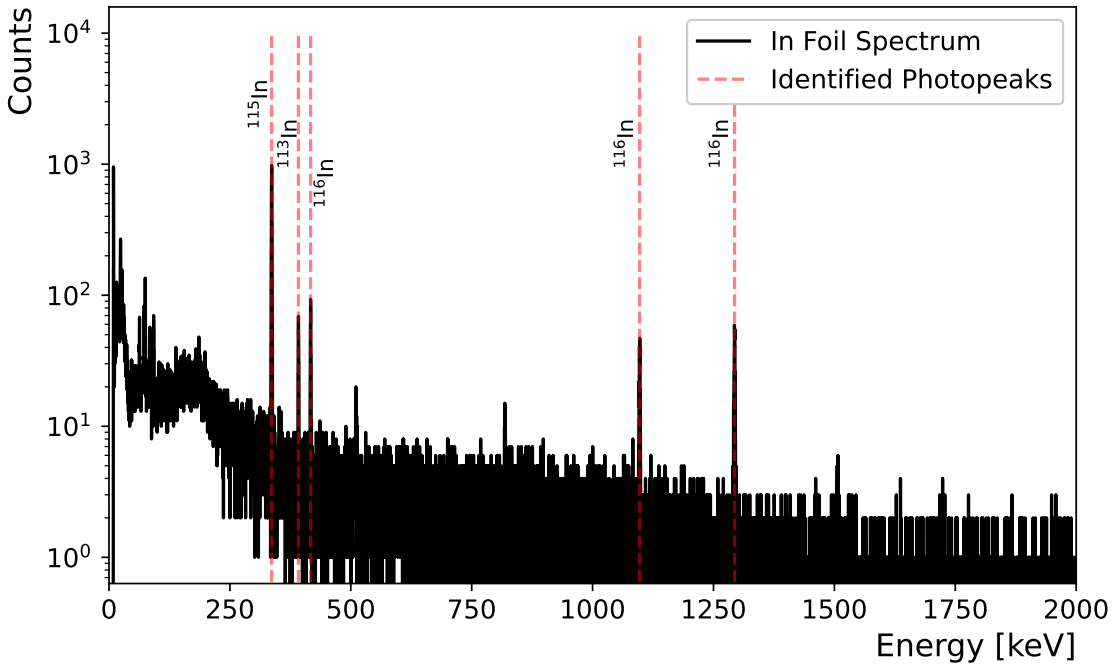

Figure 4.42: In foil γ spectra from dataset 14(^{56}Fe). The red dashed lines are photopeaks resulting from activation of the foil. Only peaks above 200 keV and greater than 10% of the peak at 336 keV are identified.

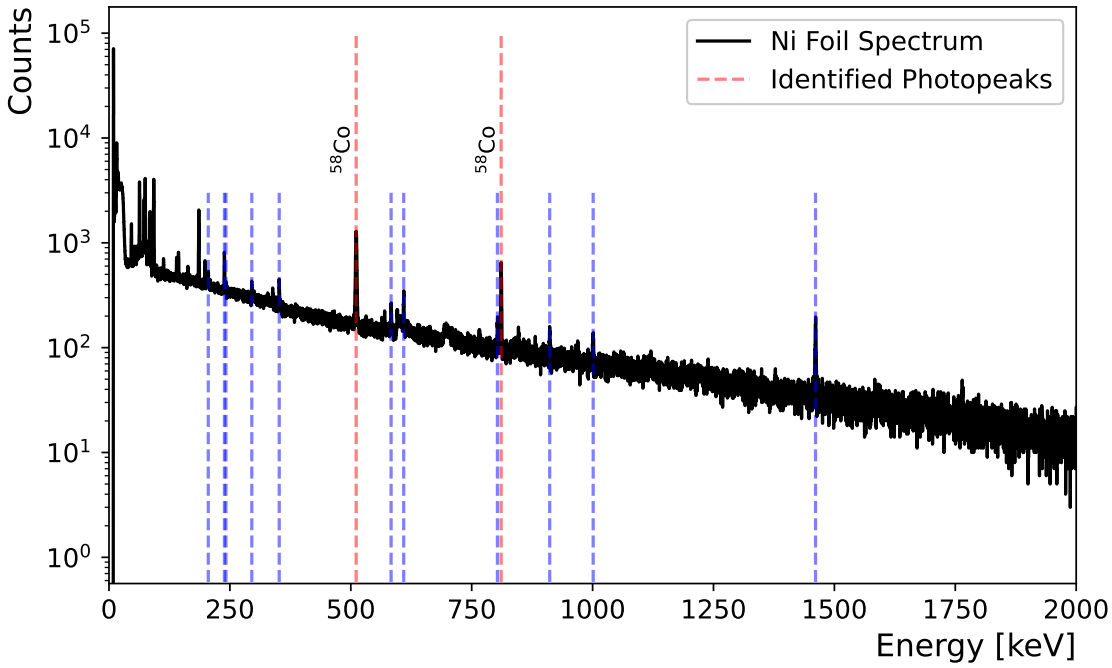

Figure 4.43: Ni foil γ spectra from dataset 14(^{56}Fe). The red dashed lines are photopeaks resulting from activation of the foil. The blue lines are background photopeaks. Only peaks above 200 keV and greater than 10% of the peak at 810 keV are identified.

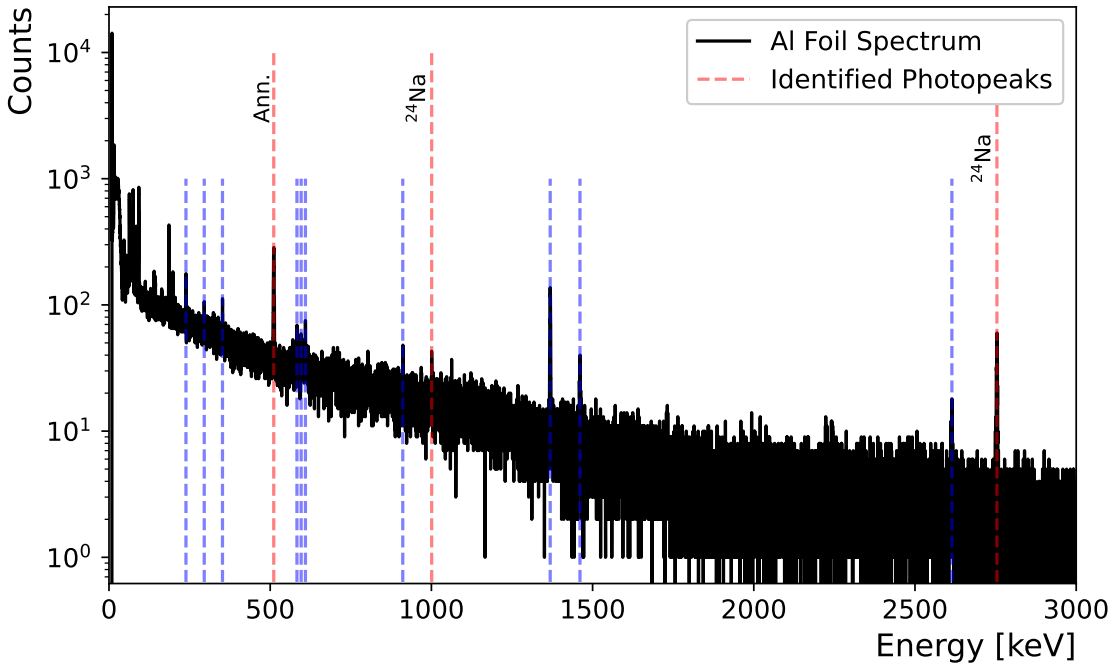

Figure 4.44: Al foil γ spectra from dataset 14(^{56}Fe). The red dashed lines are photopeaks resulting from activation of the foil. The blue lines are background photopeaks. Only peaks above 200 keV and greater than 10% of the peak at 1368 keV are identified.

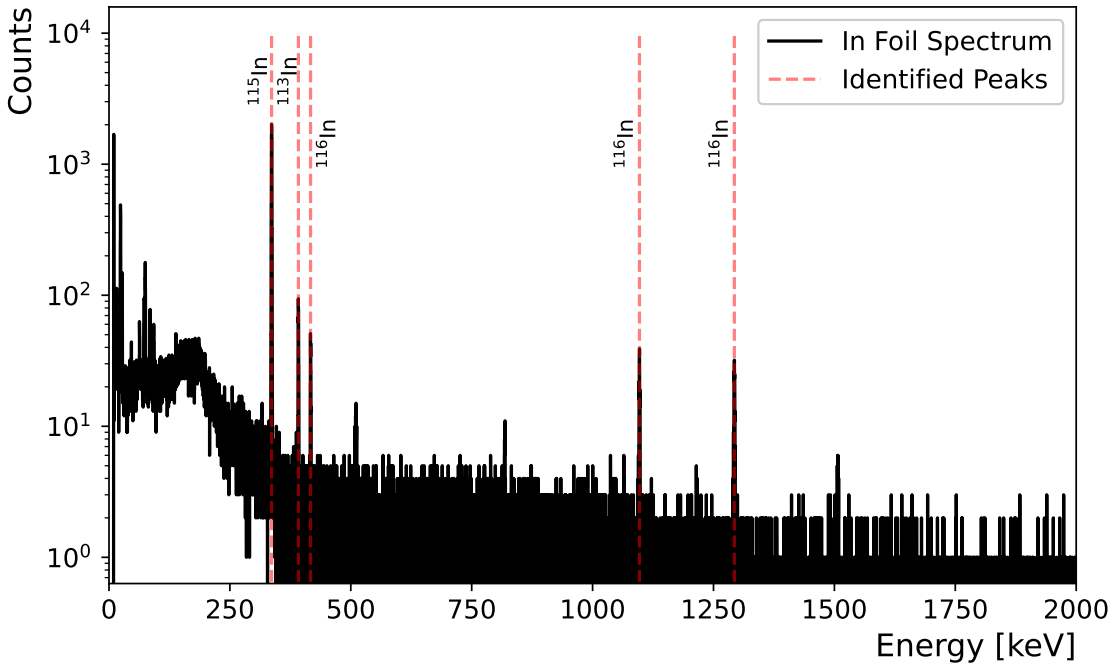

Figure 4.45: In foil γ spectra from dataset 14(NaCl). The red dashed lines are photopeaks resulting from activation of the foil. Only peaks above 200 keV and greater than 10% of the peak at 336 keV are identified.

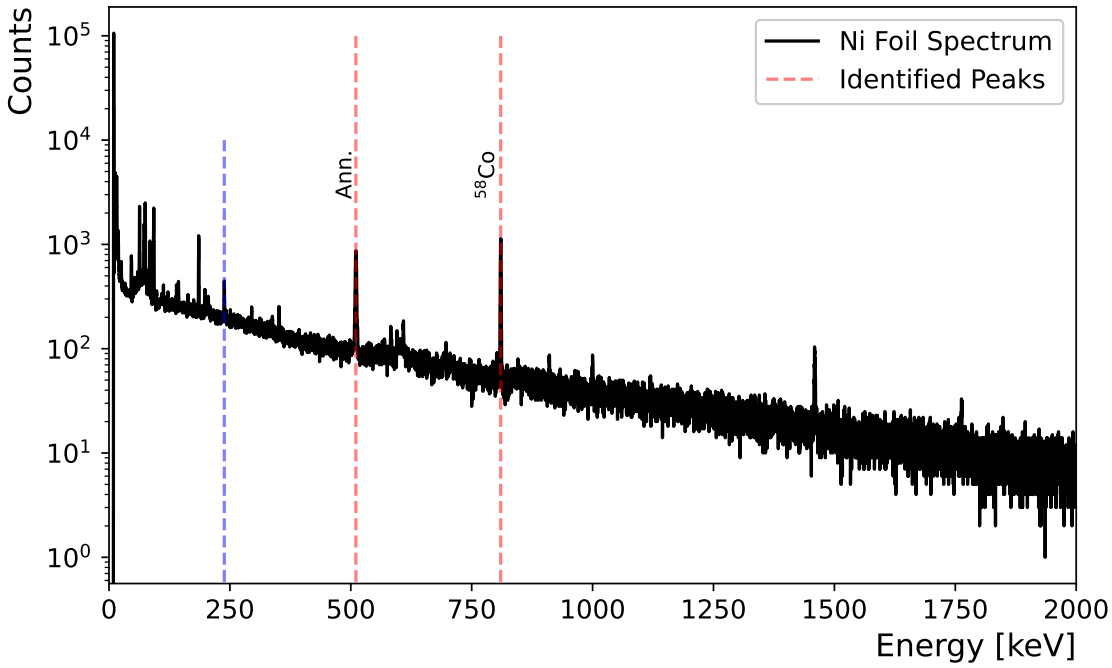

Figure 4.46: Ni foil γ spectra from dataset 14(NaCl). The red dashed lines are photopeaks resulting from activation of the foil. The blue lines are background photopeaks. Only peaks above 200 keV and greater than 10% of the peak at 810 keV are identified.

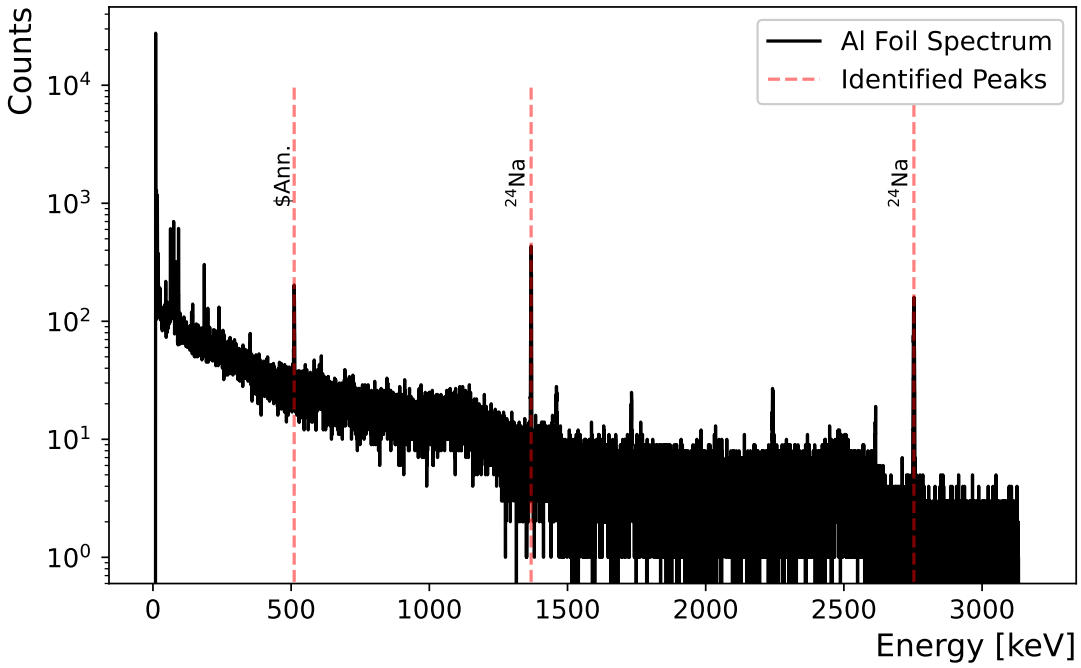

Figure 4.47: Al foil γ spectra from dataset 14(NaCl). The red dashed lines are photopeaks resulting from activation of the foil. The blue lines are background photopeaks. Only peaks above 200 keV and greater than 10% of the peak at 1368 keV are identified.

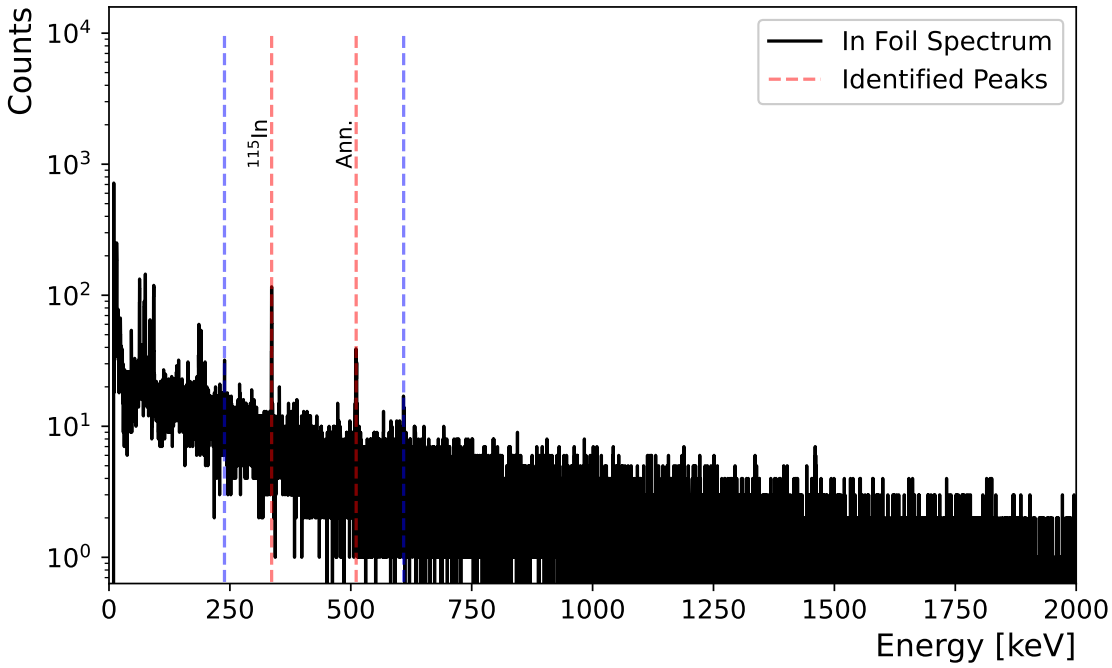

Figure 4.48: In foil γ spectra from dataset 23(Al_2O_3). The red dashed lines are photopeaks resulting from activation of the foil. Only peaks above 200 keV and greater than 10% of the peak at 336 keV are identified.

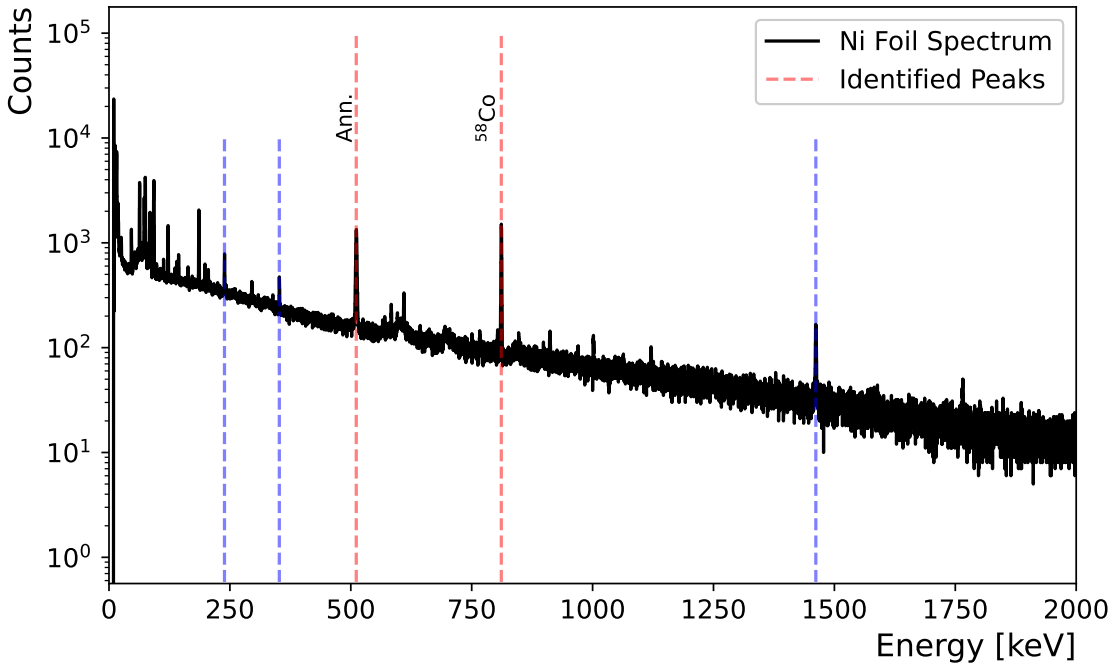

Figure 4.49: Ni foil γ spectra from dataset 23(Al_2O_3). The red dashed lines are photopeaks resulting from activation of the foil. The blue lines are background photopeaks. Only peaks above 200 keV and greater than 10% of the peak at 810 keV are identified.

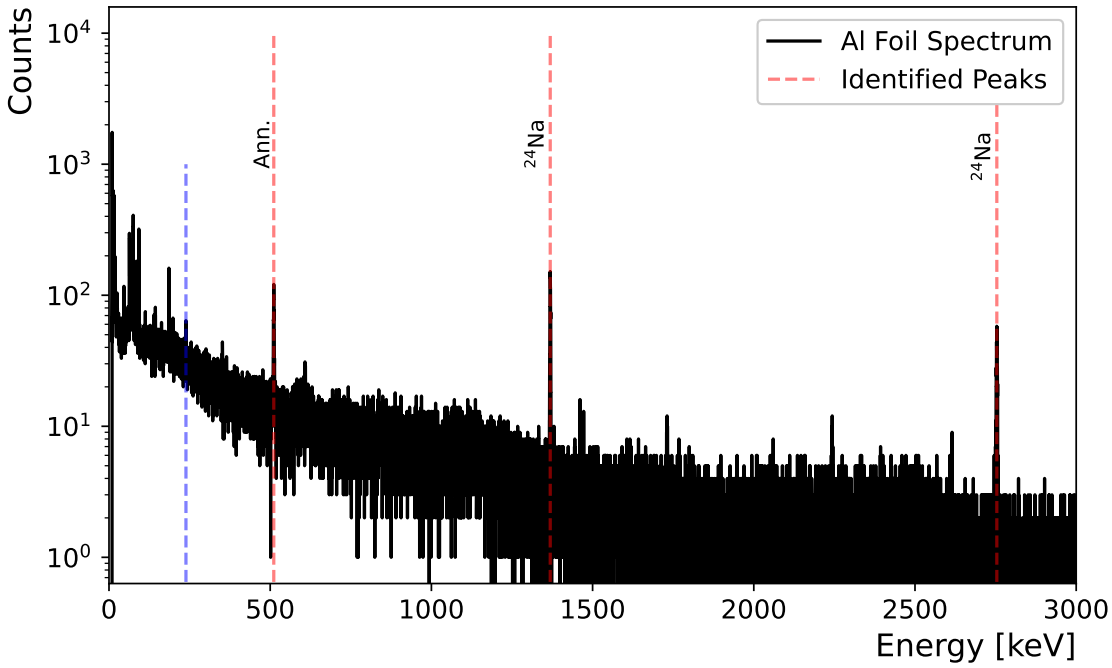

Figure 4.50: Al foil γ spectra from dataset 23(Al_2O_3). The red dashed lines are photopeaks resulting from activation of the foil. The blue lines are background photopeaks. Only peaks above 200 keV and greater than 10% of the peak at 1368 keV are identified.

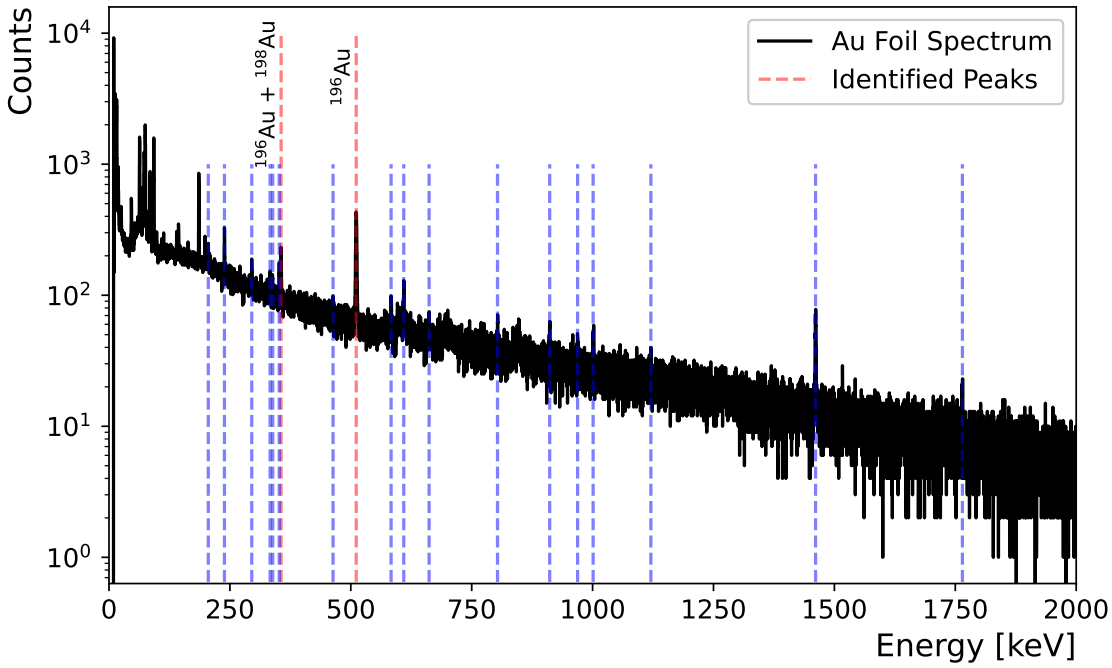

Figure 4.51: Au foil γ spectra from dataset 23(Al_2O_3). The red dashed lines are photopeaks resulting from activation of the foil. The blue lines are background photopeaks. Only peaks above 200 keV and greater than 10% of the peak at 355 keV are identified.

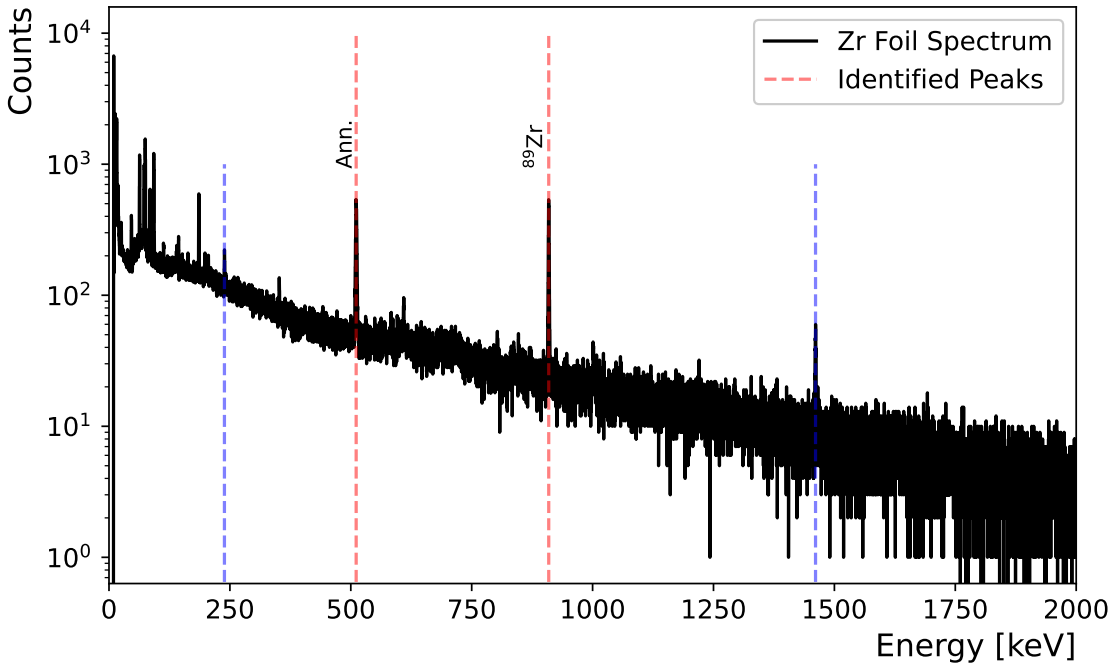

Figure 4.52: Zr foil γ spectra from dataset 23(Al_2O_3). The red dashed lines are photopeaks resulting from activation of the foil. The blue lines are background photopeaks. Only peaks above 200 keV and greater than 10% of the peak at 909 keV are identified.

Foil	Centroid	Ref. Energy [47]	Source
In	336.2	336.241	^{115}In(n,n')^{115}In
In	391.7	391.698	^{115}In(n,3n)^{113}In
In	416.8	416.90	^{115}In(n,γ)^{116}In
In	1096.9	1097.28	^{115}In(n,γ)^{116}In
In	1293.1	1293.56	^{115}In(n,γ)^{116}In
Ni	238.4	238.632	^{212}Pb (Th)
Ni	510.5	511.0	Annihilation
Ni	810.0	810.7593	^{58}Ni(n,p)^{58}Co
Al	511.0	511.0	Annihilation
Al	1368.5	1368.625	^{27}Al(n,α)^{24}Na
Al	2754.1	2754.008	^{27}Al(n,α)^{24}Na

Table 4.28: Tabulation of the fitted photopeaks for all the foils in dataset 14(NaCl). If the peak is from neutron irradiation, then the reaction and isotope are stated. *U* means the isotope comes from the Uranium-238 decay chain. *UA* means the isotope comes from the Uranium-235 decay chain. *Th* means the isotope comes from the Thorium-232 decay chain.

Foil	Centroid	Ref. Energy [47]	Source
In	238.8	238.632	^{212}Pb (Th)
In	336.3	336.241	^{115}In(n,n')^{115}In
In	511.1	511.0	Annihilation
In	609.3	609.321	^{214}Bi (U)
Ni	238.8	238.632	^{212}Pb (Th)
Ni	352.2	351.9320 + 351.07	^{214}Pb (Th) + ^{211}Bi (UA)
Ni	511.3	511.0	Annihilation
Ni	811.2	810.7593	^{58}Ni(n,p)^{58}Co
Ni	1461.6	1460.820	^{40}K
Al	238.7	238.632	^{212}Pb (Th)
Al	511.0	511.0	Annihilation
Al	1368.6	1368.625	^{27}Al(n,α)^{24}Na
Al	2753.8	2754.008	^{27}Al(n,α)^{24}Na
Au	238.7	238.632	^{212}Pb (Th)
Au	295.2	295.224	^{214}Pb (U)
Au	333.1	333.05 + 333.82	^{197}Au(n,2n)^{196}Au + ^{197}Au(n,γ)^{198}Au
Au	338.5	338.320	^{228}Ac (Th)
Au	352.0	351.9320 + 351.07	^{214}Pb (Th) + ^{211}Bi (UA)
Au	355.9	355.73	^{197}Au(n,2n)^{196}Au
Au	511.2	511.0	Annihilation
Au	583.3	583.187	^{208}Tl (Th)
Au	609.5	609.321	^{214}Bi (U)
Au	661.9	661.657	^{137}Cs
Au	911.3	911.204	^{228}Ac (Th)
Au	969.0	968.971	^{228}Ac (Th)
Au	1001.1	1001.03	^{234m}Pa (U)
Au	1120.5	1120.294	^{214}Bi
Au	1461.1	1460.820	^{40}K
Au	1764.7	1764.491	^{214}Bi (U)
Au	2614.9	2614.511	^{208}Tl (U)
Zr	238.7	238.632	^{212}Pb (Th)
Zr	511.1	511.0	Annihilation
Zr	909.3	909.15	^{90}Zr(n,2n)^{89}Zr
Zr	1461.0	1460.820	^{40}K

Table 4.29: Fitted photopeaks for all the foils in dataset 23(Al_2O_3). If the photopeak is from a background isotope, then the parent isotope is stated. If the peak is from neutron irradiation, then the reaction and isotope are stated. *U* means the isotope comes from the Uranium-238 decay chain. *UA* means the isotope comes from the Uranium-235 decay chain. *Th* means the isotope comes from the Thorium-232 decay chain.

Dataset	Foil	Centroid	Net Area [counts]	Uncertainty [%]	χ^2_ν	Intensity [%]
14(^{56}Fe)	In	336.9	7073	1.2	0.93	45.9
14(^{56}Fe)	Ni	810.9	5274	2.1	1.21	99.45
14(^{56}Fe)	Al	1368.5	1691	3.2	0.76	99.936
14(NaCl)	In	336.2	14773	0.9	0.77	45.9
14(NaCl)	Ni	810.0	10524	1.2	1.10	99.936
14(NaCl)	Al	1368.3	5271	1.6	1.12	99.936
23(Al_2O_3)	In	336.3	558	5.7	1.19	45.9
23(Al_2O_3)	Ni	811.2	12462	1.1	0.88	99.936
23(Al_2O_3)	Al	1368.6	1870	2.7	1.25	99.936
23(Al_2O_3)	Zr	909.3	4957	1.9	1.10	99.04
23(Al_2O_3)	Au	355.9	760	8.4	0.86	87.0

Table 4.30: The Fitzpeaks photopeak results for the photopeaks of interest. The net area is the sum of the counts under the fitted photopeak subtracted by the background. The uncertainty is the statistical uncertainty calculated by Fitzpeaks. The χ^2_ν is the reduce chi-squared of the fit. The intensity information is from ENSDF [47].

4.2.3 Reaction Rate Results

Equation (2.15) is used to calculate the total reaction rate for each foil using the data from Tables 4.22, 4.30 and 4.31. These results are shown in Table 4.32. The uncertainty in the reaction rate includes the statistical uncertainty associated with the net counts and is recorded in Table 4.32.

Dataset	Foil	Realtime [s]	Livetime [s]	Time Since Irradiation [s]
14(^{56}Fe)	In	9092	9090	2410
14(^{56}Fe)	Ni	691327	691200	937963
14(^{56}Fe)	Al	141433	141404	11643
14(NaCl)	In	5188	5185	3603
14(NaCl)	Ni	345661	345600	364380
14(NaCl)	Al	92245	92228	10986
23(Al_2O_3)	In	18438	18436	91880
23(Al_2O_3)	Ni	593618	593533	865848
23(Al_2O_3)	Al	44499	44492	112812
23(Al_2O_3)	Zr	171980	171953	271825
23(Al_2O_3)	Au	243527	243492	443920

Table 4.31: Activation foil experimental information.

Dataset	Reaction	Reaction Rate [s^{-1}]
14(^{56}Fe)	^{115}In(n,n')	1180 ± 14
14(^{56}Fe)	^{58}Ni(n,p)	3.12 ± 0.07
14(^{56}Fe)	^{27}Al(n,a)	151 ± 5
14(NaCl)	^{115}In(n,n')	3683 ± 33
14(NaCl)	^{58}Ni(n,p)	9.80 ± 0.12
14(NaCl)	^{27}Al(n,a)	486 ± 8
23(Al_2O_3)	^{115}In(n,n')	2.76 ± 0.16
23(Al_2O_3)	^{58}Ni(n,p)	9.24 ± 0.10
23(Al_2O_3)	^{27}Al(n,a)	1281 ± 35
23(Al_2O_3)	^{90}Zr(n,2n)	1365 ± 26
23(Al_2O_3)	^{198}Au(n,2n)	126 ± 11

Table 4.32: Calculated reaction rates for all reactions for all datasets.

4.3 Maximum Entropy Unfolding

The Maximum Entropy Unfolding method described in Section 2.3 was used with the activation foil rates to modify the STOF-determined neutron flux spectrum. Before the unfold was done, the STOF-determined flux spectrum was adjusted as described in the following section.

4.3.1 Air Correction and Flux Extrapolation

The foil pack was placed in beam at the GENESIS target location, which was closer to the deuteron target than the location of the STOF spectrometer. One consequence of this is the flux per steradian incident at the STOF location will differ from that incident at the foil pack due to scattering through the air. To quantify this, the effect of air scatter on the STOF flux spectrum from Section 4.1.13, was calculated using MCNP6 [48]. A MCNP6 model consisting only of air between the STOF TC location and the foil pack location was created, see Fig. 4.53. MCNP was used to determine the differential flux with and without air scatter for each energy bin. The ratio as a function of energy was weighted by the measured spectrum and summed for each experiment. A python code was developed to read in the MCNP results and construct from the per bin results a full spectrum output matching a specified input shape (see Appendix E). The resulting air correction percentage for each dataset's spectrum is shown inFigs. 4.54 to 4.56.

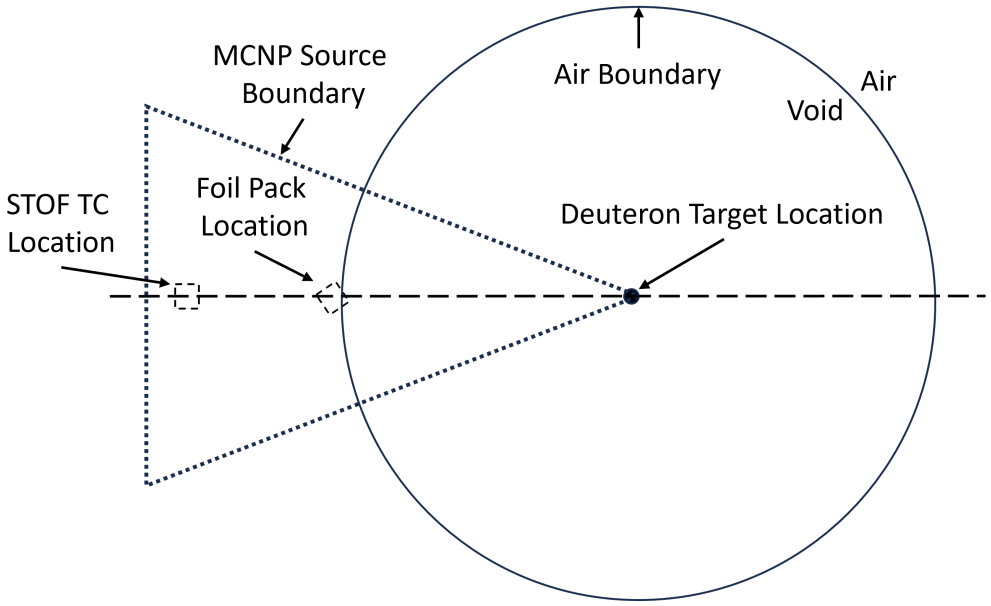

Figure 4.53: Diagram of the MCNP model used to determine the attenuation of neutrons through air between the STOF TC and the foil pack.

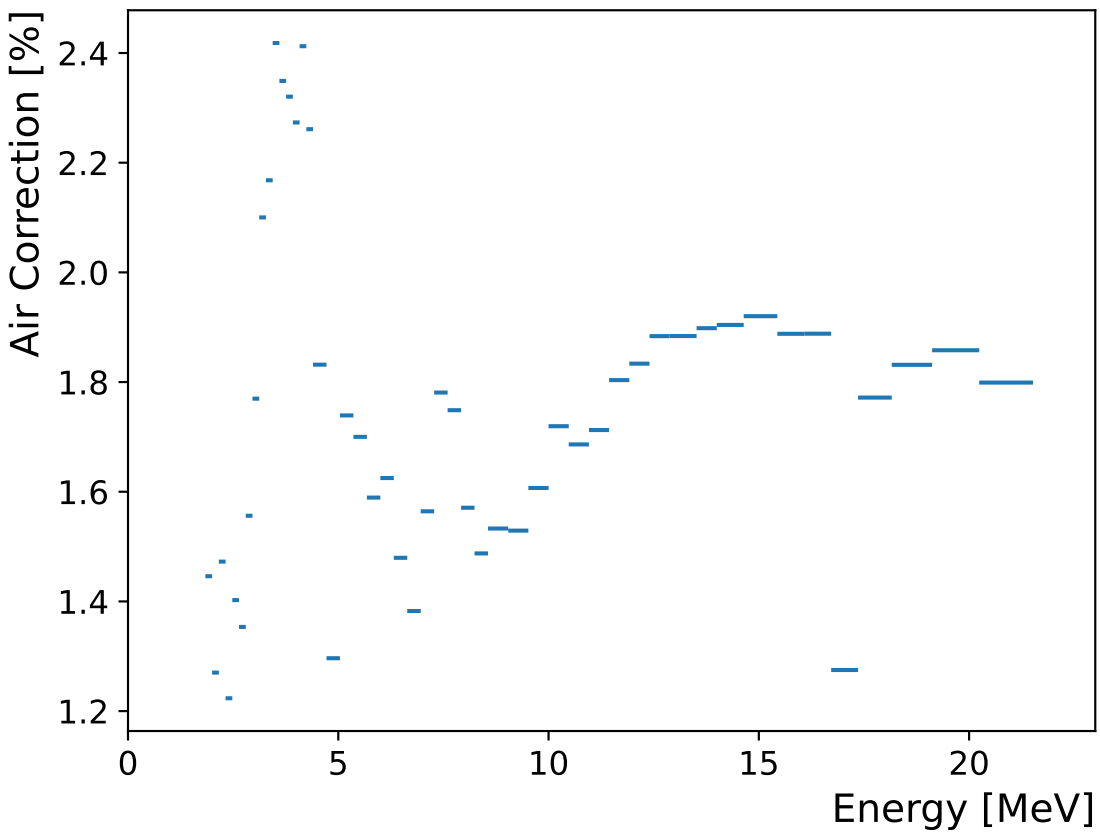

Figure 4.54: Percent that each bin for the final STOF flux for dataset 14(^{56}Fe) is changed to account for attenuation through the air between the foil pack location and the location of STOF.

In order to give the maximum entropy algorithm dynamic range below the scintillator detection threshold, each measured STOF spectrum is artificially linearly extrapolated down to 336 keV before application of the algorithm. The measured activation rates are for thresholdings reactions that extend down to 336 keV (see Fig. 4.38).

The extrapolation for each spectrum is done in two steps. First, the flux is extrapolated down to the lowest non-zero value using the slope between the two lowest measured energy bins. Second, it is linearly extrapolated from the new lowest value to 0 at 336 keV (see Appendix B for tabulated input flux).

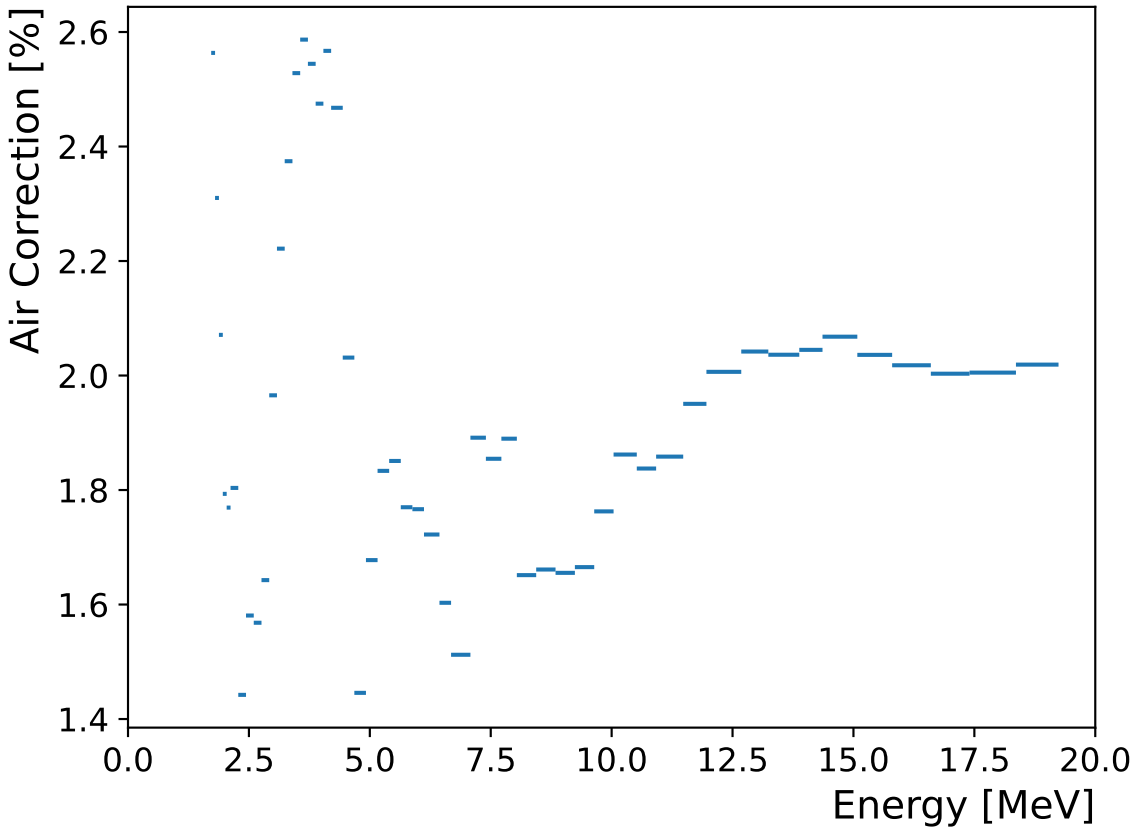

Figure 4.55: Percent that each bin for the final STOF flux for dataset 14(NaCl) is changed to account for attenuation through the air between the foil pack location and the location of STOF.

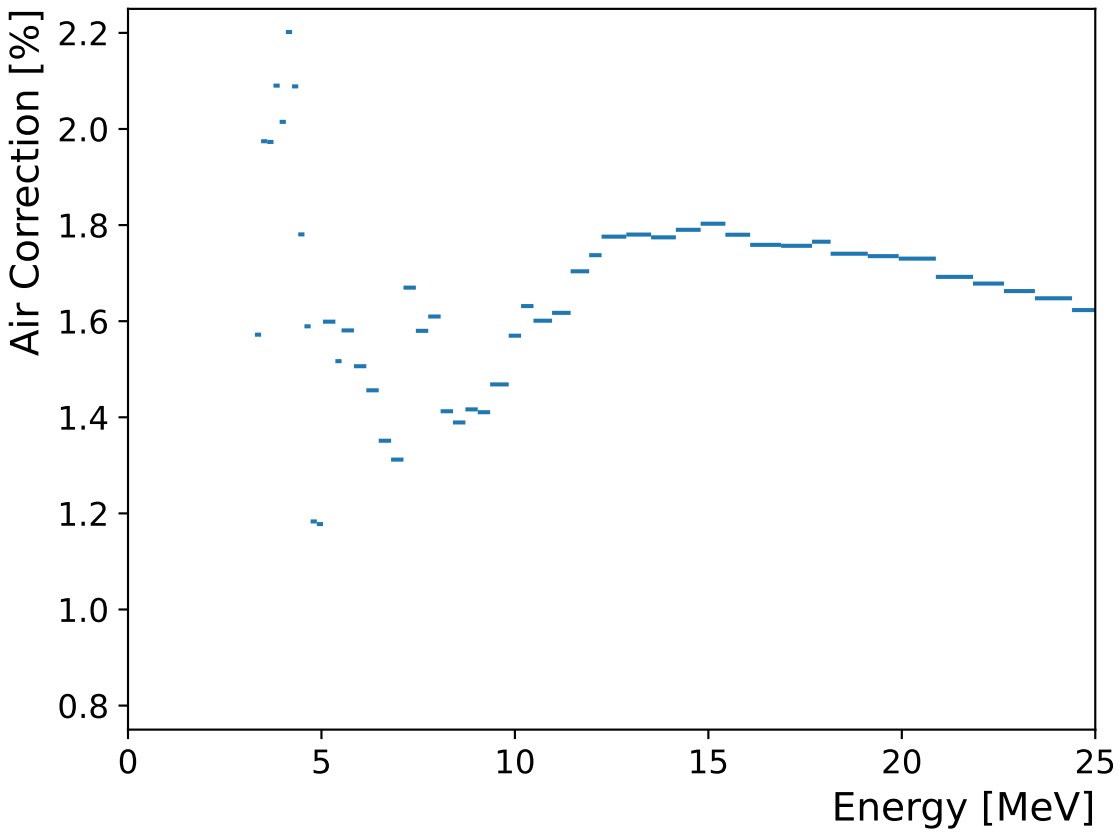

Figure 4.56: Percent that each bin for the final STOF flux for dataset 23(Al_2O_3) is changed to account for attenuation through the air between the foil pack location and the location of STOF.

4.3.2 Response Function Estimation

A response function for each reaction needs to be estimated to perform a spectral unfold. The response function, $\omega_{i,n}$, is of the form,

$$\omega_{i,n} = N_n \frac{\sigma_{i,n}\phi_{i,n}}{f_{i,n}} \tag{4.12}$$

where $\omega_{i,n}$ is derived in Section 2.3, i is each discretized energy bin, and n is each reaction. MCNP is used to account for the change in flux within the foil. An MCNP model of the foil pack was created as shown in Fig. 4.57.

However, using MCNP to estimate the response function is complicated by the fact that the unfolding is expected to alter the STOF incident flux estimate, thus changing the actual incident flux and changing the initially assumed response function. A data-driven iterative method was developed, where the STOF measurement is assumed initially as the incident flux and a spectrum unfold is performed. Then the process is repeated with the unfolded flux as the incident flux, calculating a new ω and new unfold. This process is repeated until the spectrum converges.

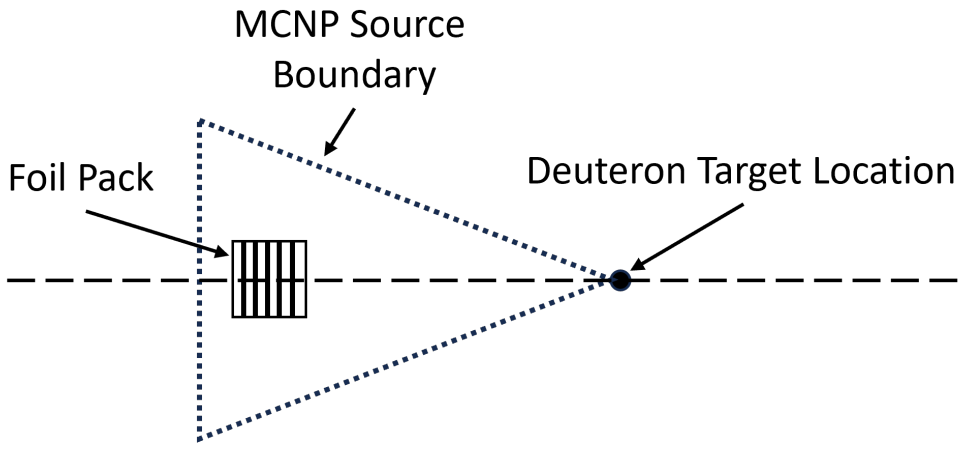

Figure 4.57: Diagram of the MCNP model used to determine the attenuation of neutrons through each foil.

4.3.3 Unfolding

The maximum entropy unfolding was implemented through python (see Appendix E). The function uses the Nelder-Mead [49] minimizing method. The plot for each iteration for each dataset is plotted in Figs. 4.58 to 4.60.

In the figures, the black line is the initial inputted spectrum and the green line is the final-unfolded spectrum for each dataset. For dataset 14(NaCl) and 23(Al_2O_3), the unfolding is reducing the measured spectrum nearly across the whole energy range. This is predominantly due to the difference in beam profile seen by the STOF TC and the foil pack. The magnitude of the neutron beam is expected to have a radial dependence, with the middle having a higher intensity than the edges. The neutron beam map of an independent experiment is shown in Fig. 4.61. The neutron beam for this dataset is representative of the described radial dependence, though collimator and beam tuning adjustments result in modest differences between experiments. The dataset of this beam map also used a 14 MeV deuteron beam from the 88-Inch Cyclotron into Cave 5 with the same collimator in place. As seen in the figure, the neutron intensity very quickly drops from its peak in the center to 30% of the peak at a 5 cm offset and then finally disappearing around a 10 cm offset. The exact position along the beam axis this map was measured at was not recorded, but it was taken downstream of the GENESIS target position. The solid angle coverage of STOF is much smaller since it is so much further away from the deuteron target than the foil pack. The STOF measurement is more representative of the higher magnitude beamline center than the foil pack that interacted with a larger beam spot. These unfolding results indicate that there is magnitude flux change between the beamline center and the beam edge upwards of 9.48% for the dataset 14(NaCl) neutron beam and upwards of 16.5% for the dataset 23(Al_2O_3) neutron beam.

The unfolding result for dataset 14(^{56}Fe) has a substantial energy bias where the lower end of the spectrum is increased while the higher end of the spectrum is not affected. To quantify the energy dependence of the unfolding, a variance is calculated between the ratios of the pre-unfolded spectrum and the unfolded spectrum for each bin and shown in Table 4.33. The lower this variance, the less the unfolding algorithm changes the shape of the spectrum. This variance only includes the non-extrapolated bins of the flux spectra.

Dataset	Variance
14(^{56}Fe)	0.00962
14(NaCl)	0.000670
23(Al_2O_3)	0.00608

Table 4.33: The variance of the per bin ratio between the pre-unfolded spectrum and the unfolded spectrum. The extrapolated bins are excluded.

Both dataset 14(^{56}Fe) and 14(NaCl) used the same 14 MeV deuteron beam. Differences between the two experimental configurations include slightly different STOF positions,

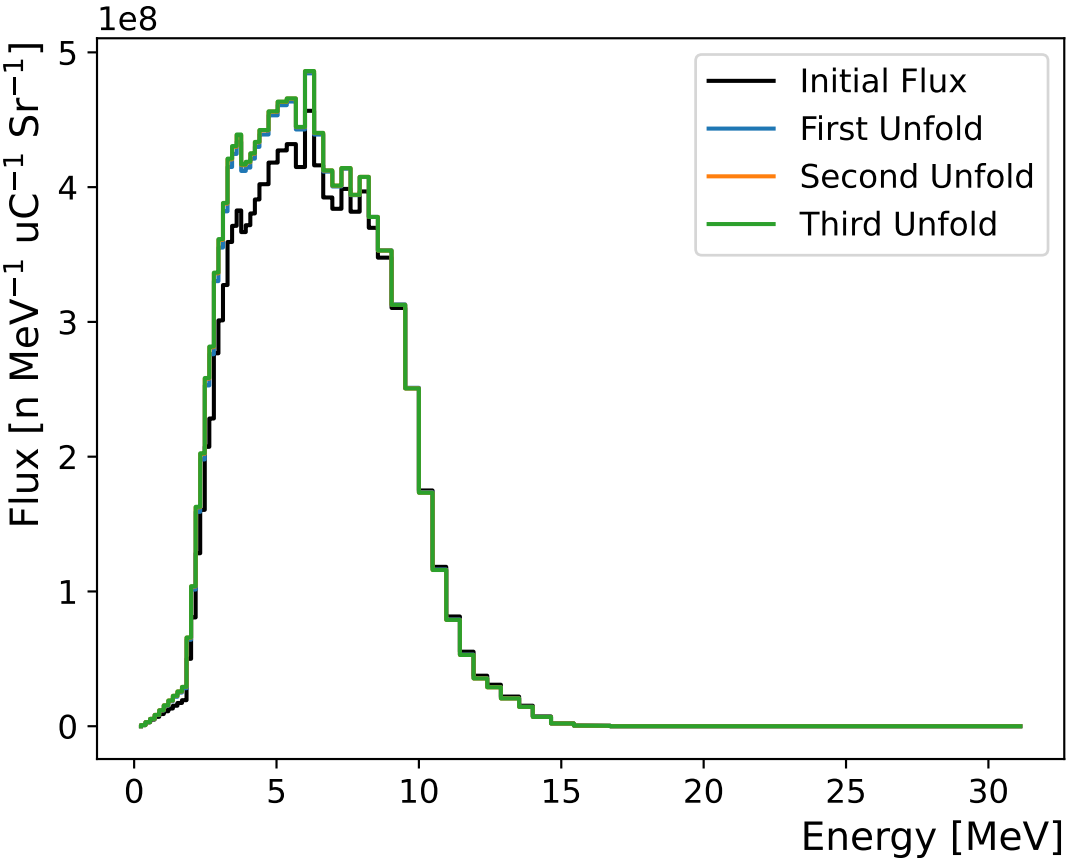

Figure 4.58: All unfolded flux spectra for dataset 14(^{56}Fe), including the initial input spectrum (black). The second iteration of the unfold (orange line) is hidden beneath the third iteration of the unfold (green line).

different detector biases, different collimator positions, and independent deuteron beam tuning. The different STOF positions are accounted for with high confidence. While no two beam tunes of the cyclotron are precisely the same, this is expected to result in small energy dependent differences between experiments, not the large deviations observed in the neutron spectrum. The collimator position for dataset 14(^{56}Fe) is believed to have been positioned partially blocking the beam, explaining the nearly 2x magnitude difference observed in the reaction rates and the STOF spectrum between the two datasets. However, this would not affect the variation in spectral shape of the flux that is observed in the unfolding and between the dataset 14(NaCl) unfolded spectrum and the dataset 14(^{56}Fe) unfolded spectrum. The difference in the detector biases are accounted for in the efficiency curve by incorporating the light yield calibration results found inSection 4.1.9. If the fitted LY parameter values are inaccurate, this could result in an energy-dependent effect on the spectrum. Notably, the

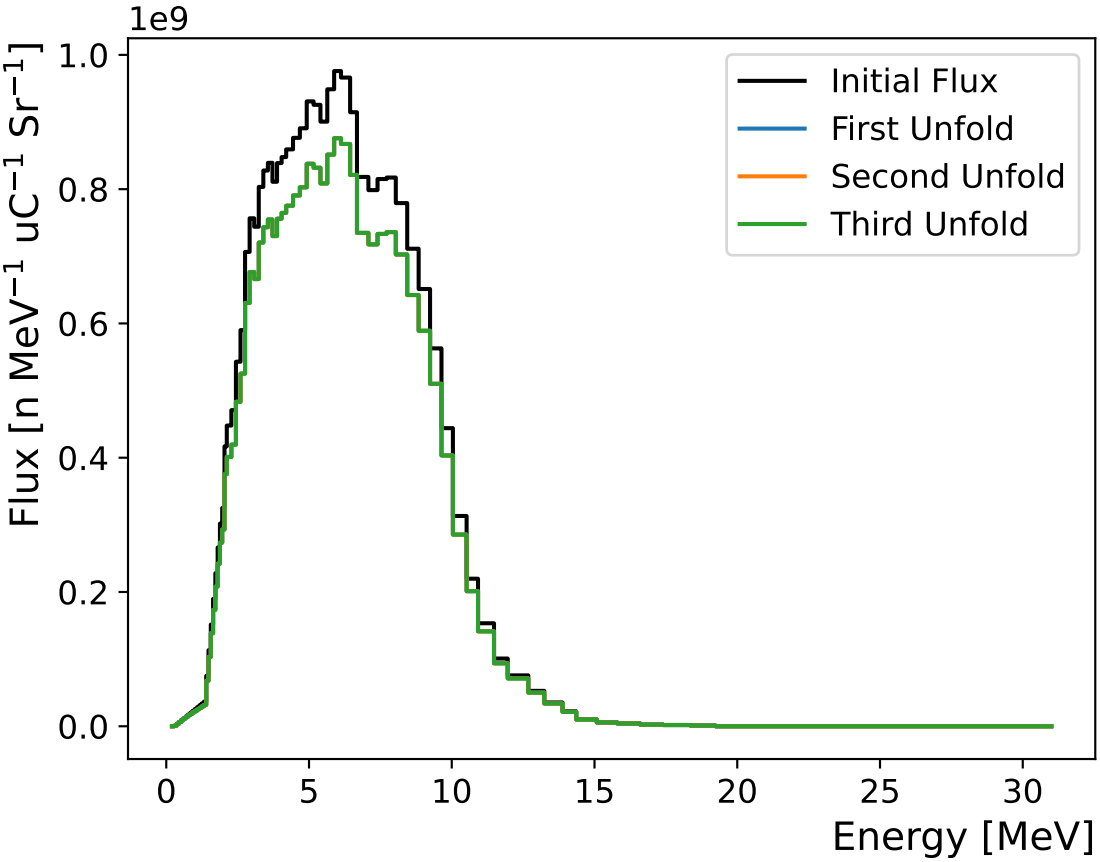

Figure 4.59: All unfolded flux spectra for dataset 14(NaCl), including the initial input spectrum (black). The first and second iteration of the unfold (blue and orange lines) are hidden beneath the third iteration of the unfold (green line).

confidence in the light yield calibration for dataset 14(^{56}Fe) is lower than that for dataset 14(NaCl) due to the significantly reduced observed neutron events. The total number of observed events is 2.65 times lower. In the next section, the effects of these light yield calibration parameters are investigated for dataset 14(^{56}Fe).

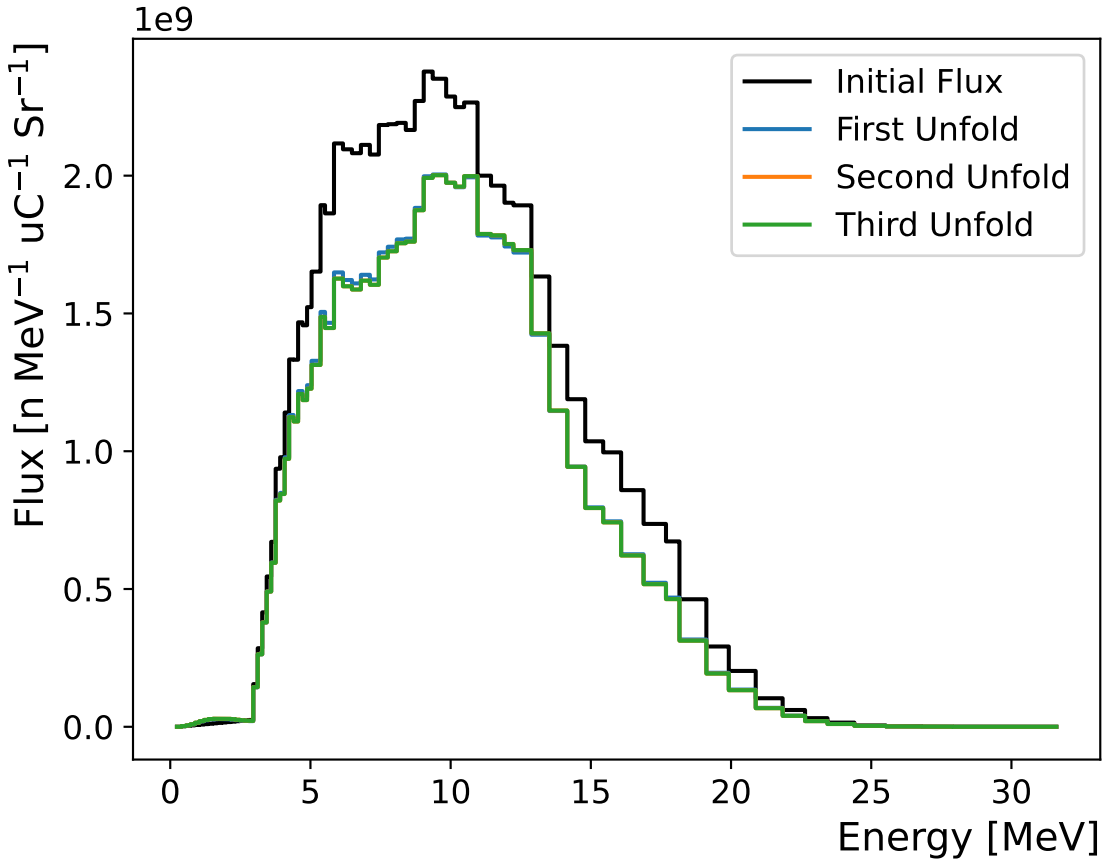

Figure 4.60: All unfolded flux spectra for dataset 23(Al_2O_3), including the initial input spectrum (black). The second iteration of the unfold (orange line) is hidden beneath the third iteration of the unfold (green line).

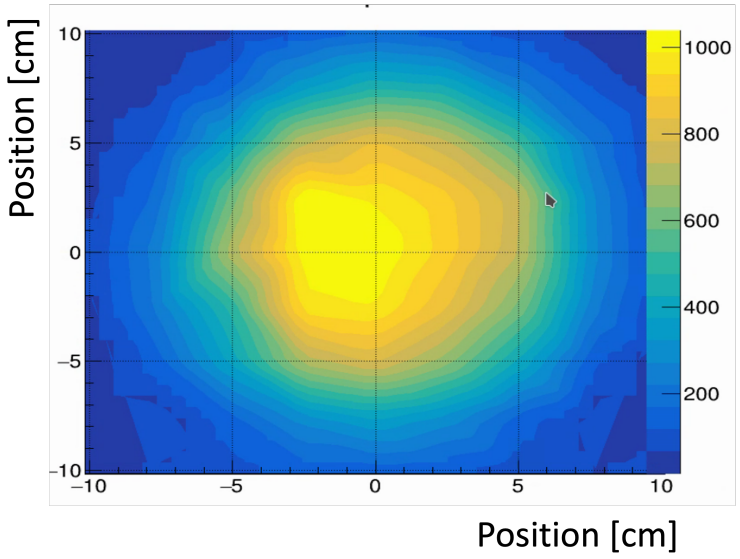

Figure 4.61: Example of a neutron beam spatial profile from a separate experiment also using a 14 MeV deuteron beam from the 88-Inch Cyclotron into Cave 5. The z-axis is the total number of counts. The x-axis and y-axis are the position in cm. The change in relative intensity from the peak at (0,0) to (5,0) is approximatly 30%.

4.3.4 Light Yield Calibration Parameter Affects For Dataset 14(^{56}Fe)

The light yield calibration is performed for each detector in the STOF configuration as described in Section 4.1.9, resulting in two parameters, a and b for a linear function to convert measured LY to MeVee. To test the validity of these parameters, they were varied, a new STOF spectrum was produced, and subsequently unfolded following the methodology previously discussed in this chapter. To quantify the energy dependence of the between the spectra, the variance, as described in the previous section, is calculated. The STOF SC light yield parameters were all changed jointly by the same percentage. The STOF TC light yield parameters were varied independently. The new values were changed by multiplying them by a factor, F. The tested factors and the resulting variances are listed in Table 4.34.

Detector(s)	F_a	F_b	Variance
-	-	-	0.00962
TC	0.664	-	0.0645
TC	1.33	-	0.0185
TC	-	0.0	0.00894
TC	-	2.0	0.0144
SCs	-	0.5	0.000350
SCs	-	2.0	0.0748
SCs	0.50	-	0.0973
SCs	0.55	-	0.0985
SCs	0.60	-	0.0783
SCs	0.65	-	0.0647
SCs	0.75	-	0.0438
SCs	1.10	-	0.00373
SCs	1.25	-	0.0000152
SCs	1.35	-	0.000130
SCs	1.50	-	0.00582

Table 4.34: Varied LY calibration parameters for alternative flux spectra for dataset 14(^{56}Fe). F_a is the factor that the a LY parameter is altered by. F_b is the factor that the b LY parameter is altered by. The "-" indicates that no factor was applied. The variance is the same as described in the previous section.

Of the new spectra, increasing the a for the SCs by 25% produces a spectrum with minimum change in spectral shape, this spectrum is shown in Fig. 4.62.

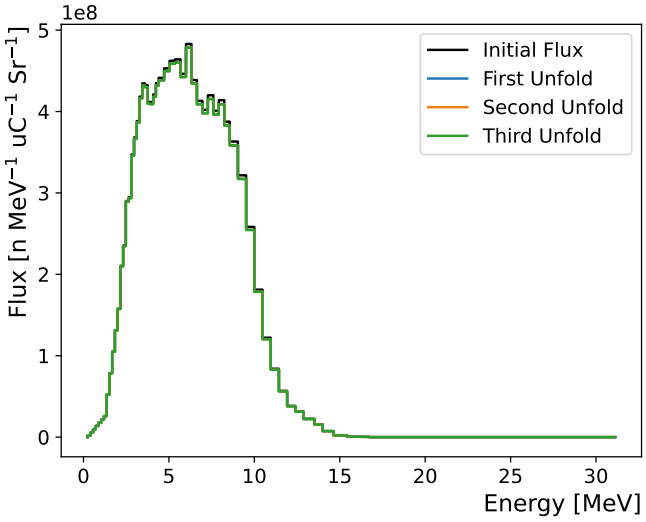

Figure 4.62: Unfolded flux spectra with adjusted LY parameters for 14(^{56}Fe). The blue and orange lines are hidden beneath the green line.

4.3.5 Integrated Flux from Activation Foils

The reaction rate as determined by each foil is compared to the reaction rate as estimated by the unfolded spectrum. The estimated reaction rate was calculated using Eq. (2.17) with the pre-unfolded spectrum and the unfolded spectrum as the incident spectrum. MCNP was used to account for the difference in flux within each foil. The ratio of the foil reaction rate to the STOF estimated reaction rate for both the unfolded and pre-unfolded spectra are tabulated in Table 4.35.

For dataset 14(NaCl), the ratios for the pre-unfolded spectrum for each foil are within 2% of each other. This agreement gives confidence in the shape of the pre-unfolded spectrum. As seen in the unfolded spectra ratios, the unfold is performing predominantly a magnitude change due to the beam profile as described in Section 4.3.3. The spread also changes from within 2% to within 1.5%. This is due to the unfolding performing a small energy-dependent spectral adjustment. This spectrum shape change can be due to possibilities. First, the simulated efficiency spectrum is reliant on an assumed linear LY calibration. While the LY calibration for fast neutrons is approximately linear, it is not actually linear and so small deviations in spectral shape would be anticipated. Second, The energy resolution of TOF spectrometers increase with increasing energy. This results in a smearing of the neutron events biased against the high energy side. Both of these are expected to result in a small energy-dependent spectral adjustment, such as what is observed with the unfolded spectrum.

For dataset 23(Al_2O_3), The Al foil ratio is a clear outlier compared to the other ratios. This is possibly due to the fitted LY calibration parameters being less accurate than those for dataset 14(NaCl). However, the unfolding algorithm weights the inputs that are more in

Dataset	Foil	Ratio (pre-unfold)	Ratio (unfolded)
14(^{56}Fe)	In	1.122	1.015
14(^{56}Fe)	Ni	1.042	0.974
14(^{56}Fe)	Al	1.022	1.004
14(^{56}Fe)(adjusted)	In	1.023	1.000
14(^{56}Fe)(adjusted)	Ni	0.977	0.970
14(^{56}Fe)(adjusted)	Al	0.985	0.982
14(NaCl)	In	0.915	0.985
14(NaCl)	Ni	0.923	1.000
14(NaCl)	Al	0.935	0.999
23(Al_2O_3)	In	0.852	0.992
23(Al_2O_3)	Ni	0.781	0.996
23(Al_2O_3)	Al	0.96	1.11
23(Al_2O_3)	Au	0.86	1.035
23(Al_2O_3)	Zr	0.896	1.00

Table 4.35: The ratio of the reaction rate measured by the activation analysis divided by the STOF estimated reaction rate. The 14(^{56}Fe) (adjusted) dataset incorporates the spectrum from Fig. 4.62

agreement with each other, as can be seen in the unfolded spectra ratios where the spectrum is changed to prioritize agreement between the non-outliers over the one outlier. Excluding the Al ratio, the spread of the ratios changes from 11.5% in the pre-unfolded spectra to 4.3% in the unfolded spectra.

For dataset 14(^{56}Fe), there is a clear outlier in the pre-unfolded ratios with the In foil. However, unlike the unfold with the dataset 23(Al_2O_3) spectrum, this unfolded spectrum results in an unrealistic shape change shown in Section 4.3.3, prompting an investigation into changing the fitted LY parameters. The ratios for this adjusted spectrum bring all three into better agreement with each other, with only a spread of 3.8%. The adjusted spectrum's unfolded ratio range is reduced to 3% which is also lower than the spread in the ratios for the unfolded non-adjusted spectrum of 4.1%. The unfolding algorithm was not able to account for the outlier in dataset 14(^{56}Fe) realistically, however, it was able to do so in dataset 23(Al_2O_3). This is likely due to the increased number of monitor reactions. The algorithm was able to realistically deal with a single outlier out of 5 data points, but not with a single outlier out of 3 data points.

Chapter 5

Conclusion

5.1 Discussion, Summary, and Future Work

Development and implementation of a neutron spectrometer for independent neutron flux measurements in the MeV energy range is needed for numerous applications. As is seen between the datasets 14(^{56}Fe) and 14(NaCl) (see Fig. 5.1), changes in the experimental environment (e.g. collimator positioning and accelerator tuning) can result in significant changes to the total flux as observed in Fig. 5.1, even when the deuteron beam energy remains the same. Comparing the dataset 14(^{56}Fe) spectrum to the dataset 14(NaCl) spectrum, the limiting factor for the STOF accuracy is shown to be the determination of the efficiency, specifically for achieving confident LY calibration parameters. The dataset 14(NaCl) had 2.6 times the amount of data than in dataset 14(^{56}Fe), resulting in a less accurate estimation of the LY calibration parameters for dataset 14(^{56}Fe). This inaccuracy is exhibited in the ratio between the measured reaction rates and the estimated reaction rates, shown in Table 4.35, and the energy dependent unfold adjustment, shown in Fig. 4.58. The application of the Maximum Entropy Unfolding method to the analysis of activation foil data, crucially, can mitigate these limitations. The experimentally-driven investigation into the LY calibration parameter optimization produced a spectrum that fits the measured reaction rates. The investigation is a proof of concept that a methodology to minimize the individual LY calibration parameters for each detector relative to the variance described in Section 4.3.4 is worth pursuing for future work. This would allow for high-confident LY calibration parameters to be produced when neutron data is limited.

Additionally, the Maximum Entropy Unfolding method is capable of correcting a spectrum with some discrepant data, e.g. dataset 23(Al_2O_3) shown in Fig. 5.1. The unfolding can achieve this when there are enough activation reactions measured over a sufficient energy range. The spread of the ratio of the measured and estimated reaction rates for dataset 23(Al_2O_3), listed in Table 4.35, is larger than for dataset 14(NaCl). Notably, the estimated reaction rate for the aluminum foil is a clear outlier. The broader range of measured data available to the unfolding algorithm allows a more physically-justified, self-consistent spectral

adjustment and identification of outliers. Unexpected delays in the ability to count the foils resulted in lower statistics ($\tilde{3}$% error) for the aluminum foil counting and though not on order of 11%, the aluminum activity was not as trustworthy as in the other datasets.

The STOF-determined spectrum for all three measurements have low energy cut off at 2.0 MeV, 1.8 MeV, and 3.4 MeV for datasets 14(^{56}Fe), 14(NaCl), and 23(Al_2O_3) respectively. The first 2-3 bins for each spectrum were discarded due to the bins unrealistically increasing. The timing resolution of the spectrometer translates to an energy uncertainty greater than the chosen bin widths. This primarily results in a smoothing of bin-scale features in most of the spectrum where there are sufficient statistics and the efficiency curve is not rapidly changing. However, the high sensitivity near the threshold is expected to cause the extreme discontinuities observed, due to misattributed neutron flux in bins where the model predicts near-zero efficiency.

The lack of detector response at low neutron energy prevents the capability to accurately evaluate rates of reactions with lower thresholds. The unfolding algorithm provides some additional insight into the unmeasured low-energy portion of the neutron spectrum. A simplistic linear extrapolation of the measured spectrum provides the unfolding algorithm the degrees of freedom to attempt the unfolding down to 0.336 MeV (the lowest threshold for the measured reactions). This resulted in a successful spectrum unfold of the dataset 14(NaCl) and 23(Al_2O_3) and an initial failure for dataset 14(^{56}Fe). The success for dataset 14(NaCl) compared to dataset 14(^{56}Fe) was due to the larger number of measured events, resulting in a statistically superior spectrum and higher confidence in the efficiency curve. The success for dataset 23(Al_2O_3) was primarily due to a larger number of measured reaction rates (5 instead of 3), better constraining the unfolding algorithm. Importantly, the shape of the low-energy extrapolated regime of these spectrums should not be taken at face value. This extrapolated regime of the spectrum predominantly affects the indium reaction, meaning that the unfolding algorithm only has one degree of freedom to adjust the spectrum in the energy range up to the next reaction's threshold. Instead, only the total magnitude should be considered when interpreting these results. Namely, while there may be some low-energy neutrons present in this part of the spectrum, the total neutron contribution is very small compared to the high energy regime.

While the unmeasured low energy regime may be small for the thick target deuteron breakup neutron spectra considered in this work, there is still considerable need to measure it. This can be achieved with the STOF spectrometer by increasing the gain to measure the low energy neutrons at the loss of the high-energy neutrons, followed by a measurement in a low-gain mode to measure the high-energy neutrons. Both spectra can be combined to create a broad-energy neutron spectrum. Alternatively, use of borated or lithiated scattering cells could also be used to measure lower energy. Such a measurement would be even more important if a beryllium breakup target is reimplemented at the GENESIS facility. The neutron flux from an uncollimated 16 MeV deuteron beam incident on a beryllium breakup target was previously measured at the 88-Inch Cyclotron by Harrig [6]. This spectrum, reproduced in Fig. 5.1, shows a much larger low-energy neutron flux compared to the carbon target results. Although the beryllium spectrum in Fig. 5.1 exhibits a significantly greater

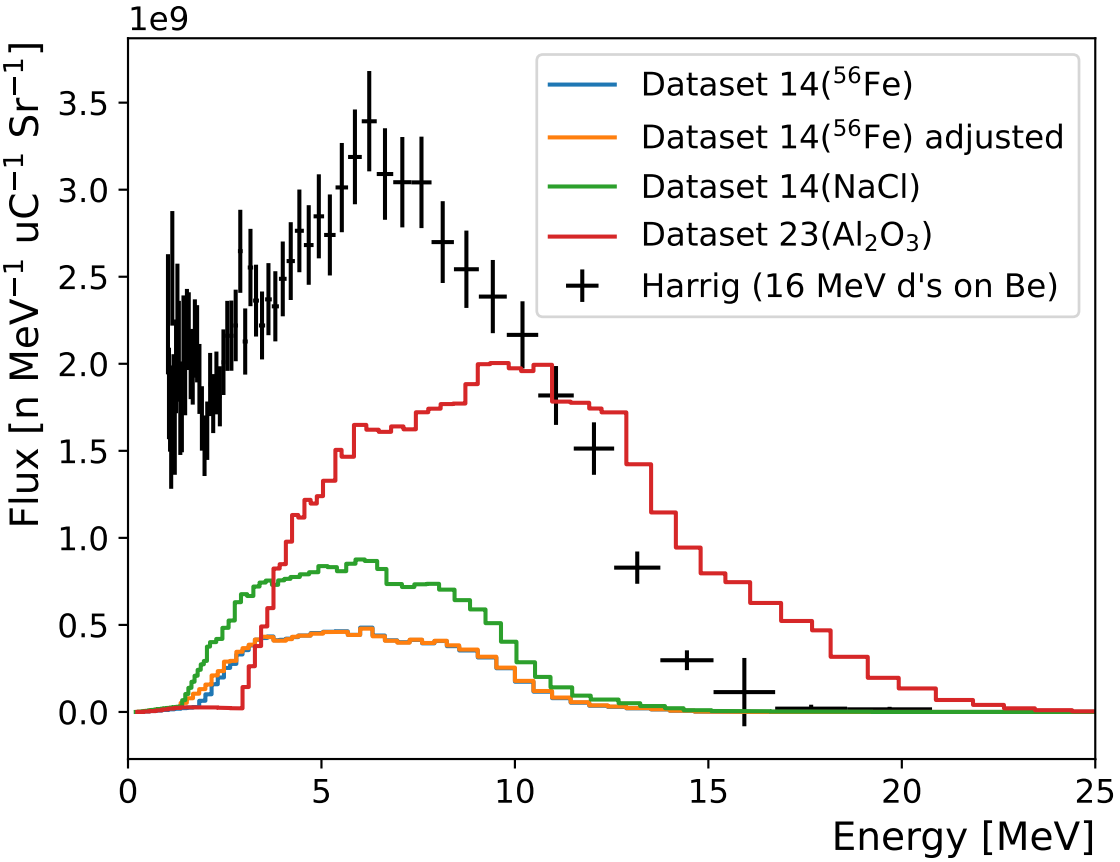

Figure 5.1: Unfolded flux results for all datasets compared to the flux produced from 16 MeV deuterons on a beryllium target from Harrig [6].

total flux than the measurements in this report, this is primarily due to losses in collimation and, to a lesser extent, the higher incident deuteron energy. Similar measurements [50] indicate a more modest increase of about 35% at the same deuteron energy in the absence of collimation. While the STOF spectrometer circumvents frame overlap, as described in Section 1.2.2, the cross section measurements done by the GENESIS array cannot. While beryllium targets produce neutrons from equivalent deuteron beams, more are produced at low energies, which (depending on the specific measurement) may lead to more ambiguous results. The STOF spectrometer, in conjunction with activation foils and spectral unfolding techniques, provides a powerful, high-efficiency capability to noninvasively monitor neutron spectra at experimental facilities like GENESIS where traditional time-of-flight techniques are not possible.

Bibliography

[1] M Kireeff Covo et al. "The 88-Inch Cyclotron: A one-stop facility for electronics radiation and detector testing." *Measurement* 127 (2018), pp. 580–587.

[2] JM Gordon et al. "GENESIS: Gamma Energy Neutron Energy Spectrometer for Inelastic Scattering." *Nuclear Instruments and Methods in Physics Research Section A: Accelerators, Spectrometers, Detectors and Associated Equipment* 1061 (2024), p. 169120.

[3] Jonathan T Morrell et al. "Secondary neutron production from thick target deuteron breakup." *Physical Review C* 108.2 (2023), p. 024616.

[4] DL Bleuel et al. "Characterization of a tunable quasi-monoenergetic neutron beam from deuteron breakup." *Nuclear Instruments and Methods in Physics Research Section B: Beam Interactions with Materials and Atoms* 261.1-2 (2007), pp. 974–979.

[5] J Bailey et al. "Selection and measurement of RF phase width of the K1200 Cyclotron beam." *Proc. Thirteenth International Conference on Cyclotrons and their Applications,(eds. G. Dutto and MK Craddock)*. Vol. 431.

[6] KP Harrig et al. "Neutron spectroscopy for pulsed beams with frame overlap using a double time-of-flight technique." *Nuclear Instruments and Methods in Physics Research Section A: Accelerators, Spectrometers, Detectors and Associated Equipment* 877 (2018), pp. 359–366.

[7] Josh A Brown. "A Double Time of Flight Method For Measuring Proton Light Yield." PhD thesis. University of California, Berkeley, 2017.

[8] E Barnard et al. "Time-of-flight measurements of neutron spectra from the fission of U235, U238 and Pu239." *Nuclear Physics* 71.1 (1965), pp. 228–240.

[9] Zs Elter et al. "Performance investigation of the pulse and Campbelling modes of a fission chamber using a Poisson pulse train simulation code." *Nuclear Instruments and Methods in Physics Research Section A: Accelerators, Spectrometers, Detectors and Associated Equipment* 774 (2015), pp. 60–67.

[10] DB Gayther. "International intercomparison of fast neutron fluence-rate measurements using fission chamber transfer instruments." *Metrologia* 27.4 (1990), p. 221.

[11] Matthew Edgell Gooden et al. "Energy dependence of fission product yields from 235U, 238U and 239Pu for incident neutron energies between 0.5 and 14.8 MeV." *Nuclear Data Sheets* 131 (2016), pp. 319–356.

[12] Robert C Haight et al. "The LANL/LLNL prompt fission neutron spectrum program at LANSCE and approach to uncertainties." *Nuclear Data Sheets* 123 (2015), pp. 130–134.

[13] S Noda et al. "Prompt fission neutron spectra from fission induced by 1 to 8 MeV neutrons on U 235 and Pu 239 using the double time-of-flight technique." *Physical Review C* 83.3 (2011), p. 034604.

[14] TN Taddeucci et al. "Multiple-scattering corrections to measurements of the prompt fission neutron spectrum." *Nuclear Data Sheets* 123 (2015), pp. 135–139.

[15] CY Wu et al. *Low-mass fission detector for the fission neutron spectrum measurement.* Tech. rep. Lawrence Livermore National Lab.(LLNL), Livermore, CA (United States), 2010.

[16] A Donzella et al. "A proton recoil telescope for neutron spectroscopy." *Nuclear Instruments and Methods in Physics Research Section A: Accelerators, Spectrometers, Detectors and Associated Equipment* 613.1 (2010), pp. 58–64.

[17] L Harris Jr, Glenn F Knoll, and John Swinton King. "Proton-recoil spectrometer for fast neutron spectra" (1965).

[18] P Marini et al. "Systematic investigation of background sources in neutron flux measurements with a proton-recoil silicon detector." *Nuclear Instruments and Methods in Physics Research Section A: Accelerators, Spectrometers, Detectors and Associated Equipment* 841 (2017), pp. 56–64.

[19] Yoshiaki Shikaze et al. "Development of highly efficient proton recoil counter telescope for absolute measurement of neutron fluences in quasi-monoenergetic neutron calibration fields of high energy." *Nuclear Instruments and Methods in Physics Research Section A: Accelerators, Spectrometers, Detectors and Associated Equipment* 615.2 (2010), pp. 211–219.

[20] Marcel Reginatto. "Overview of spectral unfolding techniques and uncertainty estimation." *Radiation Measurements* 45.10 (2010), pp. 1323–1329.

[21] Z Bell et al. "Materials Selection for a High Temperature Fission Chamber." *ORNL/LTR-2012/331, Oak Ridge National Laboratory* (2012).

[22] RL Van Hemert et al. "A new detector for keV neutrons." *Nuclear Instruments and Methods* 89 (1970), pp. 263–275.

[23] J Taforeau et al. "A new recoil proton telescope for characterisation of energy and fluence of fast neutron fields." *Journal of Instrumentation* 7.04 (2012), p. C04015.

[24] Keisuke Asai et al. "Neutron spectrometer for DD/DT burning ratio measurement in fusion experimental reactor." *Journal of nuclear science and technology* 43.4 (2006), pp. 320–324.

[25] John Betteley Birks. "Scintillations from organic crystals: specific fluorescence and relative response to different radiations." *Proceedings of the Physical Society. Section A* 64.10 (1951), p. 874.

[26] CN Chou. "The nature of the saturation effect of fluorescent scintillators." *Physical Review* 87.5 (1952), p. 904.

[27] J Hong et al. "The scintillation efficiency of carbon and hydrogen recoils in an organic liquid scintillator for dark matter searches." *Astroparticle Physics* 16.3 (2002), pp. 333–338.

[28] S Yoshida et al. "Light output response of KamLAND liquid scintillator for protons and 12C nuclei." *Nuclear Instruments and Methods in Physics Research Section A: Accelerators, Spectrometers, Detectors and Associated Equipment* 622.3 (2010), pp. 574–582.

[29] Claude E Shannon. "A mathematical theory of communication." *The Bell system technical journal* 27.3 (1948), pp. 379–423.

[30] *Neutron/Gamma PSD Liquid Scintillator EJ-301,EJ-309*. Available at `https://eljentechnology.com/products/liquid-scintillators/ej-301-ej-309`. Eljen Technology. Sweetwater, Texas, USA, July 2021.

[31] Hamamatsu Photonics K.K. *Photomultiplier tube assembly H6533*. URL: `https://hep.hamamatsu.com/eu/en/products/H65331.html` (visited on 12/30/2023).

[32] *Leica Disto S9010*. Available at `https://shop.leica-geosystems.com/sites/default/files/2020-12/S910_808167d_en.pdf`. Leica Geosystems AG. Heerbrugg, Switzerland, 2020.

[33] *803x Series 8-16 Ch. Programmable HV Power Supplies*. 10th. Available at `https://www.caen.it/products/r8033/`. CAEN S.p.A. Viareggio, Italy, Dec. 2022.

[34] John Smith and Jane Doe. *DT5730/DT5725 User Manual 8-Channel 14-bit 500/250 MS/s Waveform Digitizer*. 8th. Available at `https://www.caen.it/support-services/documentation-area/`. CAEN S.p.A. Viareggio, Italy, Mar. 2023.

[35] *User Manual UM430 725 and 730 DPP-PSD Register Description and Data Format*. 6th. Available at `https://www.caen.it/products/dpp-psd/`. CAEN S.p.A. Viareggio, Italy, Apr. 2020.

[36] *User Manual UM5960 CoMPASS Multiparamtric DAQ Software for Physics Applications*. 12th. Available at `https://www.caen.it/support-services/documentation-area/`. CAEN S.p.A. Viareggio, Italy, Aug. 2020.

[37] Ilka Antcheva et al. "ROOT—A C++ framework for petabyte data storage, statistical analysis and visualization." *Computer Physics Communications* 182.6 (2011), pp. 1384–1385.

[38] *GEM Series Coaxial HPGe Detector Product Configuration Guide*. Available at https://www.ortec-online.com/-/media/ametekortec/brochures/g/gem.pdf?la=en&revision=ae7caf09-b98c-4a33-a092-b43edb472666. ORTEC AMETEK. Oak Ridge, TN, USA.

[39] ORTEC. *GammaVision Maestro-PRO Gamma-Ray Spectrum Analysis and MCA Emulators for Microsoft Windows 7, 8.1, and 10 Professional*. English. Version M. ORTEC. 2020.

[40] Jim Fitzgerald. *FitzPeaks Gamma Analysis and Calibration Software*. Oct. 2016. URL: https://www.jimfitz.co.uk/fitzpeak.htm.

[41] Bay Area Neutron Group. *NSD-RootScripts Repository*. Apr. 2024. URL: https://bang.berkeley.edu/detection-library-license/.

[42] Glenn F Knoll. *Radiation detection and measurement*. John Wiley & Sons, 2010.

[43] G Dietze and H Klein. "Gamma-calibration of NE 213 scintillation counters." *Nuclear Instruments and Methods in Physics Research* 193.3 (1982), pp. 549–556.

[44] Thibault A Laplace et al. "Modeling ionization quenching in organic scintillators." *Materials Advances* 3.14 (2022), pp. 5871–5881.

[45] A. Trkov et al. "IRDFF-II: A New Neutron Metrology Library." *Nuclear Data Sheets* 163 (2020), pp. 1–108. ISSN: 0090-3752. DOI: https://doi.org/10.1016/j.nds.2019.12.001. URL: https://www.sciencedirect.com/science/article/pii/S0090375219300687.

[46] DL Bleuel et al. "Precision measurement of relative γ-ray intensities from the decay of 61Cu." *Applied Radiation and Isotopes* 170 (2021), p. 109625.

[47] *From ENSDF database as of March 20, 2024. Version available at http://www.nndc.bnl.gov/ensarchivals/.*

[48] Christopher John Werner et al. *MCNP User's Manual Code Version 6.2*. Tech. rep. LA-UR-17-29981. Los Alamos, NM, USA: Los Alamos National Laboratory, Oct. 2017. URL: http://permalink.lanl.gov/object/tr?what=info:lanl-repo/lareport/LA-UR-17-29981.

[49] J. A. Nelder and R. Mead. "A Simplex Method for Function Minimization." *The Computer Journal* 7.4 (Jan. 1965), pp. 308–313. ISSN: 0010-4620. DOI: 10.1093/comjnl/7.4.308. eprint: https://academic.oup.com/comjnl/article-pdf/7/4/308/1013182/7-4-308.pdf. URL: https://doi.org/10.1093/comjnl/7.4.308.

[50] Keith A Weaver. *Spectra of neutrons from deuteron bombardment of light nuclei*. Tech. rep. California Univ., 1973.

Appendix A

STOF-Determined Neutron Flux

A.1 Dataset 14(^{56}Fe) Not Adjusted

Lower Bin Edge [MeV]	Upper Bin Edge [MeV]	Flux [n MeV^{-1} uC^{-1} Sr^{-1}]	Flux Error [±]
0.24	0.40	0.000e+00	0.000e+00
0.40	0.56	0.000e+00	0.000e+00
0.56	0.72	0.000e+00	0.000e+00
0.72	0.88	0.000e+00	0.000e+00
0.88	1.04	0.000e+00	0.000e+00
1.04	1.20	0.000e+00	0.000e+00
1.20	1.36	0.000e+00	0.000e+00
1.36	1.52	0.000e+00	0.000e+00
1.52	1.68	5.172e+09	5.193e+09
1.68	1.84	6.783e+07	4.569e+06
1.84	2.00	4.930e+07	1.695e+06
2.00	2.16	7.970e+07	2.170e+06
2.16	2.32	1.265e+08	3.176e+06
2.32	2.48	1.586e+08	3.747e+06
2.48	2.64	2.044e+08	4.875e+06
2.64	2.80	2.253e+08	5.161e+06
2.80	2.96	2.725e+08	6.249e+06
2.96	3.12	2.959e+08	6.641e+06
3.12	3.28	3.206e+08	7.223e+06
3.28	3.44	3.517e+08	8.123e+06
3.44	3.60	3.625e+08	8.436e+06
3.60	3.76	3.739e+08	8.828e+06
3.76	3.92	3.583e+08	8.290e+06
3.92	4.08	3.635e+08	8.502e+06
4.08	4.24	3.715e+08	8.741e+06
4.24	4.40	3.822e+08	9.145e+06
4.40	4.72	3.949e+08	6.753e+06
4.72	5.04	4.129e+08	7.115e+06
5.04	5.36	4.199e+08	7.352e+06
5.36	5.68	4.247e+08	7.636e+06
5.68	6.00	4.084e+08	7.338e+06
6.00	6.32	4.493e+08	8.650e+06
6.32	6.64	4.101e+08	7.858e+06
6.64	6.96	3.870e+08	7.586e+06
6.96	7.28	3.780e+08	7.646e+06
7.28	7.60	3.917e+08	8.304e+06
7.60	7.92	3.752e+08	7.983e+06
7.92	8.24	3.907e+08	8.705e+06
8.24	8.56	3.644e+08	8.144e+06
8.56	9.04	3.424e+08	6.332e+06

Lower Bin Edge [MeV]	Upper Bin Edge [MeV]	Flux [n MeV^{-1} uC^{-1} Sr^{-1}]	Flux Error [±]
9.04	9.52	3.057e+08	5.807e+06
9.52	10.00	2.469e+08	4.845e+06
10.00	10.48	1.720e+08	3.471e+06
10.48	10.96	1.163e+08	2.492e+06
10.96	11.44	8.005e+07	1.838e+06
11.44	11.92	5.432e+07	1.346e+06
11.92	12.40	3.681e+07	9.741e+05
12.40	12.88	3.023e+07	8.687e+05
12.88	13.52	2.159e+07	6.005e+05
13.52	14.00	1.493e+07	5.645e+05
14.00	14.64	7.105e+06	3.054e+05
14.64	15.44	2.076e+06	1.483e+05
15.44	16.08	4.828e+05	1.056e+05
16.08	16.72	3.006e+05	9.634e+04
16.72	17.36	6.658e+03	7.722e+04
17.36	18.16	5.686e+04	7.305e+04
18.16	19.12	1.229e+05	6.047e+04
19.12	20.24	5.744e+04	5.101e+04
20.24	21.52	-2.983e+04	4.783e+04
21.52	22.64	5.047e+04	5.656e+04
22.64	24.08	-9.587e+03	4.553e+04
24.08	25.52	1.774e+04	4.418e+04
25.52	26.64	3.356e+04	8.222e+04
26.64	27.92	1.511e+05	1.606e+05
27.92	29.68	1.418e+05	4.375e+05
29.68	31.12	-1.035e+06	5.072e+05

Table A.1: STOF-determined neutron flux for dataset 14(^{56}Fe).

A.2 Dataset 14(^{56}Fe) Adjusted

Lower Bin Edge [MeV]	Upper Bin Edge [MeV]	Flux [n MeV^{-1} uC^{-1} Sr^{-1}]	Flux Error [±]
0.24	0.40	0.000e+00	0.000e+00
0.40	0.56	0.000e+00	0.000e+00
0.56	0.72	0.000e+00	0.000e+00
0.72	0.88	0.000e+00	0.000e+00
0.88	1.04	0.000e+00	0.000e+00
1.04	1.20	0.000e+00	0.000e+00
1.20	1.36	0.000e+00	0.000e+00
1.36	1.52	0.000e+00	0.000e+00
1.52	1.68	0.000e+00	0.000e+00
1.68	1.84	3.436e+08	4.571e+07
1.84	2.00	1.291e+08	6.434e+06
2.00	2.16	1.555e+08	5.595e+06
2.16	2.32	2.071e+08	6.466e+06
2.32	2.48	2.324e+08	6.521e+06
2.48	2.64	2.859e+08	7.956e+06
2.64	2.80	2.906e+08	7.488e+06
2.80	2.96	3.417e+08	8.715e+06
2.96	3.12	3.617e+08	8.922e+06
3.12	3.28	3.802e+08	9.283e+06
3.28	3.44	4.094e+08	1.016e+07
3.44	3.60	4.242e+08	1.064e+07
3.60	3.76	4.223e+08	1.056e+07
3.76	3.92	4.025e+08	9.840e+06
3.92	4.08	4.024e+08	9.877e+06
4.08	4.24	4.109e+08	1.014e+07
4.24	4.40	4.251e+08	1.070e+07
4.40	4.72	4.335e+08	7.747e+06
4.72	5.04	4.473e+08	8.007e+06
5.04	5.36	4.544e+08	8.262e+06
5.36	5.68	4.564e+08	8.491e+06
5.68	6.00	4.393e+08	8.172e+06
6.00	6.32	4.753e+08	9.398e+06
6.32	6.64	4.323e+08	8.494e+06
6.64	6.96	4.075e+08	8.186e+06
6.96	7.28	3.960e+08	8.187e+06
7.28	7.60	4.127e+08	8.968e+06
7.60	7.92	3.939e+08	8.579e+06
7.92	8.24	4.076e+08	9.267e+06
8.24	8.56	3.819e+08	8.727e+06
8.56	9.04	3.577e+08	6.751e+06

Lower Bin Edge [MeV]	Upper Bin Edge [MeV]	Flux [n MeV^{-1} uC^{-1} Sr^{-1}]	Flux Error [±]
9.04	9.52	3.168e+08	6.121e+06
9.52	10.00	2.542e+08	5.056e+06
10.00	10.48	1.781e+08	3.653e+06
10.48	10.96	1.201e+08	2.610e+06
10.96	11.44	8.264e+07	1.922e+06
11.44	11.92	5.585e+07	1.398e+06
11.92	12.40	3.774e+07	1.006e+06
12.40	12.88	3.101e+07	8.980e+05
12.88	13.52	2.210e+07	6.182e+05
13.52	14.00	1.532e+07	5.821e+05
14.00	14.64	7.303e+06	3.149e+05
14.64	15.44	2.119e+06	1.515e+05
15.44	16.08	4.930e+05	1.078e+05
16.08	16.72	3.051e+05	9.777e+04
16.72	17.36	6.834e+03	7.926e+04
17.36	18.16	5.762e+04	7.402e+04
18.16	19.12	1.254e+05	6.174e+04
19.12	20.24	5.831e+04	5.179e+04
20.24	21.52	-3.016e+04	4.836e+04
21.52	22.64	5.111e+04	5.728e+04
22.64	24.08	-9.516e+03	4.520e+04
24.08	25.52	1.693e+04	4.215e+04
25.52	26.64	3.077e+04	7.538e+04
26.64	27.92	1.376e+05	1.462e+05
27.92	29.68	1.218e+05	3.757e+05
29.68	31.12	-8.925e+05	4.322e+05

Table A.2: STOF-determined neutron flux for dataset 14(^{56}Fe) with adjusted LY parameter value, section 4.3.4.

A.3 Dataset 14(NaCl)

Lower Bin Edge [MeV]	Upper Bin Edge [MeV]	Flux [n MeV^{-1} uC^{-1} Sr^{-1}]	Flux Error [±]
1.40	1.48	0.000e+00	0.000e+00
1.48	1.56	1.176e+09	1.615e+08
1.56	1.64	3.041e+08	1.736e+07
1.64	1.72	2.280e+08	9.060e+06
1.72	1.80	2.224e+08	7.369e+06
1.80	1.88	2.603e+08	7.919e+06
1.88	1.96	2.958e+08	8.545e+06
1.96	2.04	3.194e+08	8.916e+06
2.04	2.12	4.096e+08	1.172e+07
2.12	2.28	4.400e+08	8.336e+06
2.28	2.44	4.642e+08	8.363e+06
2.44	2.60	5.345e+08	9.620e+06
2.60	2.76	5.810e+08	1.037e+07
2.76	2.92	6.951e+08	1.270e+07
2.92	3.08	7.420e+08	1.352e+07
3.08	3.24	7.279e+08	1.297e+07
3.24	3.40	7.847e+08	1.433e+07
3.40	3.56	8.074e+08	1.492e+07
3.56	3.72	8.181e+08	1.547e+07
3.72	3.88	7.909e+08	1.483e+07
3.88	4.04	8.186e+08	1.553e+07
4.04	4.20	8.265e+08	1.580e+07
4.20	4.44	8.386e+08	1.326e+07
4.44	4.68	8.590e+08	1.370e+07
4.68	4.92	8.780e+08	1.398e+07
4.92	5.16	9.154e+08	1.488e+07
5.16	5.40	9.090e+08	1.507e+07
5.40	5.64	8.842e+08	1.474e+07
5.64	5.88	9.323e+08	1.617e+07
5.88	6.12	9.590e+08	1.706e+07
6.12	6.44	9.499e+08	1.507e+07
6.44	6.68	9.002e+08	1.688e+07
6.68	7.08	8.060e+08	1.165e+07
7.08	7.40	7.837e+08	1.301e+07
7.40	7.72	8.003e+08	1.373e+07
7.72	8.04	8.022e+08	1.416e+07
8.04	8.44	7.666e+08	1.230e+07
8.44	8.84	6.997e+08	1.133e+07
8.84	9.24	6.407e+08	1.064e+07
9.24	9.64	5.536e+08	9.526e+06

Lower Bin Edge [MeV]	Upper Bin Edge [MeV]	Flux [n MeV^{-1} uC^{-1} Sr^{-1}]	Flux Error [±]
9.64	10.04	4.363e+08	7.708e+06
10.04	10.52	3.075e+08	5.115e+06
10.52	10.92	2.158e+08	4.171e+06
10.92	11.48	1.506e+08	2.636e+06
11.48	11.96	9.895e+07	2.007e+06
11.96	12.68	7.429e+07	1.339e+06
12.68	13.24	5.168e+07	1.151e+06
13.24	13.88	3.473e+07	8.292e+05
13.88	14.36	2.180e+07	7.342e+05
14.36	15.08	1.013e+07	3.834e+05
15.08	15.80	5.659e+06	3.133e+05
15.80	16.60	4.112e+06	2.747e+05
16.60	17.40	2.479e+06	2.507e+05
17.40	18.36	1.826e+06	2.246e+05
18.36	19.24	1.060e+06	2.418e+05
19.24	20.44	1.224e+06	2.466e+05
20.44	21.56	2.564e+05	2.878e+05
21.56	22.76	8.459e+05	3.264e+05
22.76	23.72	-9.621e+05	4.998e+05
23.72	24.76	-5.351e+05	1.020e+06
24.76	26.28	-1.935e+06	5.711e+06
26.28	27.72	-2.612e+08	2.027e+08
27.72	29.48	5.791e+08	7.451e+08
29.48	31.00	0.000e+00	0.000e+00

Table A.3: STOF-determined neutron flux for dataset 14(NaCl).

A.4 Dataset 23(Al_2O_3)

Lower Bin Edge [MeV]	Upper Bin Edge [MeV]	Flux [n MeV^{-1} uC^{-1} Sr^{-1}]	Flux Error [±]
0.24	0.40	0.000e+00	0.000e+00
0.40	0.56	0.000e+00	0.000e+00
0.56	0.72	0.000e+00	0.000e+00
0.72	0.88	0.000e+00	0.000e+00
0.88	1.04	0.000e+00	0.000e+00
1.04	1.20	0.000e+00	0.000e+00
1.20	1.36	0.000e+00	0.000e+00
1.36	1.52	0.000e+00	0.000e+00
1.52	1.68	0.000e+00	0.000e+00
1.68	1.84	0.000e+00	0.000e+00
1.84	2.00	0.000e+00	0.000e+00
2.00	2.16	0.000e+00	0.000e+00
2.16	2.32	0.000e+00	0.000e+00
2.32	2.48	0.000e+00	0.000e+00
2.48	2.64	0.000e+00	0.000e+00
2.64	2.80	0.000e+00	0.000e+00
2.80	2.96	1.918e+10	1.922e+10
2.96	3.12	9.450e+08	1.525e+08
3.12	3.28	4.993e+08	4.227e+07
3.28	3.44	4.089e+08	2.240e+07
3.44	3.60	5.350e+08	2.504e+07
3.60	3.76	6.582e+08	2.683e+07
3.76	3.92	9.173e+08	3.725e+07
3.92	4.08	9.589e+08	3.557e+07
4.08	4.24	1.116e+09	4.103e+07
4.24	4.40	1.306e+09	4.865e+07
4.40	4.56	1.309e+09	4.612e+07
4.56	4.72	1.445e+09	5.097e+07
4.72	4.88	1.440e+09	4.909e+07
4.88	5.04	1.505e+09	5.113e+07
5.04	5.36	1.626e+09	3.923e+07
5.36	5.52	1.865e+09	6.633e+07
5.52	5.84	1.834e+09	4.481e+07
5.84	6.16	2.086e+09	5.309e+07
6.16	6.48	2.066e+09	5.216e+07
6.48	6.80	2.054e+09	5.185e+07
6.80	7.12	2.084e+09	5.357e+07
7.12	7.44	2.042e+09	5.247e+07
7.44	7.76	2.150e+09	5.738e+07
7.76	8.08	2.152e+09	5.744e+07

Lower Bin Edge [MeV]	Upper Bin Edge [MeV]	Flux [n MeV^{-1} uC^{-1} Sr^{-1}]	Flux Error [±]
8.08	8.40	2.161e+09	5.740e+07
8.40	8.72	2.136e+09	5.649e+07
8.72	9.04	2.239e+09	6.105e+07
9.04	9.36	2.345e+09	6.635e+07
9.36	9.84	2.318e+09	5.489e+07
9.84	10.16	2.252e+09	6.643e+07
10.16	10.48	2.213e+09	6.631e+07
10.48	10.96	2.230e+09	5.683e+07
10.96	11.44	1.968e+09	4.948e+07
11.44	11.92	1.931e+09	5.066e+07
11.92	12.24	1.869e+09	6.223e+07
12.24	12.88	1.859e+09	4.630e+07
12.88	13.52	1.606e+09	4.078e+07
13.52	14.16	1.358e+09	3.509e+07
14.16	14.80	1.168e+09	3.147e+07
14.80	15.44	1.018e+09	2.832e+07
15.44	16.08	9.785e+08	2.922e+07
16.08	16.88	8.440e+08	2.305e+07
16.88	17.68	7.235e+08	2.046e+07
17.68	18.16	6.610e+08	2.586e+07
18.16	19.12	4.549e+08	1.267e+07
19.12	19.92	2.864e+08	9.509e+06
19.92	20.88	1.992e+08	7.105e+06
20.88	21.84	1.019e+08	4.035e+06
21.84	22.64	5.993e+07	3.136e+06
22.64	23.44	3.084e+07	1.991e+06
23.44	24.40	1.495e+07	1.322e+06
24.40	25.52	4.853e+06	8.367e+05
25.52	26.80	1.849e+06	6.098e+05
26.80	27.92	4.340e+05	6.217e+05
27.92	30.16	-3.344e+05	4.448e+05
30.16	31.60	-1.486e+06	4.833e+05

Table A.4: STOF-determined neutron flux for dataset 23(Al_2O_3).

Appendix B

Maximum Entropy Unfolded Neutron Flux

B.1 Dataset 14(^{56}Fe) Not Adjusted

Lower Bin Edge [MeV]	Upper Bin Edge [MeV]	Input Flux	Unfolded Flux
0.24	0.40	0.000e+00	0.000e+00
0.40	0.56	8.215e+05	8.333e+05
0.56	0.72	2.875e+06	3.020e+06
0.72	0.88	4.929e+06	5.469e+06
0.88	1.04	6.983e+06	8.421e+06
1.04	1.20	9.037e+06	1.187e+07
1.20	1.36	1.109e+07	1.553e+07
1.36	1.52	1.314e+07	1.911e+07
1.52	1.68	1.520e+07	2.261e+07
1.68	1.84	1.725e+07	2.583e+07
1.84	2.00	1.931e+07	2.920e+07
2.00	2.16	5.001e+07	6.586e+07
2.16	2.32	8.071e+07	1.039e+08
2.32	2.48	1.283e+08	1.628e+08
2.48	2.64	1.605e+08	2.025e+08
2.64	2.80	2.073e+08	2.584e+08
2.80	2.96	2.283e+08	2.817e+08
2.96	3.12	2.767e+08	3.366e+08
3.12	3.28	3.011e+08	3.614e+08
3.28	3.44	3.274e+08	3.883e+08
3.44	3.60	3.593e+08	4.212e+08
3.60	3.76	3.713e+08	4.305e+08
3.76	3.92	3.827e+08	4.391e+08
3.92	4.08	3.666e+08	4.167e+08
4.08	4.24	3.718e+08	4.188e+08
4.24	4.40	3.805e+08	4.251e+08
4.40	4.72	3.909e+08	4.336e+08
4.72	5.04	4.022e+08	4.424e+08
5.04	5.36	4.182e+08	4.563e+08
5.36	5.68	4.272e+08	4.635e+08
5.68	6.00	4.319e+08	4.659e+08
6.00	6.32	4.149e+08	4.447e+08
6.32	6.64	4.566e+08	4.862e+08
6.64	6.96	4.162e+08	4.403e+08
6.96	7.28	3.923e+08	4.124e+08
7.28	7.60	3.839e+08	4.012e+08
7.60	7.92	3.987e+08	4.142e+08
7.92	8.24	3.817e+08	3.943e+08
8.24	8.56	3.968e+08	4.076e+08
8.56	9.04	3.698e+08	3.779e+08

Lower Bin Edge [MeV]	Upper Bin Edge [MeV]	Input Flux	Unfolded Flux
9.04	9.52	3.477e+08	3.529e+08
9.52	10.00	3.104e+08	3.126e+08
10.00	10.48	2.509e+08	2.506e+08
10.48	10.96	1.749e+08	1.732e+08
10.96	11.44	1.183e+08	1.159e+08
11.44	11.92	8.142e+07	7.888e+07
11.92	12.40	5.530e+07	5.288e+07
12.40	12.88	3.749e+07	3.542e+07
12.88	13.52	3.080e+07	2.888e+07
13.52	14.00	2.200e+07	2.060e+07
14.00	14.64	1.522e+07	1.434e+07
14.64	15.44	7.240e+06	6.896e+06
15.44	16.08	2.116e+06	2.046e+06
16.08	16.72	4.919e+05	4.818e+05
16.72	17.36	3.063e+05	3.027e+05
17.36	18.16	6.742e+03	6.710e+03
18.16	19.12	5.786e+04	5.795e+04
19.12	20.24	1.251e+05	1.259e+05
20.24	21.52	5.849e+04	5.913e+04
21.52	22.64	0.000e+00	0.000e+00
22.64	24.08	0.000e+00	0.000e+00
24.08	25.52	0.000e+00	0.000e+00
25.52	26.64	0.000e+00	0.000e+00
26.64	27.92	0.000e+00	0.000e+00
27.92	29.68	0.000e+00	0.000e+00
29.68	31.12	0.000e+00	0.000e+00

Table B.1: Input and unfolded neutron flux spectrum in units of [neutrons MeV^{-1} uC^{-1} Sr^{-1}] for dataset 14(^{56}Fe) (not adjusted). The input spectrum is air corrected and linearly extrapolated to low energy, section 4.3.

B.2 Dataset 14(^{56}Fe) Adjusted

Lower Bin Edge [MeV]	Upper Bin Edge [MeV]	Input Flux	Unfolded Flux
0.24	0.40	1.619e+06	1.619e+06
0.40	0.56	5.665e+06	5.664e+06
0.56	0.72	9.712e+06	9.707e+06
0.72	0.88	1.376e+07	1.375e+07
0.88	1.04	1.781e+07	1.778e+07
1.04	1.20	2.185e+07	2.181e+07
1.20	1.36	2.590e+07	2.584e+07
1.36	1.52	5.229e+07	5.219e+07
1.52	1.68	7.868e+07	7.853e+07
1.68	1.84	1.051e+08	1.049e+08
1.84	2.00	1.315e+08	1.312e+08
2.00	2.16	1.579e+08	1.574e+08
2.16	2.32	2.104e+08	2.098e+08
2.32	2.48	2.354e+08	2.346e+08
2.48	2.64	2.901e+08	2.891e+08
2.64	2.80	2.946e+08	2.935e+08
2.80	2.96	3.471e+08	3.457e+08
2.96	3.12	3.682e+08	3.666e+08
3.12	3.28	3.883e+08	3.864e+08
3.28	3.44	4.183e+08	4.162e+08
3.44	3.60	4.345e+08	4.322e+08
3.60	3.76	4.322e+08	4.298e+08
3.76	3.92	4.119e+08	4.095e+08
3.92	4.08	4.116e+08	4.091e+08
4.08	4.24	4.208e+08	4.181e+08
4.24	4.40	4.348e+08	4.319e+08
4.40	4.72	4.414e+08	4.383e+08
4.72	5.04	4.531e+08	4.496e+08
5.04	5.36	4.624e+08	4.587e+08
5.36	5.68	4.641e+08	4.602e+08
5.68	6.00	4.463e+08	4.424e+08
6.00	6.32	4.830e+08	4.786e+08
6.32	6.64	4.387e+08	4.345e+08
6.64	6.96	4.131e+08	4.090e+08
6.96	7.28	4.022e+08	3.979e+08
7.28	7.60	4.200e+08	4.154e+08
7.60	7.92	4.008e+08	3.962e+08
7.92	8.24	4.140e+08	4.090e+08
8.24	8.56	3.876e+08	3.827e+08
8.56	9.04	3.631e+08	3.584e+08

Lower Bin Edge [MeV]	Upper Bin Edge [MeV]	Input Flux	Unfolded Flux
9.04	9.52	3.217e+08	3.172e+08
9.52	10.00	2.583e+08	2.546e+08
10.00	10.48	1.812e+08	1.785e+08
10.48	10.96	1.222e+08	1.203e+08
10.96	11.44	8.406e+07	8.280e+07
11.44	11.92	5.686e+07	5.601e+07
11.92	12.40	3.843e+07	3.786e+07
12.40	12.88	3.160e+07	3.115e+07
12.88	13.52	2.252e+07	2.221e+07
13.52	14.00	1.561e+07	1.541e+07
14.00	14.64	7.442e+06	7.355e+06
14.64	15.44	2.160e+06	2.138e+06
15.44	16.08	5.023e+05	4.979e+05
16.08	16.72	3.108e+05	3.084e+05
16.72	17.36	6.921e+03	6.870e+03
17.36	18.16	5.863e+04	5.829e+04
18.16	19.12	1.277e+05	1.271e+05
19.12	20.24	5.938e+04	5.914e+04
20.24	21.52	0.000e+00	0.000e+00
21.52	22.64	0.000e+00	0.000e+00
22.64	24.08	0.000e+00	0.000e+00
24.08	25.52	0.000e+00	0.000e+00
25.52	26.64	0.000e+00	0.000e+00
26.64	27.92	0.000e+00	0.000e+00
27.92	29.68	0.000e+00	0.000e+00
29.68	31.12	0.000e+00	0.000e+00

Table B.2: Input and unfolded neutron flux spectrum in units of [neutrons MeV^{-1} uC^{-1} Sr^{-1}] for dataset 14(^{56}Fe) (adjusted). The input spectrum is air corrected and linearly extrapolated to low energy, section 4.3.

B.3 Dataset 14(NaCl)

Lower Bin Edge [MeV]	Upper Bin Edge [MeV]	Input Flux	Unfolded Flux
0.20	0.28	0.000e+00	0.000e+00
0.28	0.36	8.303e+05	8.278e+05
0.36	0.44	3.598e+06	3.552e+06
0.44	0.52	6.365e+06	6.260e+06
0.52	0.60	9.133e+06	8.914e+06
0.60	0.68	1.190e+07	1.149e+07
0.68	0.76	1.467e+07	1.397e+07
0.76	0.84	1.744e+07	1.636e+07
0.84	0.92	2.020e+07	1.865e+07
0.92	1.00	2.297e+07	2.087e+07
1.00	1.08	2.574e+07	2.308e+07
1.08	1.16	2.851e+07	2.523e+07
1.16	1.24	3.127e+07	2.746e+07
1.24	1.32	3.404e+07	2.964e+07
1.32	1.40	3.681e+07	3.178e+07
1.40	1.48	7.506e+07	6.766e+07
1.48	1.56	1.133e+08	1.032e+08
1.56	1.64	1.516e+08	1.385e+08
1.64	1.72	1.898e+08	1.734e+08
1.72	1.80	2.281e+08	2.080e+08
1.80	1.88	2.663e+08	2.421e+08
1.88	1.96	3.019e+08	2.735e+08
1.96	2.04	3.252e+08	2.931e+08
2.04	2.12	4.169e+08	3.754e+08
2.12	2.28	4.479e+08	4.011e+08
2.28	2.44	4.709e+08	4.194e+08
2.44	2.60	5.430e+08	4.832e+08
2.60	2.76	5.901e+08	5.252e+08
2.76	2.92	7.065e+08	6.305e+08
2.92	3.08	7.566e+08	6.766e+08
3.08	3.24	7.440e+08	6.661e+08
3.24	3.40	8.033e+08	7.204e+08
3.40	3.56	8.278e+08	7.433e+08
3.56	3.72	8.392e+08	7.548e+08
3.72	3.88	8.110e+08	7.301e+08
3.88	4.04	8.389e+08	7.559e+08
4.04	4.20	8.478e+08	7.646e+08
4.20	4.44	8.593e+08	7.753e+08
4.44	4.68	8.764e+08	7.906e+08
4.68	4.92	8.907e+08	8.027e+08

Lower Bin Edge [MeV]	Upper Bin Edge [MeV]	Input Flux	Unfolded Flux
4.92	5.16	9.308e+08	8.378e+08
5.16	5.40	9.256e+08	8.318e+08
5.40	5.64	9.006e+08	8.085e+08
5.64	5.88	9.488e+08	8.514e+08
5.88	6.12	9.760e+08	8.759e+08
6.12	6.44	9.662e+08	8.673e+08
6.44	6.68	9.146e+08	8.212e+08
6.68	7.08	8.182e+08	7.348e+08
7.08	7.40	7.986e+08	7.177e+08
7.40	7.72	8.151e+08	7.333e+08
7.72	8.04	8.173e+08	7.361e+08
8.04	8.44	7.792e+08	7.026e+08
8.44	8.84	7.113e+08	6.423e+08
8.84	9.24	6.513e+08	5.890e+08
9.24	9.64	5.629e+08	5.100e+08
9.64	10.04	4.440e+08	4.033e+08
10.04	10.52	3.132e+08	2.855e+08
10.52	10.92	2.198e+08	2.012e+08
10.92	11.48	1.534e+08	1.414e+08
11.48	11.96	1.009e+08	9.377e+07
11.96	12.68	7.578e+07	7.123e+07
12.68	13.24	5.273e+07	5.007e+07
13.24	13.88	3.544e+07	3.387e+07
13.88	14.36	2.225e+07	2.135e+07
14.36	15.08	1.034e+07	9.958e+06
15.08	15.80	5.775e+06	5.575e+06
15.80	16.60	4.195e+06	4.061e+06
16.60	17.40	2.529e+06	2.454e+06
17.40	18.36	1.863e+06	1.812e+06
18.36	19.24	1.082e+06	1.055e+06
19.24	20.44	0.000e+00	0.000e+00

Table B.3: Input and unfolded neutron flux spectrum in units of [neutrons MeV^{-1} uC^{-1} Sr^{-1}] for dataset 14(NaCl). The input spectrum is air corrected and linearly extrapolated to low energy, section 4.3.

B.4 Dataset 23(Al_2O_3)

Lower Bin Edge [MeV]	Upper Bin Edge [MeV]	Input Flux	Unfolded Flux
0.24	0.40	0.000e+00	0.000e+00
0.40	0.56	2.115e+06	2.535e+06
0.56	0.72	3.625e+06	5.182e+06
0.72	0.88	5.136e+06	9.329e+06
0.88	1.04	6.646e+06	1.505e+07
1.04	1.20	8.157e+06	2.067e+07
1.20	1.36	9.668e+06	2.505e+07
1.36	1.52	1.118e+07	2.813e+07
1.52	1.68	1.269e+07	2.929e+07
1.68	1.84	1.420e+07	2.988e+07
1.84	2.00	1.571e+07	2.942e+07
2.00	2.16	1.722e+07	2.889e+07
2.16	2.32	1.873e+07	2.761e+07
2.32	2.48	2.024e+07	2.569e+07
2.48	2.64	2.175e+07	2.372e+07
2.64	2.80	2.326e+07	2.238e+07
2.80	2.96	2.477e+07	2.128e+07
2.96	3.12	1.550e+08	1.439e+08
3.12	3.28	2.852e+08	2.632e+08
3.28	3.44	4.154e+08	3.786e+08
3.44	3.60	5.455e+08	4.907e+08
3.60	3.76	6.712e+08	5.950e+08
3.76	3.92	9.364e+08	8.208e+08
3.92	4.08	9.782e+08	8.447e+08
4.08	4.24	1.140e+09	9.723e+08
4.24	4.40	1.333e+09	1.124e+09
4.40	4.56	1.332e+09	1.108e+09
4.56	4.72	1.468e+09	1.208e+09
4.72	4.88	1.457e+09	1.186e+09
4.88	5.04	1.523e+09	1.227e+09
5.04	5.36	1.652e+09	1.313e+09
5.36	5.52	1.893e+09	1.487e+09
5.52	5.84	1.863e+09	1.447e+09
5.84	6.16	2.117e+09	1.626e+09
6.16	6.48	2.096e+09	1.599e+09
6.48	6.80	2.082e+09	1.587e+09
6.80	7.12	2.112e+09	1.619e+09
7.12	7.44	2.077e+09	1.604e+09
7.44	7.76	2.184e+09	1.703e+09
7.76	8.08	2.187e+09	1.726e+09

Lower Bin Edge [MeV]	Upper Bin Edge [MeV]	Input Flux	Unfolded Flux
8.08	8.40	2.192e+09	1.755e+09
8.40	8.72	2.166e+09	1.760e+09
8.72	9.04	2.271e+09	1.875e+09
9.04	9.36	2.378e+09	1.992e+09
9.36	9.84	2.352e+09	2.002e+09
9.84	10.16	2.287e+09	1.974e+09
10.16	10.48	2.249e+09	1.960e+09
10.48	10.96	2.266e+09	1.998e+09
10.96	11.44	2.000e+09	1.788e+09
11.44	11.92	1.964e+09	1.783e+09
11.92	12.24	1.902e+09	1.752e+09
12.24	12.88	1.892e+09	1.730e+09
12.88	13.52	1.634e+09	1.428e+09
13.52	14.16	1.383e+09	1.148e+09
14.16	14.80	1.189e+09	9.434e+08
14.80	15.44	1.036e+09	7.938e+08
15.44	16.08	9.959e+08	7.418e+08
16.08	16.88	8.588e+08	6.216e+08
16.88	17.68	7.362e+08	5.175e+08
17.68	18.16	6.727e+08	4.634e+08
18.16	19.12	4.628e+08	3.125e+08
19.12	19.92	2.914e+08	1.930e+08
19.92	20.88	2.027e+08	1.327e+08
20.88	21.84	1.036e+08	6.751e+07
21.84	22.64	6.094e+07	3.976e+07
22.64	23.44	3.135e+07	2.054e+07
23.44	24.40	1.520e+07	1.009e+07
24.40	25.52	4.932e+06	3.369e+06
25.52	26.80	1.879e+06	1.351e+06
26.80	27.92	4.409e+05	3.354e+05
27.92	30.16	0.000e+00	0.000e+00
30.16	31.60	0.000e+00	0.000e+00

Table B.4: Input and unfolded neutron flux spectrum in units of [neutrons MeV^{-1} uC^{-1} Sr^{-1}] for dataset 23(Al_2O_3). The input spectrum is air corrected and linearly extrapolated to low energy, section 4.3.

Appendix C

TOF Slices for Light Yield Calibration

C.1 Dataset 14(^{56}Fe)

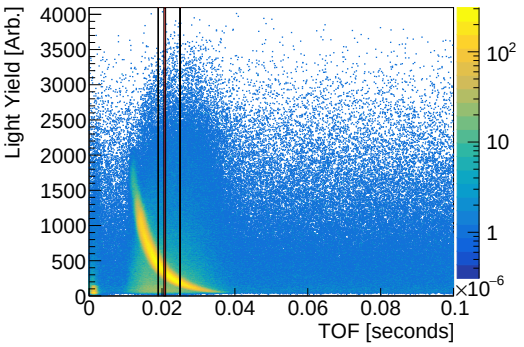

(a) TC

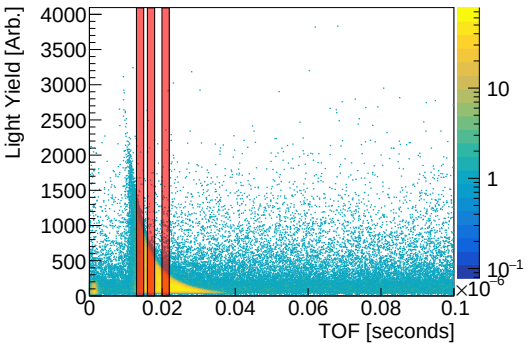

(b) SC1

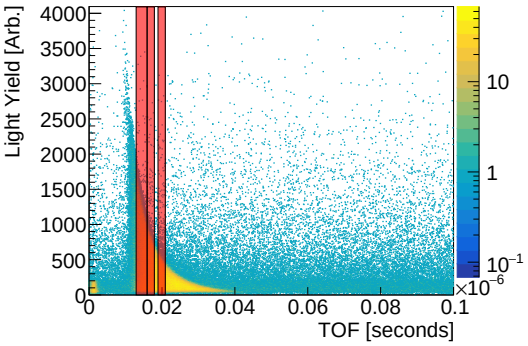

(c) SC2

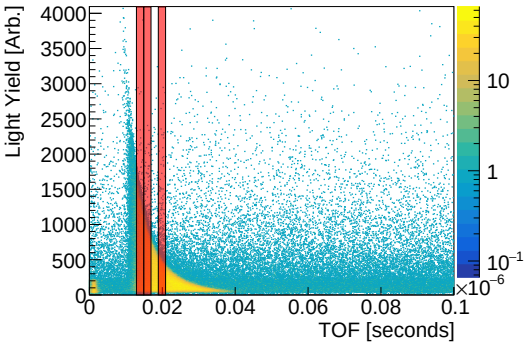

(d) SC3

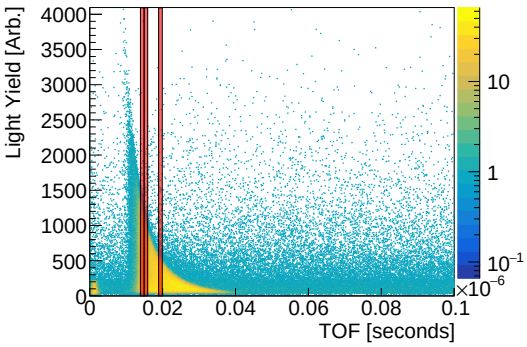

(e) SC4

Figure C.1: TOF spectra and slices for LY Calibrations for dataset 14(^{56}Fe).

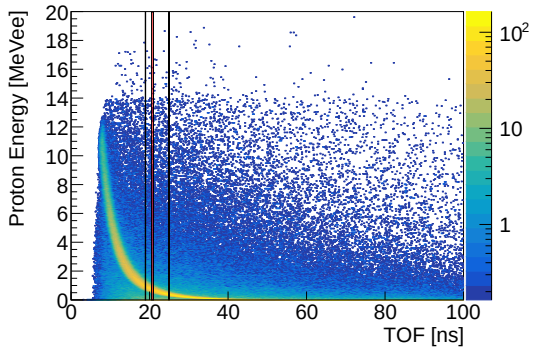

(a) TC

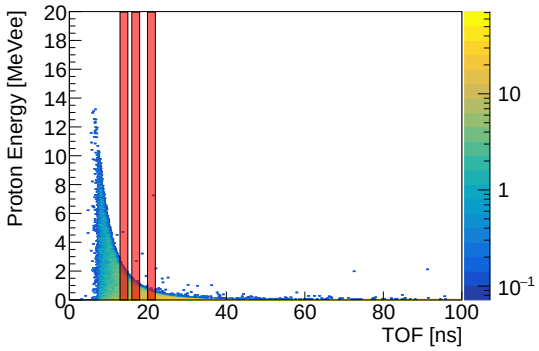

(b) SC1

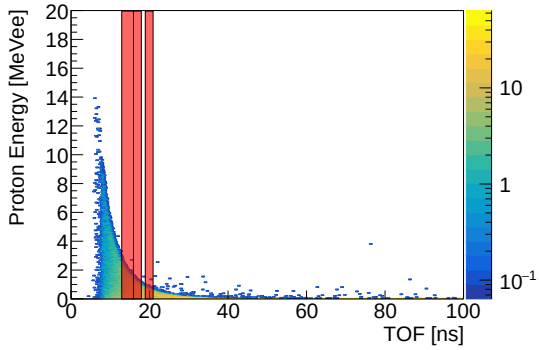

(c) SC2

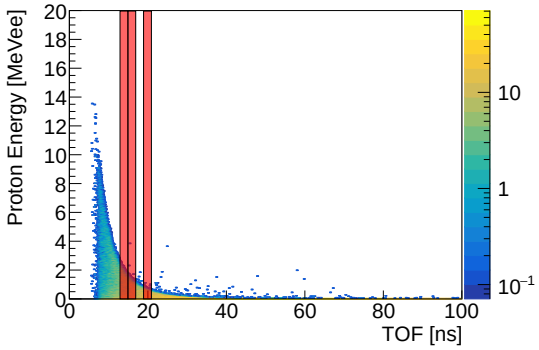

(d) SC3

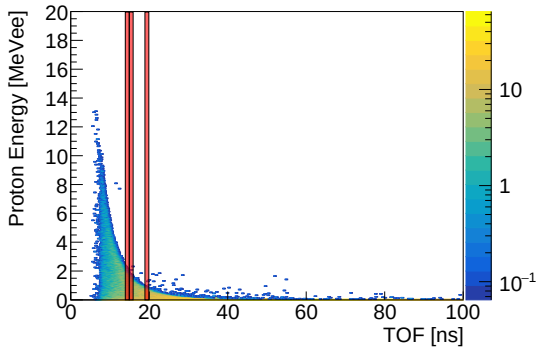

(e) SC4

Figure C.2: Simulated TOF spectra and slices for LY Calibrations for dataset 14(^{56}Fe).

C.2 Dataset 14(NaCl)

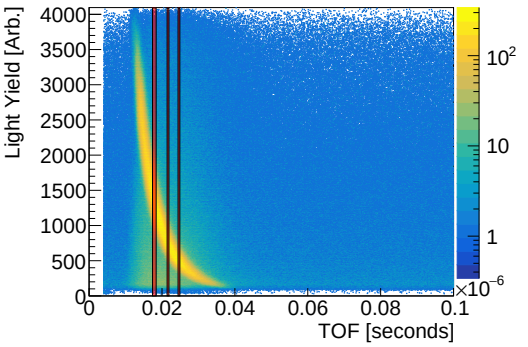

(a) TC

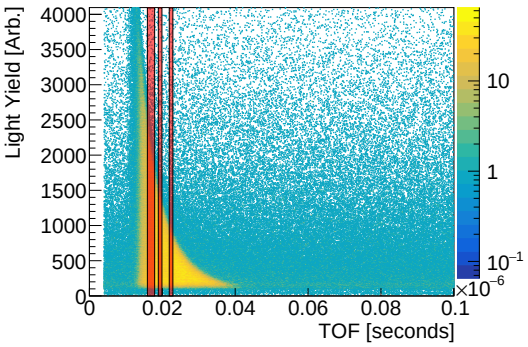

(b) SC1

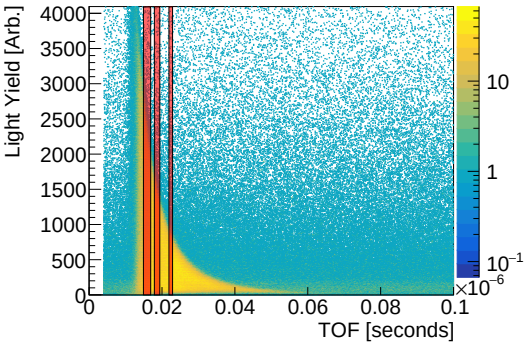

(c) SC2

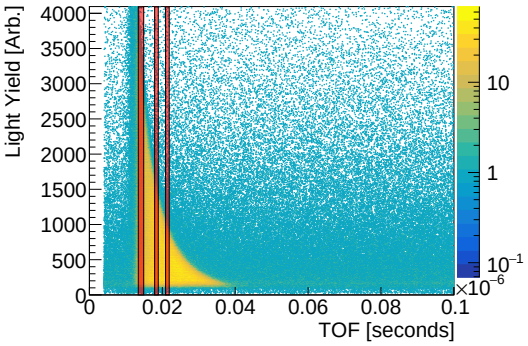

(d) SC3

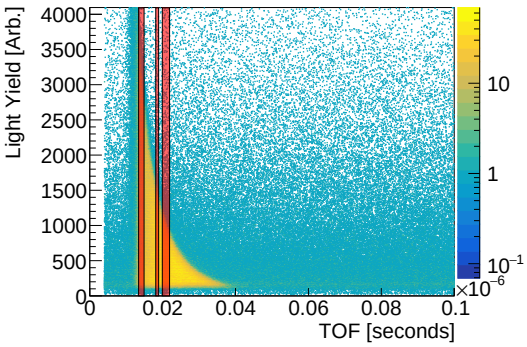

(e) SC4

Figure C.3: TOF spectra and slices for LY Calibrations for dataset 14(NaCl).

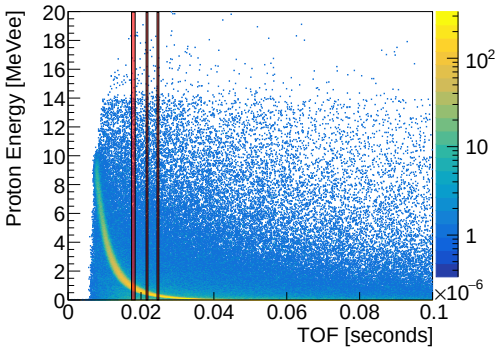

(a) TC

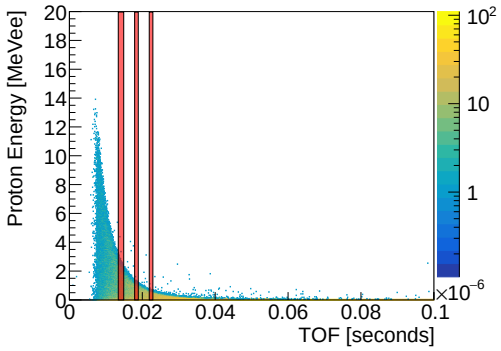

(b) SC1

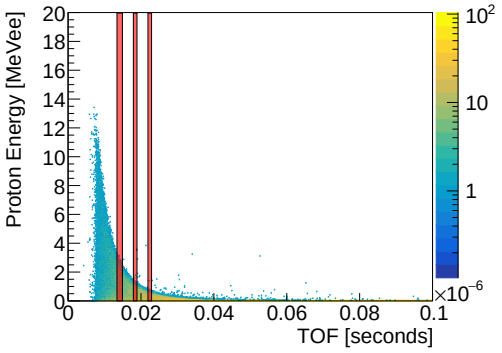

(c) SC2

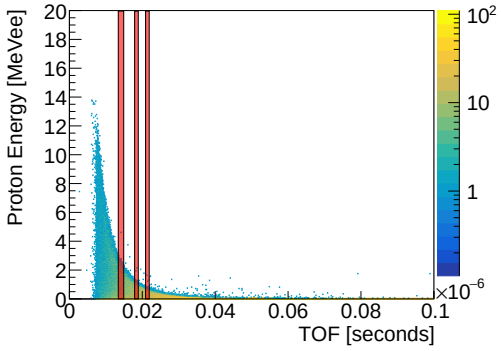

(d) SC3

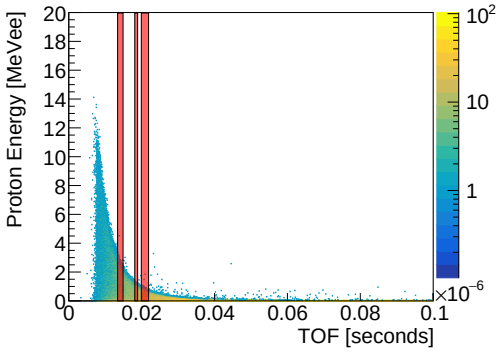

(e) SC4

Figure C.4: Simulated TOF spectra and slices for LY Calibrations for dataset 14(NaCl).

C.3 Dataset 23(Al_2O_3)

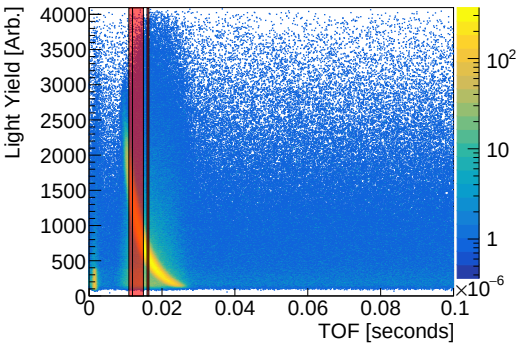

(a) TC

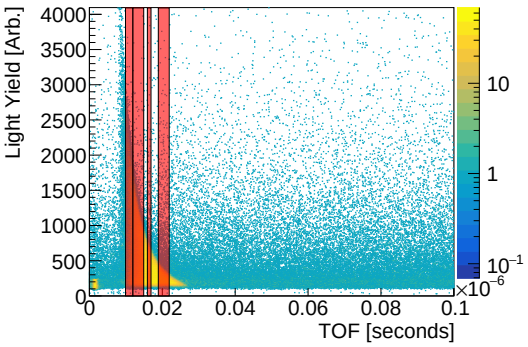

(b) SC1

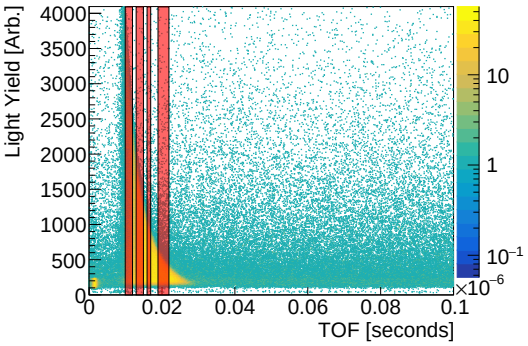

(c) SC2

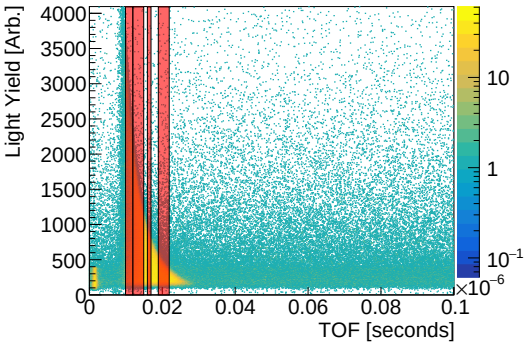

(d) SC3

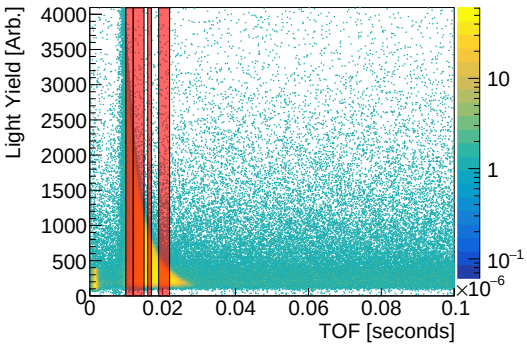

(e) SC4

Figure C.5: TOF spectra and slices for LY Calibrations for dataset 23(Al_2O_3).

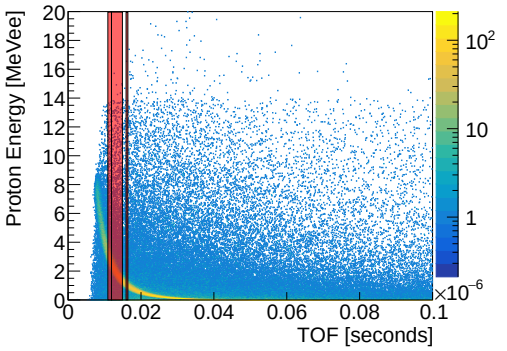

(a) TC

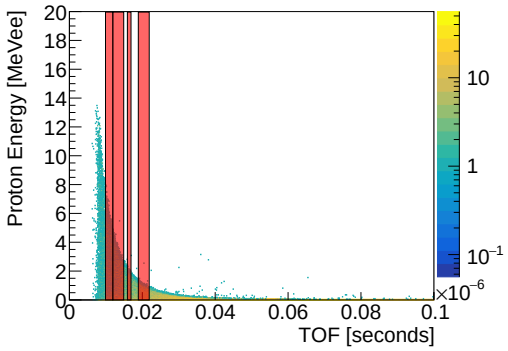

(b) SC1

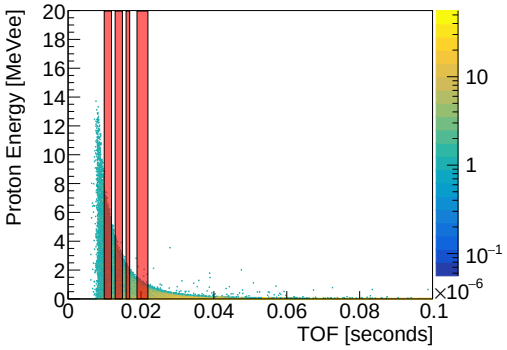

(c) SC2

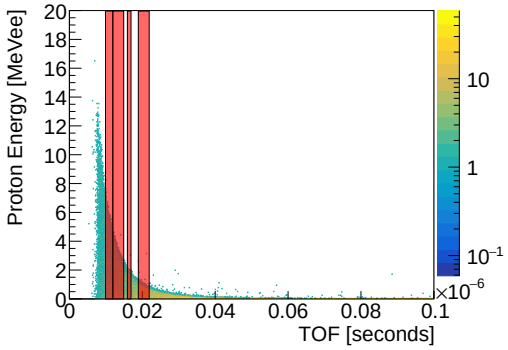

(d) SC3

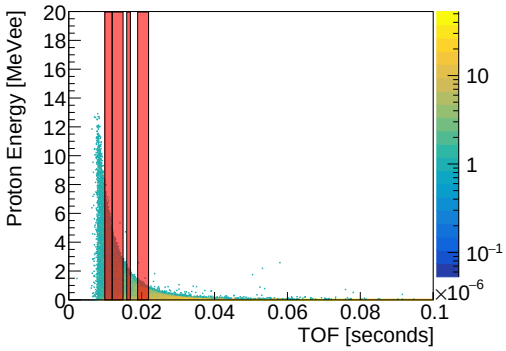

(e) SC4

Figure C.6: Simulated TOF spectra and slices for LY Calibrations for dataset 23(Al_2O_3).

Appendix D

Light Yield Calibrations

D.1 Dataset 14(^{56}Fe)

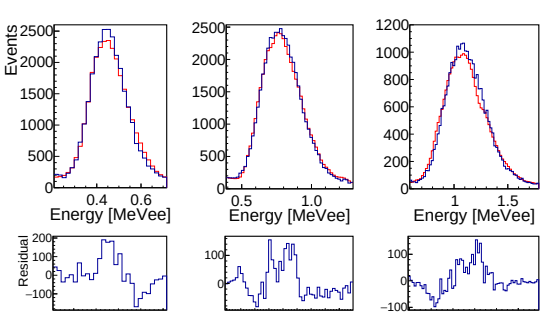

(a) TC

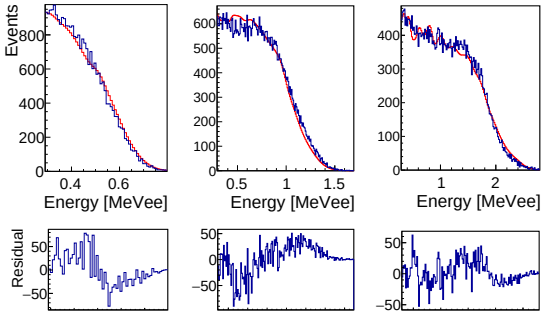

(b) SC1

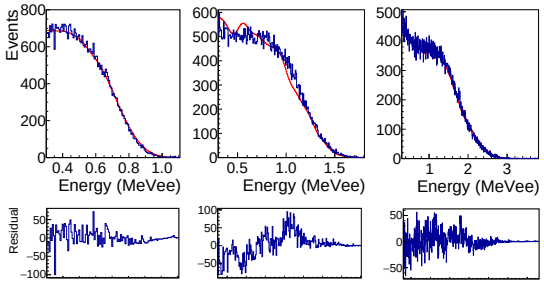

(c) SC2

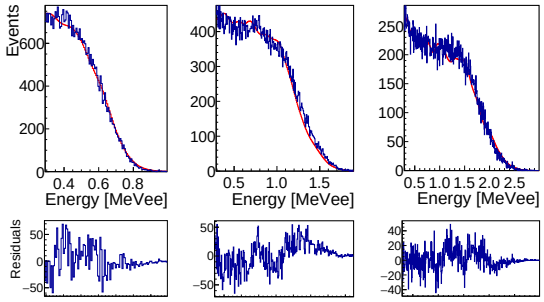

(d) SC3

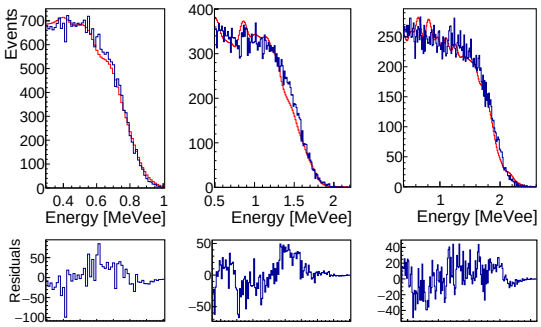

(e) SC4

Figure D.1: LY Calibration for each detector in dataset 14(^{56}Fe).

D.2 Dataset 14(NaCl)

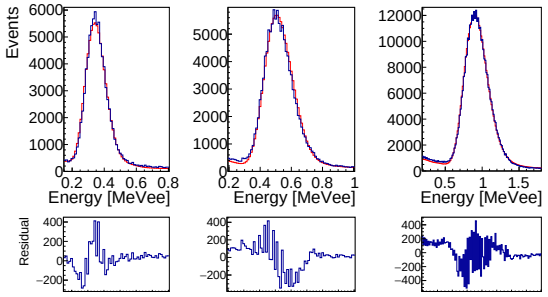

(a) TC

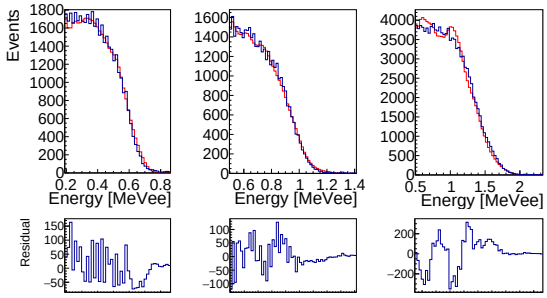

(b) SC1

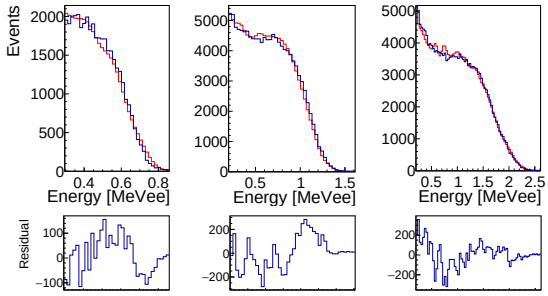

(c) SC2

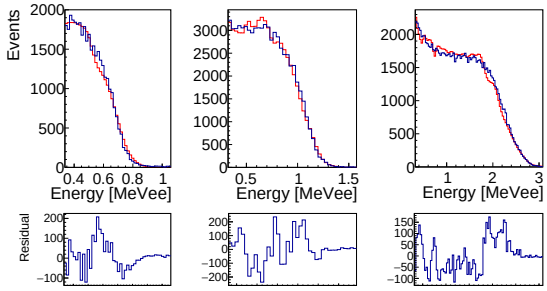

(d) SC3

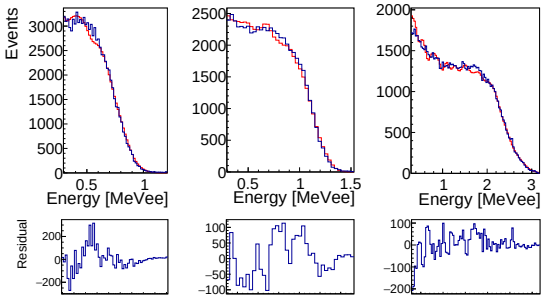

(e) SC4

Figure D.2: LY Calibration for each detector in dataset 14(NaCl).

D.3 Dataset 23(Al_2O_3)

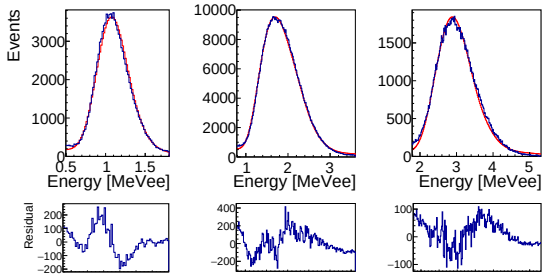

(a) TC

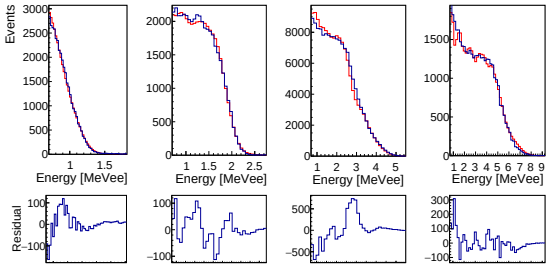

(b) SC1

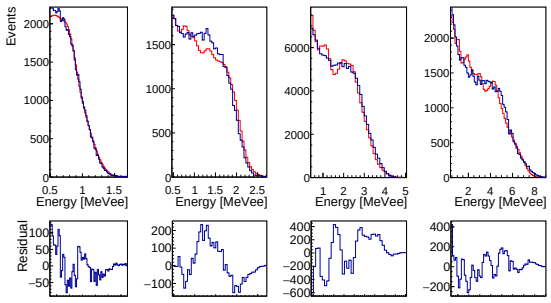

(c) SC2

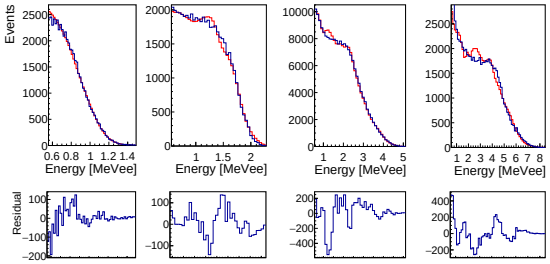

(d) SC3

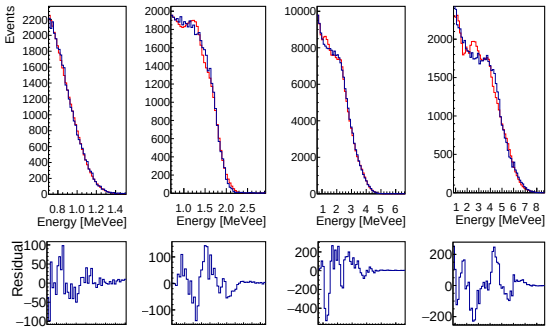

(e) SC4

Figure D.3: LY Calibration for each detector in dataset 23(Al_2O_3).

Appendix E

Python Analysis Code

NucToolSet_Thesis

April 30, 2024

[ ]:
```
# Python Script Containing Functions and Classes Used for Data Analysis
```

[ ]:
```
import numpy as np
from scipy.spatial.transform import Rotation as R
import pandas as pd
import uncertainties
from uncertainties import ufloat
import matplotlib.pyplot as plt
```

[ ]:
```
def ConvertUfloatToNumpy(a_array):
    # Function for converting an array of ufloat values into two numpy arrays.
    # First array contains the nominal_values and the second array contains the␣
 ↪std_dev values.
    a_returnValue = []
    a_returnErr   = []
    for x in a_array:
        a_returnValue.append(x.n)
        a_returnErr.append(x.s)

    return np.numpy(a_returnValue), np.numpy(a_returnErr)
```

[ ]:
```
class MCNP_tools(object):
    # Class consists of functions useful for MCNP input files
    def __init__(self):
        self.tallyResults = {}

    def print_MCNP_RotationMatrix(self, a_axis, a_rotation,␣
 ↪a_angleUnit='degree', a_returnUnit='degree'):
        a_Rotation = self.rotation(a_axis, a_rotation, a_angleUnit,␣
 ↪a_returnUnit)
        a_Rotation = a_Rotation.flatten()
        print('{:.2f} {:.2f} {:.2f} {:.2f} {:.2f} {:.2f} {:.2f} {:.2f} {:.2f}'.
 ↪format(
            ␣
 ↪a_Rotation[0],a_Rotation[1],a_Rotation[2],a_Rotation[3],a_Rotation[4],
              a_Rotation[5],a_Rotation[6],a_Rotation[7],a_Rotation[8]))
        return
```

```
   def rotation(self, a_axis, a_rotation, a_angleUnit='degree',␣
↪a_returnUnit='degree'):
       # This function uses scipy.spatial.transform.Rotation.from_euler() to␣
↪create a rotation matrix for use in MCNP.
       # The a_axis and a_rotation input format is that of scipy.spatial.
↪transform.Rotation.from_euler
       # See: https://docs.scipy.org/doc/scipy/reference/generated/scipy.
↪spatial.transform.Rotation.from_euler.html

       # test if a_returnUnit has acceptable input
       if(a_returnUnit.lower()!='degree' and a_returnUnit!='cos'):
           print('a_returnUnit must be set to Degree or Cos')
           return False

       # test if a_angleUnit has acceptable input
       if(a_angleUnit.lower()!='degree' and a_angleUnit!='cos' and a_angleUnit.
↪lower()!='rad'):
           print('Only acceptable units for a_angleUnit are Degree, Cos, or␣
↪Rad')
           return False

       # Convert to degrees if required
       if(a_angleUnit.lower()=='cos'):
           #assumes Cos(theta) where theta is in radians
           a_rotation = np.rad2deg(np.arccos(a_rotation))
       if(a_angleUnit.lower()=='rad'):
           a_rotation = np.rad2deg(a_rotation)

       a_rotation = R.from_euler(a_axis, a_rotation, degrees=True)

       if(a_returnUnit.lower()=='degree'):
           return np.rad2deg(np.arccos(a_rotation.as_dcm())).T
       else:
           return a_rotation.T

   def printAllTallies(self, a_filename):
       tallies = []
       with open(a_filename, 'r') as f:
           line = f.readline()
           while line:
               stripped = line.strip()
               split    = stripped.split()
#                print(split)
               if len(split) > 2:
                   #find start of tally
```

```
                    if (split[0] == '1tally') & (split[1]!='fluctuation') &␣
 ↪(split[2]=='nps'):
                        tallies.append(split[1])
                line = f.readline()
        print(tallies)
        return tallies

    def readInTallyInfo(self, a_filename, a_tallyNumber):
        tallyflag1 = 0
        tallyflag2 = 0
        self.tallyResults[a_tallyNumber] = {}
        self.tallyResults[a_tallyNumber]['Energy']         = []
        self.tallyResults[a_tallyNumber]['MCNP_Flux']      = []
        self.tallyResults[a_tallyNumber]['MCNP_FluxError'] = []
        with open(a_filename, 'r') as f:
            line = f.readline()
            while line:
                stripped = line.strip()
                split    = stripped.split()
#                 print(split)
                if len(split) > 0:
                    #find start of tally
                    if split[0] == '1tally':
                        if split[1] == a_tallyNumber:
                            tallyflag1 = 1
#                             print(split)
                    #find if tally is the list of tally energy bins
                    if len(split)>1:
                        if ((tallyflag1==1) & (split[0]=='energy') & (split[1]␣
 ↪== 'bins')):
                            tallyflag1 = 0
                    #if tally is results then set flag
                    if ((tallyflag1==1) & (split[0]=='energy')):
                        tallyflag2=1
                    #if reach end of tally results reset flags and record total
                    if ((tallyflag1==1) & (split[0]=='total') &␣
 ↪(tallyflag2==1)):
                        tallyflag1=0
                        tallyflag2=0
                        self.tallyResults[a_tallyNumber]['Total'] =␣
 ↪float(split[1])
                        self.tallyResults[a_tallyNumber]['Total_Error'] =␣
 ↪float(split[2])
#                         print(split)
                    # read in tally results
                    if ((tallyflag1==1) & (split[0]!='energy') &␣
 ↪(tallyflag2==1)):
```

```
                        if float(split[0]) != 0:
                            self.tallyResults[a_tallyNumber]['Energy'].
 ↪append(float(split[0]))
                            self.tallyResults[a_tallyNumber]['MCNP_Flux'].
 ↪append(float(split[1]))
                            self.tallyResults[a_tallyNumber]['MCNP_FluxError'].
 ↪append(float(split[2]))
#                           print(split)


                line = f.readline()

    def printTallies(self):
        for x in self.tallyResults:
            print('Tally: {}'.format(x))
            for y in self.tallyResults[x]['MCNP_Flux']:
                print('{}'.format((y)))
    def getTallyResults(self, a_tallyID):
        return np.array(self.tallyResults[a_tallyID]['MCNP_Flux'])
    def getTallyEnergy(self, a_tallyID):
        return np.array(self.tallyResults[a_tallyID]['Energy'])
    def getTallyResultsError(self, a_tallyID):
        return np.array(self.tallyResults[a_tallyID]['MCNP_FluxError'])
```

[ ]:
```
# These functions are used by the Activation_Analysis() class to perform unit␣
 ↪conversions.
def timeUnitConverter(a_timeInputList):
    # Input a list where list[0] is time and list[1] is the units
    # Set string to all lower case
    a_timeInputList[1] = a_timeInputList[1].lower()
    if (a_timeInputList[1] == 'seconds') | (a_timeInputList[1] == 'second') |␣
 ↪(a_timeInputList[1] == 'secs') | (a_timeInputList[1] == 'sec') |␣
 ↪(a_timeInputList[1] == 's'):
        return a_timeInputList[0]

    if (a_timeInputList[1] == 'min') | (a_timeInputList[1] == 'minute') |␣
 ↪(a_timeInputList[1] == 'minutes') | (a_timeInputList[1] == 'mins'):
        return a_timeInputList[0]*60.0

    if (a_timeInputList[1] == 'hours') | (a_timeInputList[1] == 'hour') |␣
 ↪(a_timeInputList[1] == 'hrs') | (a_timeInputList[1] == 'hr'):
        return a_timeInputList[0] * 60.0 * 60.0

    if (a_timeInputList[1] == 'days') | (a_timeInputList[1] == 'day') |␣
 ↪(a_timeInputList[1] == 'd'):
        return a_timeInputList[0] * 60.0 * 60.0 * 24.0
```

```
    if (a_timeInputList[1] == 'years') | (a_timeInputList[1] == 'year') |␣
 ↪(a_timeInputList[1] == 'yrs') | (a_timeInputList[1] == 'yr'):
        return a_timeInputList[0] * 60.0 * 60.0 * 24.0 * 365.25

    print('Error: Time Unit Not regonized for following input')
    print(a_timeInputList)
    return None

def energyUnitConverter(a_energyInputList):
    # Input a list where list[0] is time and list[1] is the units
    # Set string to all lower case
    a_energyInputList[1] = a_energyInputList[1].lower()
    if (a_energyInputList[1] == 'eV'):
        return a_energyInputList[0] / (1*10**(-3))
    if (a_energyInputList[1] == 'keV'):
        return a_energyInputList[0]
    if (a_energyInputList[1] == 'MeV'):
        print('******** WARNING: milli-eV (10^{-3}) is not implimented,␣
 ↪Assuming input is Mega-eV (10^{3}) ********')
        return a_energyInputList[0]*(1*10**3)

    print('Error: Energy Unit Not regonized for following input')
    print(a_energyInputList)
    return None

def xsUnitConverter(a_xsInputList):
    # Input a list where list[0] is time and list[1] is the units
    # Set string to all lower case
    a_xsInputList[1] = a_xsInputList[1].lower()
    if (a_xsInputList[1] == 'b'):
        return a_xsInputList[0]
    if (a_xsInputList[1] == 'cm2'):
        return a_xsInputList[0] *10**(24)

    print('Error: Xs Unit Not regonized for following input')
    print(a_xsInputList)
    return None

def massUnitConverter(a_massInputList):
    # Input a list where list[0] is time and list[1] is the units
    # Set string to all lower case
    a_massInputList[1] = a_massInputList[1].lower()
    if (a_massInputList[1] == 'micrograms') | (a_massInputList[1] ==␣
 ↪'microgram') | (a_massInputList[1] == 'ug'):
        return a_massInputList[0]*(10**(-6))
```

```
    if (a_massInputList[1] == 'milligrams') | (a_massInputList[1] ==␣
↪'milligram') | (a_massInputList[1] == 'mg'):
        return a_massInputList[0]*(10**(-3))
    if (a_massInputList[1] == 'grams') | (a_massInputList[1] == 'gram') |␣
↪(a_massInputList[1] == 'g'):
        return a_massInputList[0]
    if (a_massInputList[1] == 'kilograms') | (a_massInputList[1] == 'kilogram')␣
↪| (a_massInputList[1] == 'kgs') | (a_massInputList[1] == 'kg'):
        return a_massInputList[0]*(10**(3))

    print('Error: Mass Unit Not regonized for following input')
    print(a_massInputList)
    return None

def actUnitConverter(a_actInputList):
    # Input a list where list[0] is time and list[1] is the units
    # Set string to all lower case
    a_actInputList[1] = a_actInputList[1].lower()
    if (a_actInputList[1] == 'becquerel') | (a_actInputList[1] == 'bq'):
        return a_actInputList[0]
    if (a_actInputList[1] == 'curie') | (a_actInputList[1] == 'ci'):
        return a_actInputList[0] * 3.7*10**(10)

    print('Error: Activity Unit Not regonized for following input')
    print(a_actInputList)
    return None

def currentUnitConverter(a_currentInputList):
    # Input a list where list[0] is time and list[1] is the units
    # Set string to all lower case
    a_currentInputList[1] = a_currentInputList[1].lower()
    if (a_currentInputList[1] == 'amps') | (a_currentInputList[1] == 'amp')|␣
↪(a_currentInputList[1] == 'a'):
        return a_currentInputList[0]*10**(-6)
    if (a_currentInputList[1] == 'microamps') | (a_currentInputList[1] ==␣
↪'microamp')| (a_currentInputList[1] == 'ua'):
        return a_currentInputList[0]

    print('Error: Current Unit Not regonized for following input')
    print(a_currentInputList)
    return None


def distanceUnitConverter(a_disInputList):
    # Input a list where list[0] is time and list[1] is the units
    # Set string to all lower case
    a_disInputList[1] = a_disInputList[1].lower()
```

```
    if (a_disInputList[1] == 'micrometers') | (a_disInputList[1] ==␣
 ↪'micrometer')| (a_disInputList[1] == 'um'):
        return a_disInputList[0]*10**(-4)
    if (a_disInputList[1] == 'millimenters') | (a_disInputList[1] ==␣
 ↪'millimenter')| (a_disInputList[1] == 'mm'):
        return a_disInputList[0]*10**(-1)
    if (a_disInputList[1] == 'centimeters') | (a_disInputList[1] ==␣
 ↪'centimeter')| (a_disInputList[1] == 'cm'):
        return a_disInputList[0]
    if (a_disInputList[1] == 'meters') | (a_disInputList[1] == 'meter')|␣
 ↪(a_disInputList[1] == 'm'):
        return a_disInputList[0]*10**(2)

    print('Error: Distance Unit Not regonized for following input')
    print(a_disInputList)
    return None

class Activation_Analysis(object):
    # This class uses data from an Activation Foil Experiment to calculate␣
 ↪various outputs
    def __init__(self):
        # Energy units are [KeV]
        # distance units are [cm]
        # Activity units are [Bq]
        # Mass units are [g]
        # time units are [s]
        # Current units are [uA]
        self.dicData = {}
        self.dicData['Isotope']        = None
        self.dicData['Reaction']       = None
        self.dicData['Abundance']      = None
        self.dicData['Wt']             = None
        self.dicData['GammaEnergy']    = [None, 'keV']
        self.dicData['GammaIntensity'] = None
        self.dicData['GammaCounts']    = None
        self.dicData['GammaEff']       = None
        self.dicData['Realtime']       = [None, 's']
        self.dicData['Livetime']       = [None, 's']
        self.dicData['TimeSinceIrr']   = [None, 's']
        self.dicData['TimeIrr']        = [None, 's']
        self.dicData['AverageCurrent'] = [None, 'uA']
        self.dicData['Halflife']       = [None, 's']
        self.dicData['FluxWgtedXs']    = [None, 'b']
        self.dicData['FoilMass']       = [None, 'g']
        self.dicData['DistanceToFoil'] = [None, 'cm']
        self.dicData['MeasuredFlux']   = [None, 'n/sr/uC']
```

```
        self.dicData['Lambda']         = None
        self.dicData['Activty']        = None
        self.dicData['Fluence']        = None # n/cm2
        self.dicData['DiffFluence']    = None # n/Sr/uC
        self.dicData['ReactionRate']   = None # /s
        self.dicData['N0']             = None
        self.dicData['Foil/Measured Flux Ratio'] = None

    def loadAllData(self, a_iso, a_reaction, a_abundance, a_wt, a_gammaEnergy,␣
↪a_gammaIntensity, a_gammaCounts,
                a_gammaEff, a_realtime, a_livetime, a_timeSinceIrr, a_timeIrr,␣
↪a_averageCurrent, a_halflife,
                a_fluxWgtedXs, a_foilMass, a_distanceToFoil, a_measuredFlux):
            # Energy units are [KeV]
            # distance units are [cm]
            # Activity units are [Bq]
            # Mass units are [g]
            # time units are [s]
            # Current units are [uA]

            self.Avo = 6.0221408e23

            if type(a_gammaEnergy) is list:
                a_gammaEnergy = energyUnitConverter(a_gammaEnergy)
            if type(a_realtime) is list:
                a_realtime = timeUnitConverter(a_realtime)
            if type(a_livetime) is list:
                a_livetime = timeUnitConverter(a_livetime)
            if type(a_timeSinceIrr) is list:
                a_timeSinceIrr = timeUnitConverter(a_timeSinceIrr)
            if type(a_timeIrr) is list:
                a_timeIrr = timeUnitConverter(a_timeIrr)
            if type(a_averageCurrent) is list:
                a_averageCurrent = currentUnitConverter(a_averageCurrent)
            if type(a_halflife) is list:
                a_halflife = timeUnitConverter(a_halflife)
            if type(a_fluxWgtedXs) is list:
                a_fluxWgtedXs = xsUnitConverter(a_fluxWgtedXs)
            if type(a_foilMass) is list:
                a_foilMass = massUnitConverter(a_foilMass)
            if type(a_distanceToFoil) is list:
                a_distanceToFoil = distanceUnitConverter(a_distanceToFoil)

            self.dicData['Isotope']        = a_iso
            self.dicData['Reaction']       = a_reaction
            self.dicData['Abundance']      = a_abundance
            self.dicData['Wt']             = a_wt
```

```
            self.dicData['GammaEnergy']    = [a_gammaEnergy, 'keV']
            self.dicData['GammaIntensity'] = a_gammaIntensity
            self.dicData['GammaCounts']    = a_gammaCounts
            self.dicData['GammaEff']       = a_gammaEff
            self.dicData['Realtime']       = [a_realtime, 's']
            self.dicData['Livetime']       = [a_livetime, 's']
            self.dicData['TimeSinceIrr']   = [a_timeSinceIrr, 's']
            self.dicData['TimeIrr']        = [a_timeIrr, 's']
            self.dicData['AverageCurrent'] = [a_averageCurrent, 'uA']
            self.dicData['Halflife']       = [a_halflife, 's']
            self.dicData['FluxWgtedXs']    = [a_fluxWgtedXs, 'b']
            self.dicData['FoilMass']       = [a_foilMass, 'g']
            self.dicData['DistanceToFoil'] = [a_distanceToFoil, 'cm']
            self.dicData['MeasuredFlux']   = [a_measuredFlux, 'n/sr/uC']

            self.dicData['Lambda']         = np.log(2)/self.
↪dicData['Halflife'][0]
            self.dicData['Activity']        = self.dicData['Lambda'] *␣
↪a_gammaCounts / a_gammaEff / a_gammaIntensity / (a_livetime/a_realtime) /␣
↪(1-np.exp(-self.dicData['Lambda']*a_realtime)) * np.exp(self.
↪dicData['Lambda']*a_timeSinceIrr)
            self.dicData['Fluence']        = self.dicData['Activity'] * a_wt /␣
↪(a_foilMass*a_abundance) / self.Avo / (a_fluxWgtedXs*(1e-24)) / (1- np.
↪exp(-self.dicData['Lambda']*a_timeIrr)) * a_timeIrr # n/cm2
            self.dicData['DiffFluence']    = self.
↪dicData['Fluence']*a_distanceToFoil**2.0/(a_timeIrr*a_averageCurrent) # n/Sr/
↪uC
            self.dicData['ReactionRate']   = self.dicData['Activity']/(1-np.
↪exp(-self.dicData['Lambda']*a_timeIrr)) # /s
            self.dicData['N0']             = self.Avo*a_foilMass*a_abundance/
↪a_wt
            self.dicData['Foil/Measured Flux Ratio'] = self.
↪dicData['DiffFluence']/a_measuredFlux

    def loadLimitedData(self, a_iso, a_reaction, a_abundance, a_wt,␣
↪a_gammaEnergy, a_gammaIntensity, a_gammaCounts,
                a_gammaEff, a_realtime, a_livetime, a_timeSinceIrr, a_timeIrr,␣
↪a_halflife, a_foilMass):
            # Energy units are [KeV]
            # distance units are [cm]
            # Activity units are [Bq]
            # Mass units are [g]
            # time units are [s]

            self.Avo = 6.0221408e23
```

```
            if type(a_gammaEnergy) is list:
                a_gammaEnergy = energyUnitConverter(a_gammaEnergy)
            if type(a_realtime) is list:
                a_realtime = timeUnitConverter(a_realtime)
            if type(a_livetime) is list:
                a_livetime = timeUnitConverter(a_livetime)
            if type(a_timeSinceIrr) is list:
                a_timeSinceIrr = timeUnitConverter(a_timeSinceIrr)
            if type(a_timeIrr) is list:
                a_timeIrr = timeUnitConverter(a_timeIrr)
            if type(a_halflife) is list:
                a_halflife = timeUnitConverter(a_halflife)
            if type(a_foilMass) is list:
                a_foilMass = massUnitConverter(a_foilMass)

            self.dicData['Isotope']        = a_iso
            self.dicData['Reaction']       = a_reaction
            self.dicData['Abundance']      = a_abundance
            self.dicData['Wt']             = a_wt
            self.dicData['GammaEnergy']    = [a_gammaEnergy, 'KeV']
            self.dicData['GammaIntensity'] = a_gammaIntensity
            self.dicData['GammaCounts']    = a_gammaCounts
            self.dicData['GammaEff']       = a_gammaEff
            self.dicData['Realtime']       = [a_realtime, 's']
            self.dicData['Livetime']       = [a_livetime, 's']
            self.dicData['TimeSinceIrr']   = [a_timeSinceIrr, 's']
            self.dicData['TimeIrr']        = [a_timeIrr, 's']
            self.dicData['Halflife']       = [a_halflife, 's']
            self.dicData['FoilMass']       = [a_foilMass, 'g']

            self.dicData['Lambda']         = np.log(2)/self.
↪dicData['Halflife'][0]
            self.dicData['Activity']        = self.dicData['Lambda'] *␣
↪a_gammaCounts / a_gammaEff / a_gammaIntensity / (a_livetime/a_realtime) /␣
↪(1-np.exp(-self.dicData['Lambda']*a_realtime)) * np.exp(self.
↪dicData['Lambda']*a_timeSinceIrr)
            self.dicData['ReactionRate']   = self.dicData['Activity']/(1-np.
↪exp(-self.dicData['Lambda']*a_timeIrr)) # /s
            self.dicData['N0']             = self.Avo*a_foilMass*a_abundance/
↪a_wt


    def printResults(self):
        if self.dicData['Activity'] is not None:
            print('Activity = {}'.format(self.dicData['Activity']))
        if self.dicData['Fluence'] is not None:
            print('Fluence [n/cm2] = {}'.format(self.dicData['Fluence']))
```

```
        if self.dicData['DiffFluence'] is not None:
            print('DiffFluence [n/Sr/uC] = {}'.format(self.
↪dicData['DiffFluence']))
        if self.dicData['ReactionRate'] is not None:
            print('ReactionRate [/s] = {}'.format(self.dicData['ReactionRate']))
        if self.dicData['N0'] is not None:
            print('N0 = {}'.format(self.dicData['N0']))
        if self.dicData['Foil/Measured Flux Ratio'] is not None:
            print('Foil/Measured Flux Ratio = {}'.format(self.dicData['Foil/
↪Measured Flux Ratio']))

    def printAllKeys(self):
        print('All Dictionary Data Keys')
        for x in self.dicData.keys():
            print('Key: {} ; Data: {} '.format(x,self.dicData[x]))

    def printKeysWithData(self):
        print('Only Dictionary Data Keys with Data')
        for x in self.dicData.keys():
            if self.dicData[x] is not None:
                print('Key: {} ; Data: {} '.format(x,self.dicData[x]))
```

[ ]:
```
def␣
↪createFluxMcnpRatioPerBin(MCNP_Array1,MCNP_Array2,tally_1,tally_2,flux_total):
↪
    #This Function takes two arrays of MCNP_tools() objects, constructs a new␣
↪flux given
    # flux_total shape and the MCNP results, and takes the ratio of the two␣
↪resulting McnpFlux
    #Assumes the MCNP_Array# is an array where each element contains a␣
↪MCNP_tools() object
    # loaded with MCNP tally simulation results. Each element coorespounds to␣
↪the MCNP simulation
    # of the individual bin in the flux_total.
    #Flux_total must be in total units (not per MeV).
    #Tally_# is a string of the loaded tally to use in the MCNP_Tools() object.

    # Check Array Lengths
    if (len(MCNP_Array1) != len(flux_total)) | (len(MCNP_Array2) !=␣
↪len(flux_total)):
        print('ERROR: Flux is not equal to MCNP_Array')
        print(len(MCNP_Array1))
        print(len(MCNP_Array2))
        print(len(flux_total))
```

```
    #normalize input flux
    flux_total = flux_total/np.sum(flux_total)
    #create empty arrays to fill
    McnpFlux_num = np.zeros(len(flux_total))
    McnpFlux_dom = np.zeros(len(flux_total))

    #fill empty arrays
    for flux_binc,MCNP_binData in zip(flux_total,MCNP_Array1):
        # Check Tally lengths
        if (len(MCNP_binData.getTallyResults(tally_1)) != len(flux_total)):
            print('ERROR: Flux is not equal to MCNP_Tally_array')
            print(len(flux_total))
            print(len(MCNP_binData.getTallyResults(tally_1)))

        McnpFlux_num += MCNP_binData.getTallyResults(tally_1)*flux_binc

    for flux_binc,MCNP_binData in zip(flux_total,MCNP_Array2):
        #Check Tally Length
        if (len(MCNP_binData.getTallyResults(tally_2)) != len(flux_total)):
            print('ERROR: Flux is not equal to MCNP_Tally_array')
            print(len(flux_total))
            print(len(MCNP_binData.getTallyResults(tally_2)))

        McnpFlux_dom += MCNP_binData.getTallyResults(tally_2)*flux_binc

    #Take ratio
    Out = McnpFlux_num/McnpFlux_dom
    Out[np.isnan(Out)] = 0
    Out[np.isinf(Out)] = 0

    return Out

def createFluxMcnpRatioSum(MCNP_Array1,MCNP_Array2,tally_1,tally_2,flux_total):
    #This Function Takes two arrays of MCNP_tools() objects, constructs a new␣
 ↪flux given
    # flux_total shape and the MCNP results, and takes the ratio of the SUM of␣
 ↪the two
    # resulting McnpFluxes
    #Assumes the MCNP_Array# is an array where each element contains a␣
 ↪MCNP_tools() object
    # loaded with MCNP tally simulation results. Each element coorespounds to␣
 ↪the MCNP simulation
    # of the individual bin in the flux_total.
    #Flux_total must be in total units (not per MeV).
    #Tally_# is a string of the loaded tally to use in the MCNP_Tools() object.

    # Check Array Lengths
```

```
    if (len(MCNP_Array1) != len(flux_total)) | (len(MCNP_Array2) !=␣
↪len(flux_total)):
        print('ERROR: Flux is not equal to MCNP_Array')
        print(len(MCNP_Array1))
        print(len(MCNP_Array2))
        print(len(flux_total))
    #normalize input flux
    flux_total = flux_total/np.sum(flux_total)
    #create empty arrays to fill
    McnpFlux_num = np.zeros(len(flux_total))
    McnpFlux_dom = np.zeros(len(flux_total))
    #fill empty arrays
    for flux_binc,MCNP_binData in zip(flux_total,MCNP_Array1):
        # Check Tally lengths
        if (len(MCNP_binData.getTallyResults(tally_1)) != len(flux_total)):
            print('ERROR: Flux is not equal to MCNP_Tally_array')
            print(len(flux_total))
            print(len(MCNP_binData.getTallyResults(tally_1)))

        McnpFlux_num += MCNP_binData.getTallyResults(tally_1)*flux_binc

    for flux_binc,MCNP_binData in zip(flux_total,MCNP_Array2):
        #Check Tally Length
        if (len(MCNP_binData.getTallyResults(tally_2)) != len(flux_total)):
            print('ERROR: Flux is not equal to MCNP_Tally_array')
            print(len(flux_total))
            print(len(MCNP_binData.getTallyResults(tally_2)))

        McnpFlux_dom += MCNP_binData.getTallyResults(tally_2)*flux_binc

    #Take ratio
    Out = np.sum(McnpFlux_num)/np.sum(McnpFlux_dom)

    return Out
```

[ ]:
```
# Below is the main class of the Unfolding code.
# This class finds the neutron energy spectra via the Max Entropy Unfolding␣
↪Method
class MaxEntropy(object):

    # a_DOF = Degrees of Freedom = # of Reactions; a_counts = reaction rate
    # assumes rows are Bins; columns are reactions for 2D numpy arrays
    def __init__(self, a_counts, a_Sigma, a_DOF, a_CrossSectionMatrix,␣
↪a_FluxGuess, lambdaGuess = None):
        self.counts = a_counts
        self.sig    = a_Sigma
        self.DOF    = a_DOF
```

```
        if a_CrossSectionMatrix.shape[1] != a_DOF:
            print('ERROR: a_CrossSectionMatrix ColumnN does not equal a_DOF' )
            self.XSMat = None
        else:
            self.XSMat  = a_CrossSectionMatrix
        self.GFlux  = a_FluxGuess
        if lambdaGuess is None:
            self.lambdaGuess = np.ones(len(self.counts))

        else:
            self.lambdaGuess = lambdaGuess

        return 0

    def OptimizeMEnt(self):
        def MaxEnt_func(params):
            lamb = params.reshape(1,len(params))

            metric = -(-np.sum(self.GFlux*np.exp(-np.sum(lamb*self.
↪XSMat,axis=1))) \
                       - np.sqrt(self.DOF*np.sum(lamb**2*self.sig**2)) \
                       - np.sum(self.counts*lamb))
            return metric

        MaxFunEvals       = 100000
        Maxiter           = 100000
        my_constraints = ({'type': 'eq', 'fun': self.constraint2 },)
        return scipy.optimize.minimize(MaxEnt_func, self.lambdaGuess,␣
↪method='Nelder-Mead', options={'maxiter':Maxiter, 'maxfev':MaxFunEvals}).x
```